

Doctoral Dissertation

博士論文

A study on *in-situ* observation of oxidation reaction at a low
temperature by Field Ion Microscopy and Atom Probe
(低温における酸化反応の電界イオン顕微鏡とアトムプローブ
によるその場観察に関する研究)

A Dissertation Submitted for the Degree of Doctor of Philosophy July
2020

令和二年 7 月博士(工学)申請

Department of Applied Chemistry, Graduate School of Engineering,
The University of Tokyo
東京大学大学院工学系研究科
応用化学専攻

Sunwei Chen

陳 孫維

CONTENTS

ABBREVIATIONS	i
CHAPTER 1 INTRODUCTION	1
1.1 Atom Probe Microscopy.....	2
1.1.1 Field Emission Microscope	3
1.1.2 Field Ion Microscope.....	4
1.1.3 Atom Probe Field Ion Microscope	8
1.1.4 Atom Probe Tomography	9
1.2 Study of Surface Reaction by APM	12
1.2.1 Field-Induced Ion Emission on Surface Reaction	12
1.2.2 Previous Studies of Reaction by APM	13
1.3 The Objective of This Research	19
1.4 Reference	22
CHAPTER 2 EXPERIMENTAL METHOD.....	27
2.1 Specimen Preparation Methods	27
2.1.1 Electropolishing Method	27
2.1.2 Focused Ion Beam Based Method	29
2.2 Specimen Preparation in This Research	32
2.2.1 The Preparation Method of Tungsten	32
2.2.2 The Preparation Methods of Platinum and Platinum/Palladium Alloy ..	33
2.3 Atom Probe Instrument	35
2.3.1 Sample Stage	39
2.3.2 Cryostat.....	41
2.3.3 Position Sensitive Detector.....	41
2.2.4. Laser Pulse System.....	43
2.2.5 Voltage System.....	44
2.2.6 Gas Introduction System	45
2.2.7 Mass Spectrometer	47
2.4 Reference	49
CHAPTER 3 ELECTRIC FIELD DISTRIBUTION	51
3.1 Simulation.....	53
3.2 Experimental Method	54
3.2.1 Determination of the Sample Apex on a Sample Surface	54
3.2.2 Ion Intensity Contour Maps on a Sample Surface	56
3.2.3. EF Distribution Calculation.....	58
3.3 Specimen Shape Effect.....	59

3.4 Conclusion.....	61
3.5 Reference.....	62
CHAPTER 4 QUANTITATIVE ANALYSIS OF RESIDUAL HYDROGEN	63
4.1 Residual Hydrogen in AP analysis	64
4.2 Source of Residual Hydrogen.....	68
4.3 Specimen Shape Effect.....	70
4.4 Field Adsorption.....	72
4.5 Field Desorption	73
4.6 Conclusion.....	75
4.7 Reference.....	76
CHAPTER 5 HYDROGEN OXIDATION REACTION ON Pt.....	78
5.1 FIM Image.....	79
5.2 Temperature Effect.....	80
5.3 Active Site	83
5.4 Laser Pulse.....	86
5.5 Electric Field	88
5.5.1 The Static Voltage	88
5.5.2 The Value of Static Voltage	89
5.6 Surface Corrosion.....	90
5.7 Conclusion.....	92
5.8 Reference.....	93
CHAPTER 6 HYDROGEN OXIDATION REACTION ON W AND Pt/Pd ALLOY ...	94
6.1 Reaction on Tungsten.....	94
6.1.1 FIM Image.....	94
6.1.2 Temperature Effect.....	95
6.1.3 2D Mapping.....	97
6.2 Reaction on Platinum/Palladium Alloy	99
6.2.1 Temperature Effect.....	99
6.2.2 2D Mapping.....	101
6.3 Conclusion.....	102
6.4 Reference.....	103
CHAPTER 7 CARBON MONOXIDE OXIDATION REACTION ON Pt SURFACE	104
7.1 CO Adsorption on Pt Surface	105
7.2 Pressure Ratio of O ₂ to CO.....	107
7.3 Conclusion.....	108
7.4 Reference.....	108

CHAPTER 8 CONCLUSION AND PERSPECTIVE.....	109
APPENDICES	114
PUBLICATIONS.....	135
ACKNOWLEDGEMENT	136

ABBREVIATIONS

1D	One-Dimensional
1DAP	One-Dimensional Atom Probe
2D	Two-Dimensional
3D	Three-Dimensional
3DAP	Three-Dimensional Atom Probe
AC	Alternating Current
AES	Auger Electron Spectroscopy
AFM	Atomic Force Microscope
AP	Atom Probe
APFIM	Atom-Probe Field Ion Microscope
APT	Atom Probe Tomography
BIF	Best Imaging Field
CAP	Catalytic Atom Probe
DLD	Delay Line Detector
DC	Direct Current
e	Electron Charge
E_c	Potential Energy of Conduct Level
E_o	Potential Energy of Local Vacuum Level
EF	Electric Field
XPS	X-ray Photoelectron Spectroscopy
FEM	Field Emission Microscope
FIM	Field Ion Microscope
FIMS	Field Ion Mass Spectrometer

HREELS	High-Resolution Electron Energy Loss Spectroscopy
I_o	Energy of the First Ionization
IR	Infrared
ISS	Ion Scattering Spectroscopy
LH	Langmuir-Hinshelwood
MB	Molecular Beams
MCP	Microchannel Plate
m/n	Mass to Charge Ratio
PE	Potential Energy
PSD	Position Sensitive Detector
SEM	Scanning Electron Microscope
SIMS	Secondary Ion Mass Spectroscopy
TEM	Transmission Electron Microscope
ToFMS	Time-of-Flight Mass Spectrometer
TPR	Temperature-Programmed Reaction
U_e	Electron Potential Energy
UHV	Ultra-High Vacuum
XAFS	X-ray Adsorption Fine Structure
X_c	Critical Distance
XPS	X-ray Photoelectron Spectroscopy
ϕ	Work Function
ϵ_o	Permittivity of Vacuum

CHAPTER 1 INTRODUCTION

The urgency to understand chemical/physical properties of surface and reaction processes on surface at a fundamental level has drastically promotes the development of surface analysis technique. Several surface analysis techniques have been developed since 1960s. The discovery of the electron, ion, and photon and their interactions between surfaces serve to inspire the prosperity of surface analysis technique [1].

Microscopy is a crucial surface analysis technique, offering unique insights into the microstructures and chemical components of materials across different length scales, ranging from atomic, nano-scale, mesoscale to macroscale [2]. A general context of widely used microscopy is exhibited in figure 1.1 in terms of chemical sensitivity and typical sizes. Obviously, no technology can characterize materials with full scale of spatial and chemical dimensions. Transmission electron microscopy (TEM) or scanning tunneling electron microscopy (STEM), time-of-flight secondary ion mass spectrometer (ToF-SIMS), and atom probe microscopy (APM) can detect particle(s)/atom(s) bellow 1 nm, in which the sensitivity of (S)TEM and APM is higher than that of ToF-SIMS. Besides, APM is able to provide 2-dimensional (2D) and 3-dimensional (3D) analytical mapping of chemical and structural information of the material in atomic-scale resolution, while 2D mapping is solely obtained by (S)TEM. APM is therefore recognized as a burgeoning and mainstream microscopy technique, evidenced by an increasing application in laboratories and industries [3].

Due to APM's unique and compelling insights, this technique is widely employed in the field of chemistry analysis, material science and nanotechnology because the central theme of these areas is to find out the relationship between chemical/physical properties and performance of material. The development history and underlying principle behind APM is introduced in **section 1.1**.

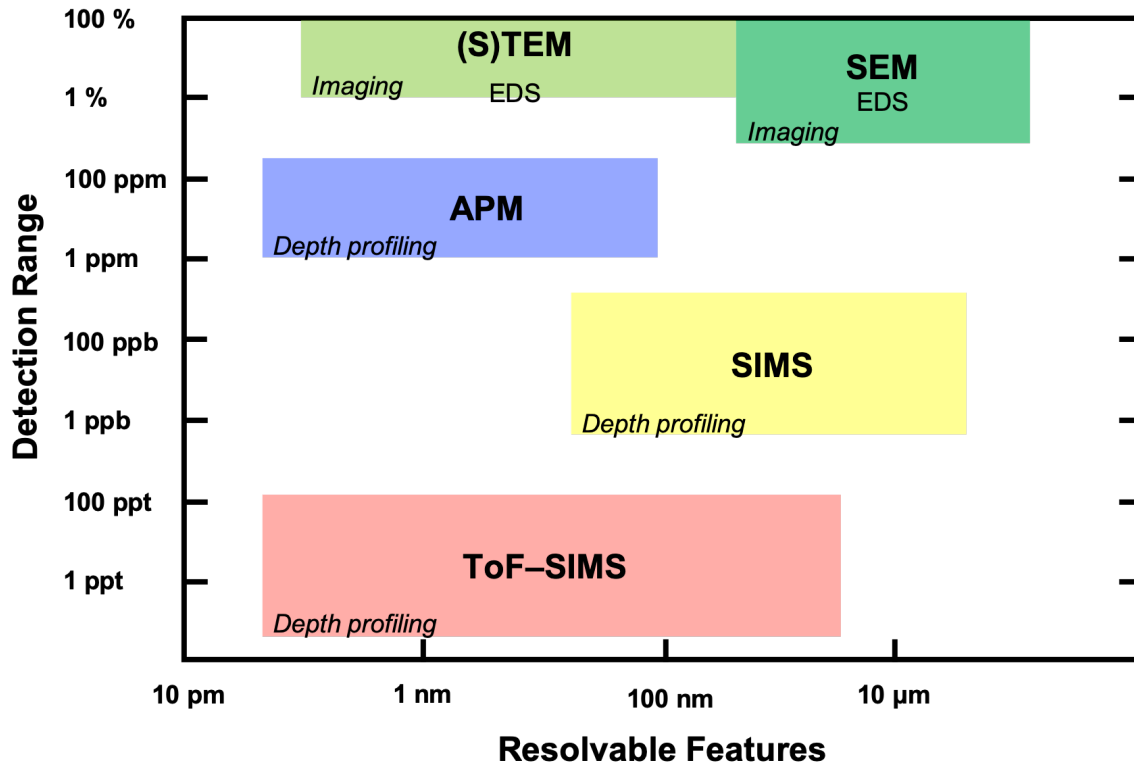


Figure 1.1 A general context of detection range (chemical sensitivity) and spatial resolution of typical microscopy and microanalysis techniques. (S)TEM is (scanning) transmission electron microscopy. EDS is energy dispersive X-ray spectroscopy. SEM is scanning electron microscopy. SIMS is secondary ion mass spectrometer. ToF is time-of-flight.

1.1 Atom Probe Microscopy

Atom probe microscopy (APM) is a field emission technology, which encompasses various imaging and analysis techniques, including field electron emission, field ionization, and field evaporation. APM mainly consists of the Field Ion Microscopy (FIM), non-tomographic Atom Probe (AP), and Atom Probe Tomography (APT). The modern state-of-the-art instrument of field evaporation techniques is APT [4].

The progress of APT techniques has witnessed the improvement of mechanical technique and theory innovation. To understand its development history, one needs to be aware of the different types of field emission techniques and the underlying theory. Here, a brief introduction is made in a chronological order.

APT has been evolved by the mean of field emission microscopy (FEM), FIM, field desorption mass spectrometer (FDMS), field ion mass spectrometer (FIMS) and atom-probe field ion microscopy (APFIM). All these acronyms refer to specific instruments and techniques in the development process of APT. Generally, FEM and FIM, which are the earliest field emission techniques, serve to determine the surface structure. APFIM is a FIM facilitated a small entrance aperture into the field-free flight tube called time-of-flight mass spectrometer (ToFMS), which enables the detection of the single ions. APFIM sometimes refers to a one-

dimensional atom probe (1D-AP) or a probe-hole AP, as only the ions from specific area can be detected. Later, a three-dimensional atom probe (3D-AP) was developed with a wide-angle position and time detector permitting the analysis of mass-to-charge ratio (m/n) of ions from a large part of the specimen surface [4].

1.1.1 Field Emission Microscope

The development of field evaporation techniques traces its point of origin to 1744 when the phenomenon of the electric-field-induced emission of electrons from a pointed wire in a poor vacuum, called electrical discharge phenomenon, was observed by Winkler [5]. This is recognized as the field electron emission-initiated, earlier than the discovery of electron by J. J. Thomson in 1897 [6]. The basic theory and effects of field electron emission, which have a significant influence on electron emission current, have been systemically studied by Lauritsen, Fowler, and Nordheim *et al.* [7–9]. FEM was invented by E. W. Müller in 1937, Berlin [10]. A typical FEM is exhibited in Figure 1.2. The emitter sample is a sharp metal needle with an apex radius less than 1 μm . A negative voltage (-3 kV to -5 kV) is applied to the emitter to create a negative electric field on the emitter surface with a magnitude of $2\text{--}5\text{ V nm}^{-1}$. Consequently, electron tunneling was triggered by the high electric field. FEM image realized by electron detector, records the current density distribution on the emitter surface. The current density would be varied according to the local electric field and work function. FEM is arguably regarded as the first surface science techniques with the ability to study the atomic-level nanoscience [11].

However, in the old generation of FEM, the experiment was conducted at room temperature and a typical magnification obtained was approximately 10^5 , not high enough to resolve individual atom.

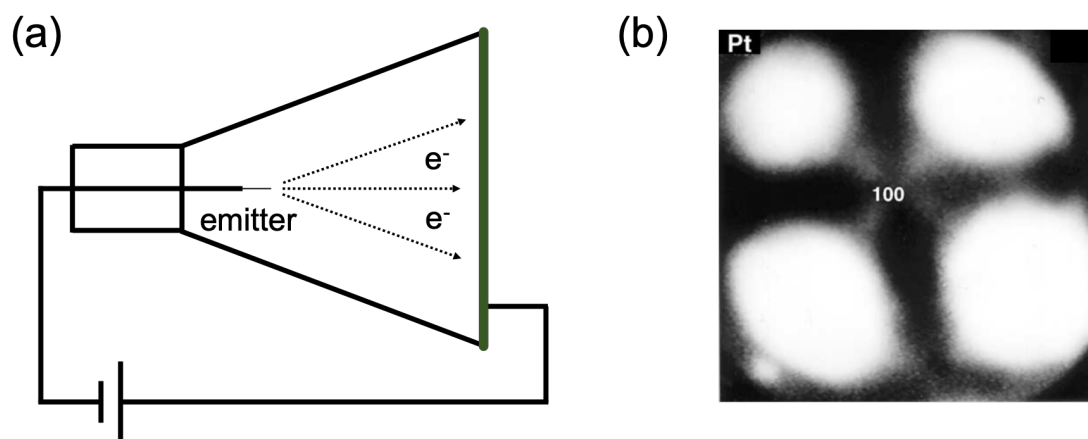


Figure 1.2 (a) An typical field emission microscope in which the emitter faces to a phosphor screen in vacuum. Electrons are emitted and projected to form an FEM image on the screen, when a negative bias voltage is applied to the sample. (b) FEM image of a (001)-oriented Pt tip.

1.1.2 Field Ion Microscope

FIM was a radical evolution of FEM, which was first made to work at the Pennsylvania State University by E. W. Müller and Bahabur in 1955 [12,13]. It achieved a major historical milestone in field emission techniques, in that human being saw the single tungsten atom for the first time.

Four distinct changes were required to obtain a successful FIM image: the polarity of the tip bias changed from negative to positive, the specimen cooled down to cryogenic temperature, a sharper needle-shaped less than 100 nm, and finally, an imaging gas introduced into main chamber to get a FIM image.

A typical FIM is shown in Figure 1.3. The specimen is mounted on a supporting electrode and faces to a detector. The typical operation of the FIM is as follows. Cool the specimen to a suitable cryogenic temperature (usually 20 K–60 K) and introduce a proper image gas into the main chamber. The pressure of imaging gas should be kept around 10^{-5} Pa. After applying a high voltage on the specimen, the imaging gas will be ionized and the ions are ejected to the screen to identify the surface structure at atomic scale.

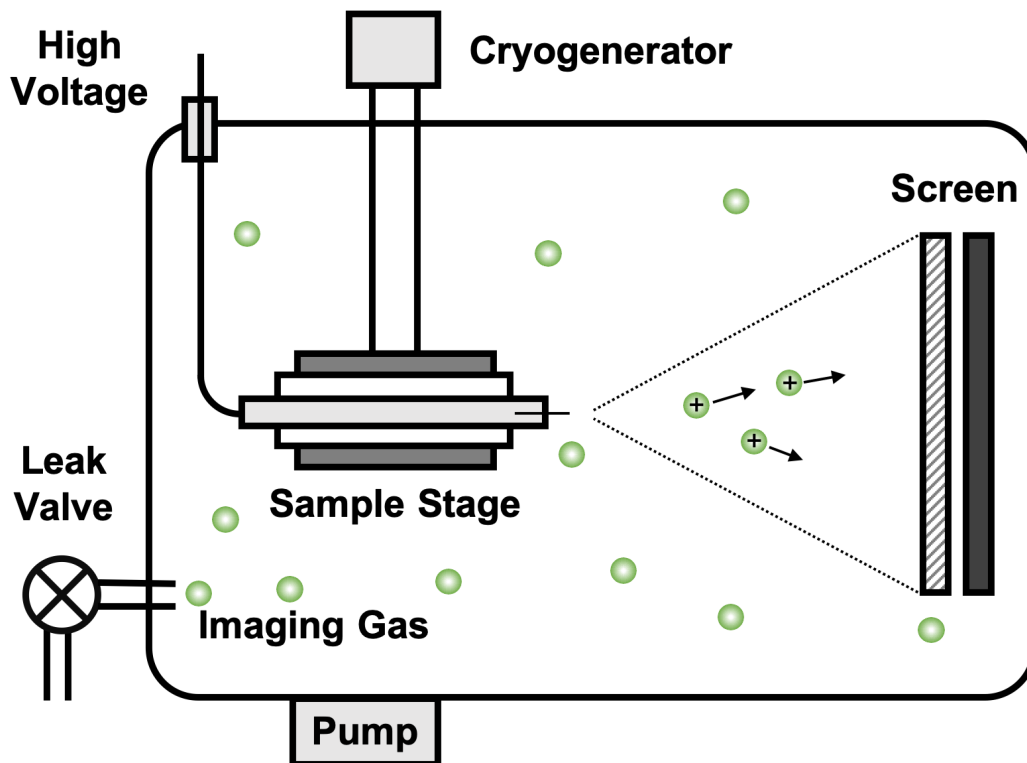


Figure 1.3 Schematic diagram of a typical field ion microscope.

The imaging gas can be captured by high electric field around the specimen. These gases move from shank to apex via a thermal accommodation process. During this process, the gas molecule loses its kinetic energy gradually and gets attracted to the specimen surface.

The field ionization of imaging gas refers to a field-induced removal of an electron from an atom. This phenomenon involves the potential energy (PE) of an electron of the imaging

gas, called electron potential energy, denoted by U_e . In the Sommerfeld model, the work needed to take an electron from the Fermi level, and put the electron at the position somewhere outside the emitter surface, is called the local thermodynamic work function, denoted by ϕ . The electron PE at this position refers to the local vacuum level, denoted by E_o . E_c represents the electron potential energy corresponding to the base of the metal conduction band. The emitter Fermi level is treated as the level of the laboratory Earth. In the presence of an electric field, the PE of an electron from the outer shell of the gas atom is deformed by electric field. As shown in Figure 1. 4, on a specimen surface subjected to a high electric field, when an external atom is present, with the nucleus of the external atom at position X_c , simple model assumes that an electron could see electron potential energy and a repulsive component due to the image of the charge. The electron potential becomes

$$U_e \approx \phi + eFx - \frac{e^2}{16\pi\epsilon_o x} + \frac{ze^2}{4\pi\epsilon_o(X_c+X)} - \frac{ze^2}{4\pi\epsilon_o|(X_c-X)|} \quad (1.1)$$

Where, e represents the electron charge, ϵ_o represents the permittivity of vacuum, X represents the electrical distance. The parameter z allows the nucleus to be allocated an ‘effective charge’ ze . The electron tunneling takes place as the nucleus is located on the critical surface, where the electron level of the topmost atomic orbital is equal to the emitter Fermi level. The electron tunneling only happens when the PE of the electron from the gas atom should coincide with, or be higher than the conduction level in the metal, that is close to the Fermi level. For the first approximation, the critical distance can be written as:

$$X_c = \frac{I_o - \phi}{eF} \quad (1.2)$$

where I_o is the energy of the first ionization. This process can only take place when the gas atom is beyond this critical distance away from the surface, as shown in Figure 1.5. These gas molecules get field ionized just outside a critical surface. The area between the critical surface and emitter surface is called forbidden zone, where the electron tunneling cannot happen. Therefore, the molecules cannot be ionized in this forbidden zone.

The probability of ionization depends on the potential barrier to the electron tunneling process, and the width of the barrier is proportional to the electric field. Therefore, the ionization probability is intrinsically proportional to the electric field. In the case of an atomic curve surface of FIM sample, the relative electric field is more intense over protruding atoms corresponding to the edges of the atomic terrace (Figure 1. 6b). If the emitter surface is well ordered, a good FIM image can be obtained. The FIM image is a set of bright image spot, which presents the protruding surface atoms on the emitter surface (Figure 1. 6c) [15].

The choice of imaging gas is determined by the specimen material and desired microscope operating temperature. The most commonly used imaging gases are listed in Table 1.. The boiling point and best image field are given in Table 1.. In principle, only the gas that does not condense on the specimen at the cryogenic temperature and does not chemically react with the sample, could be used. Besides, best imaging field (BIF) of imaging gas should be below evaporation field [16,17].

Table 1.1 Boiling Points (at standard atmospheric pressure) and best imaging field (BIF) of commonly used imaging gases.

Image gas	Boiling point (K)	BIF (V nm^{-1})
Hydrogen	20	23
Helium	4	45
Neon	27	37
Nitrogen	77	17
Argon	87	23

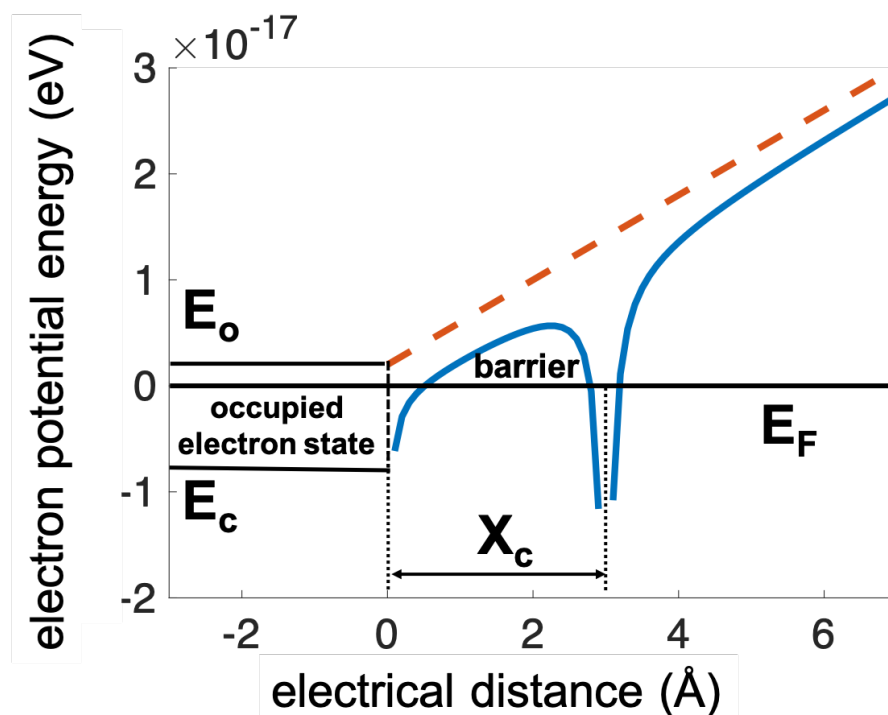


Figure 1. 4 The blue curve exhibits the variation of the electron potential energy against the distance between surface and the nucleus of external atom, under a high electric field presented by orange dash line, presenting the tunnelling barrier experienced by an electron tunnelling from the topmost filled orbital level of an external atom to the emitter Fermi level. E_o is the local vacuum level. E_F is the Fermi level. E_c is the the electron potential energy corresponding to the base of the metal conduction band. The energy reference is taken at the level of the topmost filled atomic orbital.

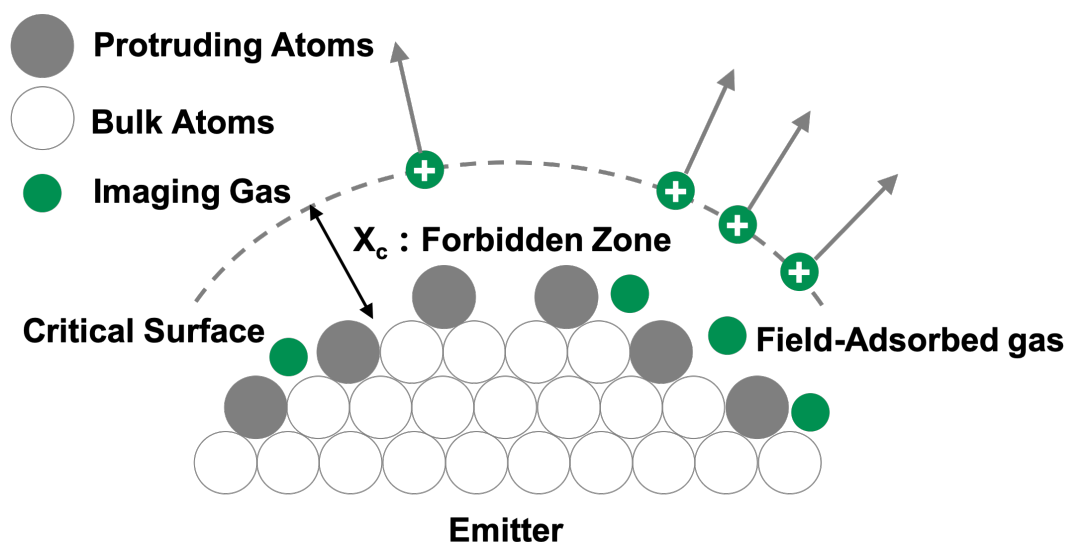


Figure 1.5 Field ion imaging process. The imaging gas becomes thermally accommodated to the cryogenic surface after a series of collisions. The imaging gas molecular get polarized when approaching the positively biased specimen surface. By a sufficient electric field, the field-adsorbed gas is ionized at the critical surface, where the electron tunnelling happens. The forbidden zone is the area between critical surface and emitter surface, where the gas molecules cannot be ionized. The ions repel from the specimen towards the detection screen.

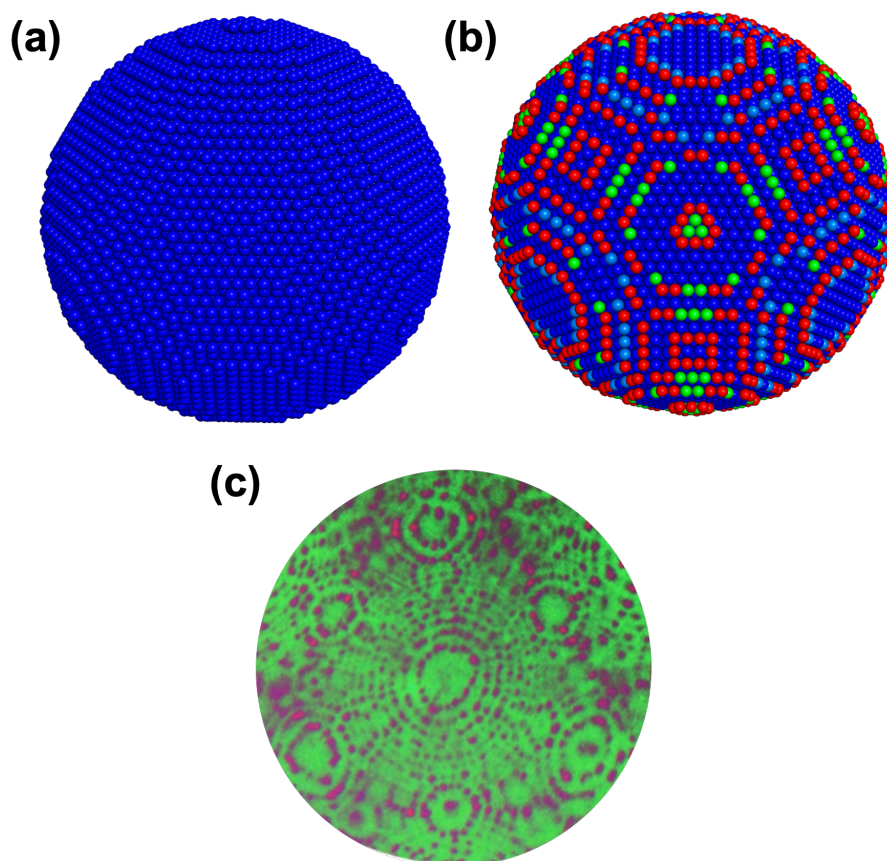


Figure 1. 6 (a) A ball model of (111)-oriented Pt hemisphere with a radius of 10 nm, (b) The protruding atoms on Pt surface, red, green and blue atoms shown in descending order by relative electric field, (c) a typical FIM image, the purple spots representing the protruding atoms.

1.1.3 Atom Probe Field Ion Microscope

To identify the atoms imaged on FIM detectors, Müller *et al.* in 1968 developed an APFIM [18,19]. The FIM was combined with a mass spectrometer, by which the ions passing through the small hole in the center of the microchannel plate (MCP) and phosphor screen can be detected, as shown in Figure 1.7. The specimen is mounted on a goniometer so that all points or atoms on the surface of the specimen can be selected for analysis. However, the ions in a limited area could be detected at one time. When it comes to the mass spectrometer, rather a magnetic sector mass spectrometer, the ToFMS was universally adopted for the atom probe, for the reason that apart from its simple design, the ToFMS is equally sensitive to all elements. In the ToFMS, a high positive voltage is applied to the specimen, ions can field evaporate from the surface by the application of either a negative voltage pulse to a counter electrode or a positive voltage pulse to the specimen. The ratio of the amplitude of pulse voltage to standing voltage values is called pulse fraction, which is typically 15%–20% in practice. The evaporation rate depends on the standing voltage, the amplitude of the pulse, and the specimen temperature. Typically, one or fewer atoms are evaporated per pulse to make sure that the analyzer can correctly analyse each ion.

In mass-to-charge analysis process, the potential energy of an ion obtained on the specimen surface, neV , is converted to kinetic energy $1/2 mv^2$, when leaving the surface. Here the n is the charge number of the ion, the e is the electron charge, V is the total voltage applied on the specimen, m is the mass of the ion, v is the average flying speed of the ion from specimen surface to a mass spectrometer, which can be calculated by $v = d/t$, where the d and t represent the flying distance and flying time, respectively. Then the mass-to-charge ratio of the ion is given by

$$\frac{m}{n} = \frac{2e}{d^2} (V_{static} + V_{pulse}) t^2 \quad (1.3)$$

V_{static} is the standing voltage on the tip, and V_{pulse} is the pulse voltage amplitude [20].

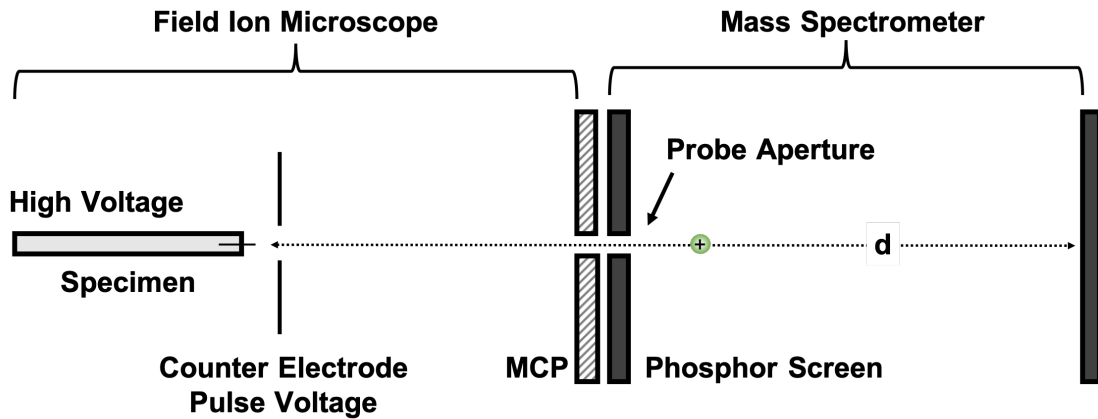


Figure 1.7 Schematic diagrams of a typical APFIM.

1.1.4 Atom Probe Tomography

Later, a *three-dimensional atom probe* (3DAP) was developed with a wide-angle position and time detector, which permitted the analysis of the mass-to-charge of ions from a large part of the specimen surface. Nevertheless, the generic name of 3DAP may cause misunderstanding, as all atom-probe variants generate the data with three-dimensional traits. In consequence, a new generic name ‘APT’ was proposed. The word ‘tomography’ was derived from the ‘*tomos*’ (part) and ‘*graphein*’ (to write) in Greek, which was introduced to describe the analysis innovation from two-dimensional X-radiographs to three-dimensional information. At present, this word is generally applied to any methods providing three-dimensional images of the internal structure in a solid sample.

A schematic diagram of a typical APT is exhibited in Figure 1.8. The system consists of a conventional APFIM and FIM. A laser pulse (or a voltage pulse) is employed to trigger the surface atoms. A local electrode is placed in front of the specimen to increase the local electric field on the specimen surface. The time and position sensitive detector (PSD), as presented in Figure 1.9a, is composed of MCP and delay line detector (DLD). The MCP is employed to amplify the ions signal. The DLD can be used to record the position of the detected particles, which is encoded by the current arrival time difference at both ends of each parallel-pair delay-line, for (X_1 , X_2) and (Y_1 , Y_2) in each layer independently (Figure 1.9b). The operation principle of MCP and DLD will be explained in chapter 2 in detail. The sequence of atom hitting on the detector is employed to track the serial evaporation of atoms in the serial evaporation of the layers. Then a three-dimensional image can be reconstructed from this combination of two-dimensional positions and evaporation sequences. In APT, the sample should be kept at the temperature from 20 K to 60 K to improve the spatial resolution via decreasing the thermal vibration energy of the atoms. An ultra-high vacuum is required to eliminate surface contamination [21–24].

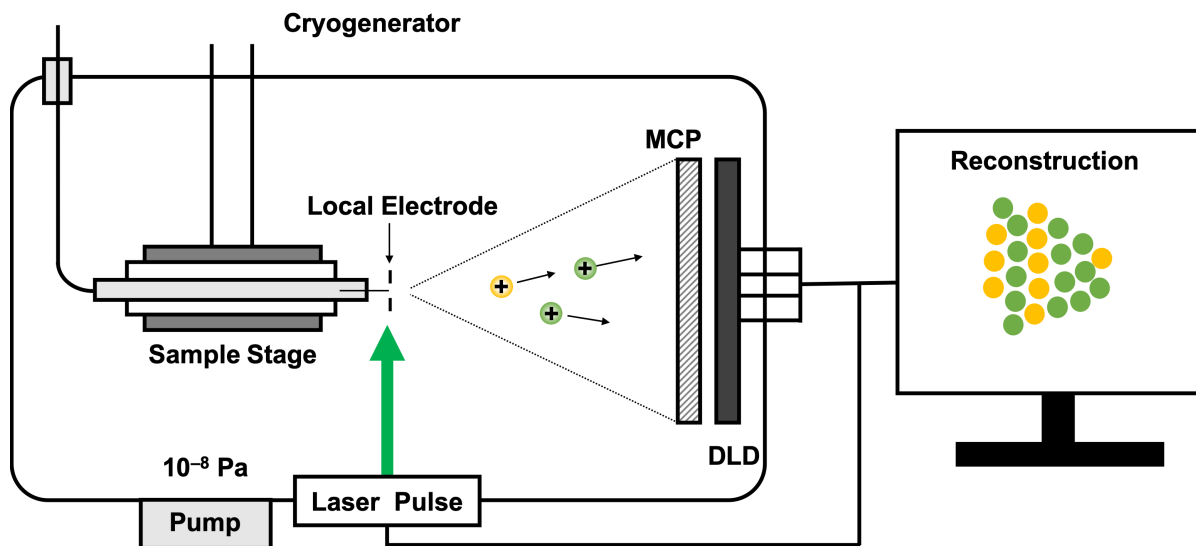


Figure 1.8 Schematic diagram of a typical atom probe tomography.

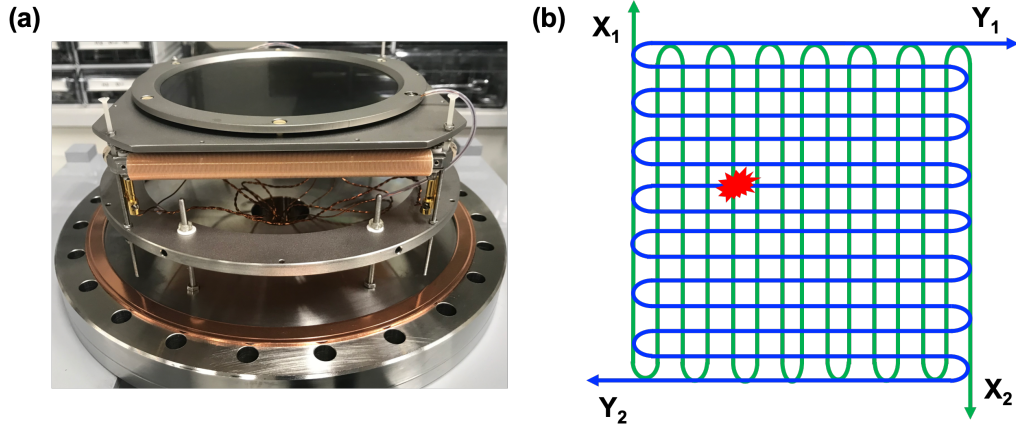


Figure 1.9 (a) A general view of the MCP and DLD, (b) Operation principle of DLD: as an electron beam hits DLD, the arriving time difference at both ends (X_1, X_2) and (Y_1, Y_2) of each parallel-pair delay-line can be employed to determine the hitting position.

The field evaporation is the field-induced removal of an atom from its own lattice, which refers to a combination of ionization and desorption of an atom from AP specimen surface, which is subjected to a very intense electric field. As shown in Figure 1.10, with sufficient electric field, the polarized surface atom can be pulled away from the surface while one of its electrons was draining into the specimen bulk. The ionized atom repels from the surface towards the PSD. Despite the underlying mechanism of field desorption process is still under debate and neither model has been experimentally proven beyond doubt. A widely accepted explanation is that the field evaporation is due to the escape of an ion over a barrier reduced by virtue of reduced thermal activation by the intense electric field [2]. A typical evaporation field for pure metal is listed in appendix A.

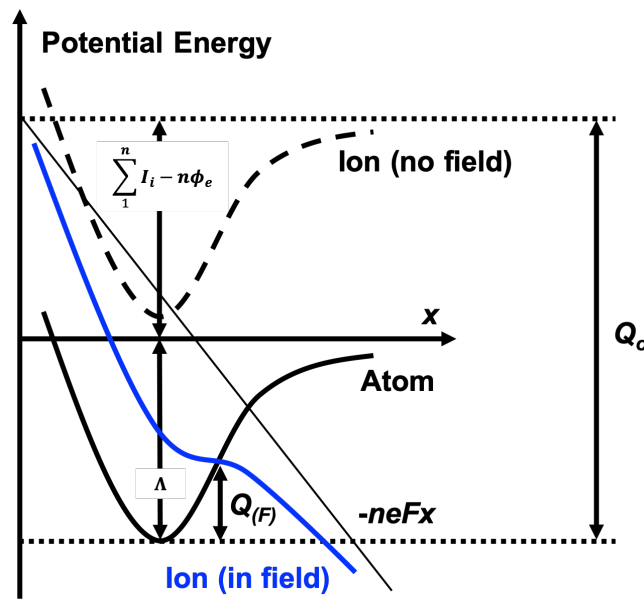


Figure 1.10 Potential energy of an atom (black line) and an ion (black dash line) in absence of electric field and the potential energy of an ion (blue line) modified by electric field. V is potential, Λ is

sublimation energy, n is the charge degree, I_i is the i th ionization energy, ϕ_e is the work function of emitting surface, Q_o and $Q_{(F)}$ are the energy barrier without and with electric field.

A typical APT image is shown in Figure 1.11, all the atoms in a certain volume of a titanium carbide(TiC) steel were analyzed [25]. The selected atoms, titanium, carbon and deuterium, are shown in the 3D maps. The position of every atom can be clearly located in the maps.

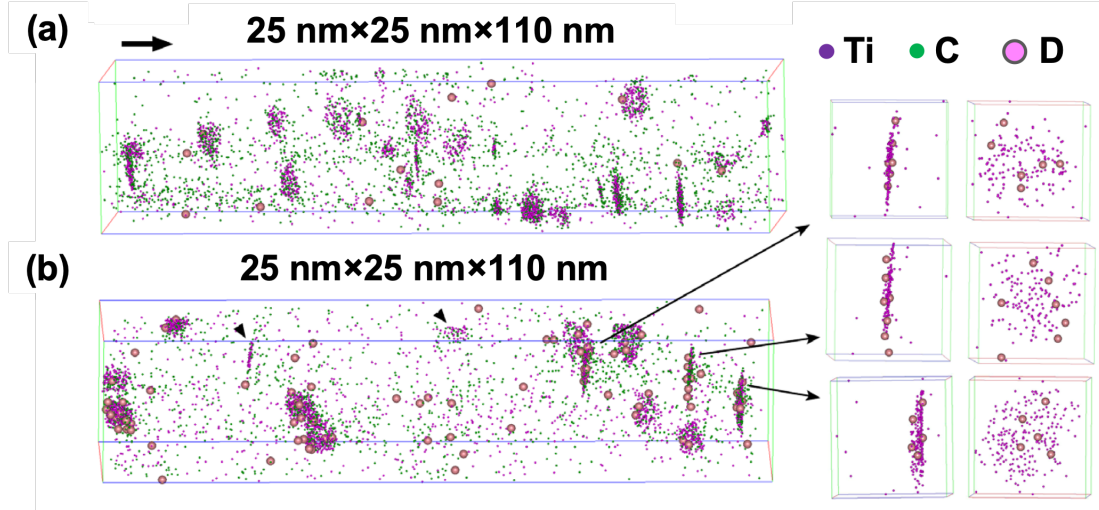


Figure 1.11 3D maps of deuterium-uncharged (a) and deuterium-charged specimens (b) of a TiC steel with annealing. The arrow on the upper left corner indicates the analysis direction.

The application of the laser pulse dramatically improves the mass resolution and material application. The use of a voltage pulse with a duration in nanosecond range leads to an energy spread of the ions. In contrast, the ultrashort laser pulse (100 fs to 10 ps) can eliminate the significant ion energy spread, resulting in a high mass resolution. In addition, the laser pulse enables the analysis of high resistance material, such as semiconductors and insulators. In voltage pulse mode, only metal can be analyzed, because the poorly conductive material cannot transmit the voltage pulse to the sample apex efficiently.

The APT development has witnessed so many generations of machine-building over nearly 60 years, as attempts were made to achieve as many as emitter materials as possible, as precise as reconstruction method, as convenient as operation protocol. It is also a story about the supporting improvement in electronic equipment, software, computer, and scientific theory. Over 60 years of development, the operation APT data collection has become more convenient, making it on the list of common characterization methods not only in laboratories but also in factories.

The Last decade has seen the automation of APT techniques, including automatic data collection, analysis, calibration, and sample preparation, and all these benefited from computer science. Consequently, the application of APT is widespread both in academic and industrial laboratories.

Despite the prosperity of the application of APM in material analysis, studies of the reaction process by APT have seldomly been reported. In this research, the emphasis is put on the study of the *in-situ* observation of reaction by APM.

1.2 Study of Surface Reaction by APM

The chemical composition of an on-going reaction on the sample surface is more complicated than that in static sample of APT and FIM analysis. As mentioned above, in APT analysis, the detected ions were evaporated from the specimen, while in FIM analysis only the introduced imaging gases were ionized. Therefore, employing both FIM and APT to monitor chemical reaction process on surface allow us to detect the adsorbents, reactant, intermediates, and final product, which can be used to unravel the reaction mechanism further.

1.2.1 Field-Induced Ion Emission on Surface Reaction

Once a specimen surface is subjected to a high electric field, the introduced atoms and molecules may experience both: (a) a long-range, weak polarization force attracting them towards the apex via an electric field gradient; (b) a short-range, but strong chemical forces. The latter can result in the formation of chemical bond between gas and surface, and the strength is dependent on the gas activity with sample materials. Under this condition, the field-induced ion emission processes are defined by where the emission occurs and what is emitted. The basic types of field-induced ion emission can be classified into field desorption and field ionization (Figure 1.12). Field desorption refers to ions entity originally from a strong bound entity, while field ionization refers to the ions which are not bounded on the surface. The distinction between field ionization and field desorption is that the former involves both the bond-breaking and ionization, the latter only ionization [4].

Field ionization, that the ion ionization takes place at the so-called critical distance, is called surface field ionization. Field ionization that occurs far away from the surface is recognized as free-space field ionization.

Field desorption is subdivided according to the nature of ions constituents. In the cases that all the ions are the original part of the specimen, this process is field evaporation. If the entity is only the adsorbents on the emitter surface, this emission process is called adsorbate field desorption. Field etching or corrosion occurs as the ion entity is ions consisting of the adsorbents and emitter atoms, which may be derived from a chemical reaction.

The reaction between the reactants, products and surface perhaps leads to the adsorbate field evaporation, and field etching, which impede the study of *in-situ* observing the reaction process by APM.

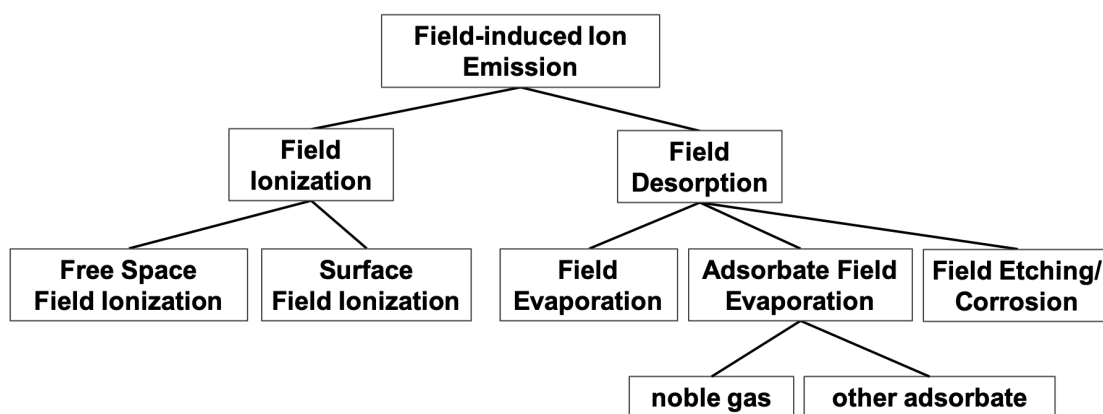


Figure 1.12 A classification of the different types of the field-induced ion emission.

1.2.2 Previous Studies of Reaction by APM

Even though the *in-situ* observation of reaction process by AP remains unsolved, several works about the studies of adsorption and reaction phenomena by other field emission techniques, such as FEM, FIM, and APFIM has been reported.

B. E. Nieuwenhuys group

B. E. Nieuwenhuys group from Gorlaeus Laboratorium (Leiden, The Netherlands) is one of the earliest groups to study gas chemisorption and dissociation phenomenon by field emission techniques. In the 1980s, the adsorption of CO, NO, N₂, H₂, H₂O, CO₂, and O₂ on the metals of Group VIII was investigated by FEM [26,27]. In their studies, the brightness of the field emission patterns changes at various stages of the interaction, resulting from each gas adsorption changing work function at a specific level. A saturated layer of CO, H₂, and NO at 300 K results in a work function increase of 0.98 eV, 0.21 eV, and 0.46 eV above that of the clean surface, respectively. The variety of the work function has a significant influence on local field strength, the close vicinity to the emitter metal surface. Work function changes could be estimated via the static voltage by using the Fowler-Nordheim equation. Here a simplified version of the Fowler-Nordheim equation to illustrate the work function and applied static voltage was shown as below,

$$\frac{\Delta\phi}{\phi_o} = \left(1 + \frac{\Delta V}{V_o}\right)^{2/3} - 1 \quad (1.4)$$

Where $\Delta\phi$ is the changing work function, ϕ_o is the average work function of the clean sample surface. Here for a constant current, V_o is the voltage at zero coverage, and ΔV is the change in voltage from that of a clean surface with imaging gas adsorption occurring.

B. E. Nieuwenhuys et al. [28] suggested that both H₂ oxidation reaction and CO oxidation reactions obey Langmuir-Hinshelwood (LH) mechanism, at which both components react with each other (adsorbed O and adsorbed H/CO) in the adsorbed state. In the case of NO and CO reaction, the dissociation of NO made reaction more active, where the dissociated and adsorbed O combined with intact CO molecule. Some research published in the 1990s revealed that on

Pd surface at 450 K encountered a reversible work function change of the order of 0.22 eV with introducing H₂ to the main chamber to react with NO. The NO can easily dissociate on Pd surface and the appearance of H₂ can remove the adsorbed N atom and O atom from the surface.

V. V. Gorodetskii

V. V. Gorodetskii (from Boreskov Institute of Catalysis, Novosibirsk, Russia) systematically investigated the oscillation phenomenon of CO oxidation on Pt surface by FEM and FIM during the 1990s and 2000s. His early studies showed that the local field was higher in the presence of an oxygen layer than that with a CO-covered adsorption layer. With the coexistence of O₂ and CO in the main chamber, ions were preferentially ionized at the oxygen-covered surface area. Upon increasing the sample temperature, the CO-oxidation oscillating reaction happened and the brightness of FIM images changed periodically[29–36].

As for the studies of the titration and oscillation phenomenon of the CO oxidation on Pt surface by FIM, the main results were summarized in Table 1.1

Apart from FIM and FEM, in V. V. Gorodetskii's research, various surface analysis techniques, such as high-resolution electron energy loss spectroscopy (HREELS), molecular beams (MB) and temperature-programmed reaction (TPR), were employed to investigate the CO oxidation reaction. He has cooperated with B. E. Nieuwenhuys group (mentioned above), J. H. Block group[29,34] (Fritz-Haber-Institut der Max planck-Gesellschaft, Germany), and F. Zeara group[30–33] (University of California, Riverside, USA) to finish all the research.

Table 1.1 Results of titration reaction

	CO_{ad} + O_{2 gas} reaction	O_{ad} + CO_{gas} reaction
reaction temperature	300-380 K	300-373 K
surface plane specificity	most active {110} least active {111}	reaction with CO _{gas} begins in the region of {110} plane
induction time	small at {110} {210} middle at {100} high at {111}	Absent
existence	boundary start at (110) and move to (113) →(210) →(111)	chaotic growth of CO _{ad} -island boundaries without crystallo-graphic specificity.
rate of the wave fronts	very fast at (100) plane	comparably much smaller
mechanism of wave propagation	surface mobility of CO _{ad} molecules	Growth of CO _{ad} -islands at proceeding titration reaction with mobile CO _{ad}
mechanism of sharp boundary appearance	adsorption and dissociation of impinging O ₂ molecules at immobile O _{ad} -island boarders	disappearance at the immobile layer

P. A. J. Bagot group

A new instrument called Catalytic Atom Probe (CAP) was developed by P. A. J. Bagot group at the University of Oxford [37,38], which aimed to eliminate the 'material gap' and 'pressure gap' in surface analysis. This new instrument is based on a 3DAP technique, which can provide intensive information about a 3D mapping of atom position and chemical information. A versatile gas reaction cell was constructed for 3DAP to enable a new method to study the reaction mechanism of heterogeneous catalysis. This gas reaction cell enables the metal specimen to expose to a pressure of up to 1 bar and a temperature range from room temperature to 873 K, which was well designed to study a wide variety of gas-surface interaction. As shown in figure 1.13, the reaction cell was installed on to the preparation chamber of the CAP. And the procedure for treating a specimen in the reaction cell was as follows:

- a. insert specimen into the main chamber
- b. clean specimen by field evaporation
- c. transfer the specimen to the preparation chamber
- d. prime gas-dosing rig with gases of interest and pre-heat the reaction cell
- e. transfer the specimen into reaction cell and admit gases to cell
- f. closed gases supply after holding for a required dosing time
- g. transfer the specimen to the main chamber via preparation chamber when the cell pressure drops below to 10^{-2} Pa.

The purification reaction of engine exhausting, NO_x , CO, and any unburnt hydrocarbons by platinum alloys, were investigated by CAP. The atomic-scale positional and chemical information for adsorbed gas and metal atoms/oxides from a specimen of interest were revealed as follows:

- a. NO and O_2 gases induced surface rearrangement in Pt. Especially in Pt-Rh surface, the Rh enrichment layer was observed at a temperature below 523 K, and the Rh-depleted was observed on {001}, {011} and {012} upon the temperature ranged from 573 K and 773 K.
- b. NO, O_2 and H_2O cause chemical segregation in Pt-Rh alloys.
- c. surface segregation behavior varied with surface orientation and treatment temperature.

d. CO and NO can co-exist on Pt-Rh alloys uncompetitively. CO, however, hindered oxidation layer formation on the catalyst surface.

The CAP appeared to be a powerful surface analysis technique to repeatedly compare a catalyst surface before and after the reaction at the atomic scale with a minimum risk of being contaminated. Besides, the reaction cell makes the reaction take place with large scales of pressure and temperature, which keeps the main chamber in a UHV condition. However, this leads to a ‘time gap’ between reaction and observation.

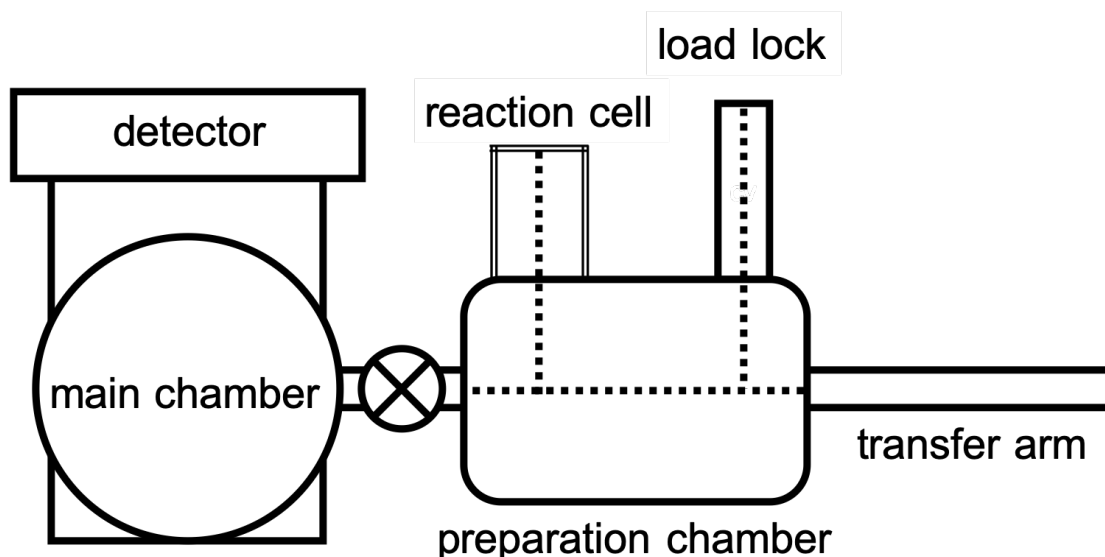


Figure 1.13 Schematic diagram of the chamber layout of the CAP (top view).

T.V. Bocarmé group

T.V. Bocarmé group, from Université libre de Bruxelles (Belgium) has been making efforts on reaction observation through field emission techniques. Professor Bocarmé had experience in P. A. J. Bagot group as a post-doctor researcher [37]. He participated in the construction of the CAP in the University of Oxford.

In the 2000s, T.V. Bocarmé et al. devoted to research concerning the H₂ oxidation, CO oxidation, and NO-H₂ reaction on Pt/Rh surface at high temperatures by FIM and a pulsed field desorption mass spectroscopy [39–49]. Here the pulsed field desorption mass spectroscopy refers to a 1DAP, by which only the ions from the selected area could be detected. In the study of water formation from H₂ and O₂ on Rh catalyst surface, the reaction was conducted in the 10⁻³ Pa at the temperature ranging from 400 to 600 K. The sample morphology changed during ongoing water formation. In that, on {011} and {113} planes, a polyhedral shape with missing-row-type reconstruction was formed.

In addition, the variation of gas mixture resulted into the occurrence of the local structure change with the reaction temperatures from 400 K to 500 K. Upon temperature up to 550 K, a self-sustained kinetic oscillation with a period of about 40 S took place with a specific mixture of H₂ and O₂ gas. Moreover, the formation of water was more active on an oxidized surface, where RhO⁺, RhO₂⁺, and Rh₂O⁺ could be detected. In CO oxidation study, Au carbonyl, such as AuCOⁿ⁺ and Au(CO)₂ⁿ⁺ formed on the Au surface at 300 K. Expose Au to a mixture of CO and O₂, CO and O₂ would competitively adsorbed on Au surface. With the pressure of O₂ ten times higher than that of CO, a weakly oxygen-covered surface established. Upon increasing the pressure of CO, this oxygen-covered surface would easily transfer to a CO-covered surface, which brought a chemical wave across the surface.

In the last decade, a series of researches were published concerning the hydrogenation of NO/NO₂ and the reaction between CO and H₂ on noble metal/alloy surface. The surface segregation caused by reaction or adsorption on alloy surface was also studied.

Conclusion

The field-induced ion emission of an on-going reaction on AP specimen surface is complicated. Extensive efforts have been made on gas adsorption and desorption processes on noble metals by FEM, FIM and 1DAP. The work function variation of metal surface caused by the gas adsorption has been clarified. The oscillation and bistability phenomena of CO oxidation, NO oxidation, NO hydrogenation on noble metal surface at high temperatures (about 300 K–700 K) have been systemically investigated. To overcome the ‘pressure’ gap, a CAP with a reaction cell installed close to the main chamber has been developed.

Besides, all the reaction processes mentioned above was observed by FIM, FEM or APFIM. The adsorption and desorption of reaction gas was judged by the brightness of the FEM images and FIM images. The surface composition only from the area of interest could be analyzed by a mass spectrometer via a probing hole. By far, no achievement had been realized to *in-situ* observe the reaction over a whole reaction surface. Moreover, few attentions have been paid to the reaction observation at cryogenic temperatures.

1.3 The Objective of This Research

This research aims to *in-situ* observe the surface reaction at a cryogenic temperature with atomic resolution by FIM and AP. As shown in figure 1.14, a FIM image is used to identify the surface morphology before a reaction conducted on the specimen surface. Then the selected reactant gases are introduced into the main chamber, making the reaction happen on the specimen surface by changing the specimen temperature. The variation of the chemical composition distribution on the specimen surface can be recorded by AP.

To achieve this goal, a proper and simple reaction should be chosen as a tentative model on the first try in AP analysis. The heterogeneous reaction (gas and solid) can be regarded as a suitable model to be studied. Therefore, the hydrogen oxidation or CO oxidation catalyzed by Pt metal were selected to be studied in this research. Besides, the hydrogen oxidation reaction and CO oxidation reaction with simple LH reaction mechanisms have been intensively investigated. The results from this research can therefore be used to compare with the previous research to examine the rationality and uniqueness of the AP method.

Besides, during AP analysis, the reaction surface is subjected to a high electric field and the pressure of reactant gas should be kept in vacuum condition (10^{-5} Pa to 10^{-6} Pa), which is different from the real reaction conditions. Therefore, the influence of the EF variation over specimen surface on active site identification should be explored. And during the AP experiment, the effects of the laser/voltage pulse, the surface corrosion caused by the reaction etc. will also be investigated.

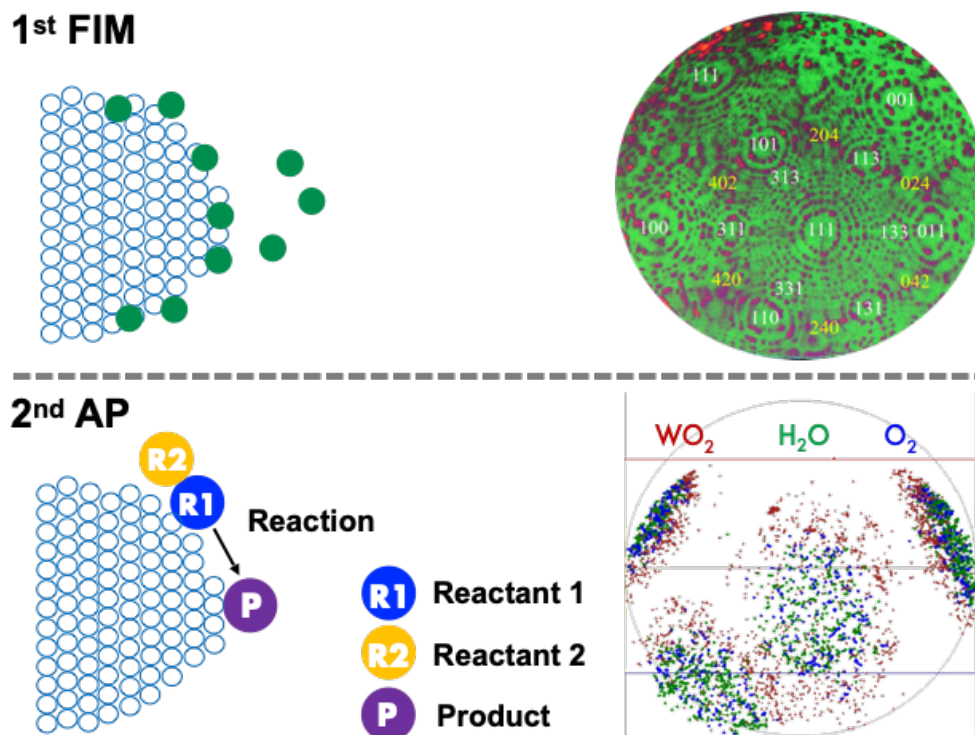


Figure 1.14 The experiment sequence: a FIM image of specimen surface is obtained to identify the surface structure; reactant gases are introduced into chamber, making the reaction happen on the specimen surface by changing the specimen temperature. The variation of the chemical composition distribution on specimen surface can be recorded by AP.

This thesis is composed of eight chapters as follows.

The emphasis was laid on the research background in chapter 1. The development history and underlying principle behind APM are introduced. The target of this research, previous works on adsorption and reaction studied by APM, and the difficulties of this research are clarified.

In chapter 2, the sample preparation method and the structure of the homemade AP is introduced. The laser system, gas introduction, operation protocol will be explained in detail.

The influence of EF variation over specimen surface on active site identification is investigated in chapter 3. A simulation method is established to calculate the EF distribution over an ideal hemisphere. An experimentally non-destructive method to evaluate the EF distribution on a sample surface based on the evaporation rate of ions in AP analysis is reported for the first time.

In chapter 4, the emphasis is put on the residual hydrogen behaviors in AP analysis. This study systematically evaluates EF effects on residual H signals in laser pulse mode.

A comparison between residual hydrogen signals and deuterium gas (D_2) signals is also performed to ascertain the source of the residual hydrogen. The author also discusses the adsorption and desorption of all hydrogen signals.

In chapter 5, the reaction of O_2 and H_2 on platinum was systematically studied. The Pt surface structure was determined by an FIM image. Then the reaction of O_2 and H_2 over platinum in high vacuum, at temperatures from 60 K to room temperature, was studied by FIM and AP. The reaction temperature and active sites are identified. In addition, the variations of reactant ion intensity and product ion intensity caused by laser pulse and voltage pulse were also investigated.

In chapter 6, the hydrogen oxidation reaction is conducted on Pt/Pd alloy and W metal surface. The reaction activity could be compared between Pt, Pt/Pd alloy and W sample surfaces.

In chapter 7, some experimental conditions of CO oxidation reaction studied by APM is explored.

At last, a conclusion of this research is made in chapter 8, the limitation of this characterization and a prospect will be made in the last chapter.

1.4 Reference

1. D. Phil Woodruff, *Modern Techniques of Surface Science* (Cambridge University Press, United Kingdom, 2016), Chapter 1.
2. B. Gault, M. P. Moody, J. M. Cairney and S. P. Ringer, *Atom Probe Microscopy* (Springer Science+Business Media, New York, 2012), Chapter 1.
3. T. F. Kelly and M. K. Miller, Atom probe tomography, *Rev. Sci. Instrum.* **78**, 031101 1–20 (2007).
4. M. K. Miller and R. G. Forbes, *Atom-Probe Tomography: The Local Electrode Atom Probe* (Springer Science+Business Media, New York, 2012), Chapter 1.
5. J. H. Winkler, G. Eigenschaften, Wirkungen und Ursachen der Electricitat nebst Beschreibung aweir electrischer Maschinen (Verlag B. Ch. Breitkopf, Leipzig, 1744).
6. J. J. Thomson, Cathode Rays. *Philos. Mag.* **44**, 293(1897).
7. J. E. Lilienfeld, The auto-electronic discharge and its application to the construction of a new form of x-ray tube. *Am. J. Roentgenol*, **9**, 172–179(1922).
8. R. A. Millikan, C. C. Lauritsen, Relations of Field-Currents of Thermionic-Currents. *Proc. Natl. Acad. Sci. U.S.A.* **14**, 45 (1928).
9. R. H. Fowler, L. Nordheim, Electron emission in intense electric fields. *Proc. R. Soc. Lond. A*, **119**, 173 (1928)
10. E. W. Müller, Elektronenmikroskopische Beobachtungen von Feldkathoden. *Z. Phys.* **106**, 541–550 (1937).
11. E. W. Müller, Work Function of Tungsten Single Crystal Planes Measured by the Field Emission Microscope. *J. Appl. Phys.* **26**, 732–737 (1955).
12. K. Bahabur, *Experimental Investigation of Field Ion Emission*. Ph.D Thesis, Pennsylvania State University, 1955.
13. E. W. Müller, K. Bahadur, Field Ionization of Gases at a Metal Surface and the Resolution of the Field Ion Microscope. *Phys. Rev.* **102**, 624–631 (1956).
14. M. K. Miller, *Atom Probe Tomography: Analysis at the Atomic Level* (Springer Science+Business Media, New York, 2000), Chapter 3.
15. E. W. Müller, T. T. Tsong, *Field Ion Microscopy* (Elsevier, New York, 1969).
16. R. G. Forbes, PhD. Thesis, Cambridge University, 1970.

17. R. G. Forbes, Field-ion imaging old and new. *Appl. Surf. Sci.* **94–95**, 1–16 (1996).
18. T. T. Tsong, Atom-probe field ion microscopy (Cambridge University Press, New York, 1990)
19. E. W. Müller, The Atom-Probe Field Ion Microscope. *Rev. Sci. Instrum.* **39**, 83–86(1968).
20. N. Mayama, Y. Kajiwara, S. Mikami, S. Ito, T. Kaneko, T. Iwata and M. Owari, Improvement of Mass Resolution in Wide-Angle Laser-Assisted Atom Probe by Flight Path Compensation. *e-J. Surf. Sci. Nanotech.* **7**, 35–38 (2009).
21. M. Lampton, O. Siegmund and R. Raffanti, Delay line anodes for microchannel-plate spectrometers. *Rev. Sci. Instrum.* **58**, 2298–2305 (1987).
22. O. Jagutzki, V. Mergel, K. Ullmann-Pfleger, L. Spielberger, U. Spillmann, R. Dörner, H. S. Böcking, A broad-application microchannel-plate detector system for advanced particle or photon detection tasks: large area imaging, precise multi-hit timing information and high detection rate. *Nucl. Instrum. Meth. A*, **477**, 244–249 (2002).
23. A. Oelsner, O. Schmidt, M. Schicketanz, M. Klais, and G. Schönhense, Microspectroscopy and imaging using a delay line detector in time-of-flight photoemission microscopy. *Rev. Sci. Instrum.* **72**, 3968–3974 (2001).
24. G. Da Costa, F. Vurpillot, A. Bostel, M. Bouet, and B. Deconihouta, Design of a delay-line position-sensitive detector with improved performance. *Rev. Sci. Instrum.* **76**, 013304-1–8(2005).
25. J. Takahashi, K. Kawakami, Y. Kobayashia and Toshimi Tarui, The first direct observation of hydrogen trapping sites in TiC precipitation-hardening steel through atom probe tomography. *Scripta Mater.* **63**, 261–264 (2010).
26. P. D. Cobden, E. E. Nieuwenhuys, V.V. Gorodetskii, Adsorption of some small molecules on a Pd field emitter. *Appl. Catal. A-Gen.* **188**, 69–77 (1999).
27. B. E. Nieuwenhuys, Adsorption and reaction of CO, NO, H₂ and O₂, ON group VIII metal surface. *Surf. Sci.* **126**, 307–336, (1983).

28. M. F. H. van Tol, P.T. Wouda and B.E. Nieuwenhuys, Oscillating behavior of NO reduction reactions over rhodium studied on the atomic level. *J. Vac. Technol. A* **12**(4), 2176–2182 (1994).
29. V. Gorodetskii, W. Drachsel, M. Ehsasi, and J. H. Block, Field ion microscopic studies of the CO oxidation on platinum: Bistability and oscillations. *J. Chem. Phys.* **100**, 6915–6922(1994).
30. V. V. Gorodetskii and B. E. Nieuwenhuys, Chemisorption and dissociation of carbon monoxide on Rhodium surface. *Surf. Sci.* **105**, 299–312 (1981).
31. V. V. Gorodetskii and B. E. Nieuwenhuys, W. M. H. Sachtler and G. K. Boreskov, Adsorption of hydrogen on Rhodium: comparison with hydrogen adsorption on platinum and iridium. *Surf. Sci.* **108**, 225–234 (1981).
32. V.V. Gorodetskii and B. E. Nieuwenhuys, W. M. H. Sachtler and G. K. Boreskov, Adsorption of oxygen and its reactions with carbon monoxide and hydrogen on rhodium surfaces: comparison with platinum and iridium. *Surf. Sci.* **7**, 355–371 (1981).
33. V.V. Gorodetskii, V.I. Elokhin, J.W. Bakker, B.E. Nieuwenhuys, Field electron and field ion microscopy studies of chemical wave propagation in oscillatory reactions on platinum group metals. *Catal. Today* **105**, 183–205 (2005).
34. V. Gorodetskii, W. Drachsel and J.H. Block, Imaging the oscillating CO-oxidation on Pt-surfaces with field ion microscopy. *Catal. Lett.* **19**, 223–231 (1993).
35. V.V. Gorodetskii, W. Drachsel, Kinetic oscillations and surface waves in catalytic CO+O₂ reaction on Pt surface field electron microscope, field ion microscope and high resolution electron energy loss studies. *Appl. Catal. A-Gen.* **188**, 267–275(1999).
36. V.V. Gorodetskii, A.V. Matveev, E.A. Podgornov, and F. Zaera, Study of the low-temperature reaction between CO and O₂ over Pd and Pt surfaces. *Top. Catal.* **32**, 17–28 (2005).
37. P.A.J. Bagot, T. V. Bocarmé, A. Cerezo, G.D.W. Smith, 3D atom probe study of gas adsorption and reaction on alloy catalyst surfaces I: Instrumentation. *Surf. Sci.* **600**, 3028–3035 (2006).

38. P.A.J. Bagot, A. Cerezo, G.D.W. Smith, 3D atom probe study of gas adsorption and reaction on alloy catalyst surfaces II: Results on Pt and Pt–Rh. *Surf. Sci.* **601**, 2245–2255 (2007).
39. C. Barroo, S. V. Lambeets, F. Devred, T. D. Chau, N. Kruse, Y. De Decker and T.V. Bocarme, Hydrogenation of NO and NO₂ over palladium and platinum nano-crystallites: case studies using field emission techniques. *New J. Chem.* **38**, 2090–2097.
40. S. V. Lambeets , T. V. Bocarmé, N. Kruse and D. E. Perea, Surface/subsurface interactions during Rh oxidation revealed by atom probe tomography and microscopy. *Microsc. Microanal.* **25**, 330–331(2019).
41. S. V. Lambeets, C. Barroo, S. Owczarek, N. Kruse and T. V. Bocarmé, Subsurface oxygen formation during H₂ oxidation over Rh, Pt and Pt-Rh model nanoparticles.. *Microsc. Microanal.* **24**, 1948–1949 (2018).
42. S. V. Lambeets , C. Barroo, S. Owczarek, L. Jacobs, E. Genty, N. Gilis, N. Kruse and T. V. Bocarmé, Adsorption and hydrogenation of CO₂ on Rh nanosized crystals: demonstration of the role of interfacet Oxygen Spillover and Comparative Studies with O₂, N₂O, and CO. *J. Phys. Chem. C* **121**, 16238–16249(2017).
43. L. Jacobs, C. Barroo, N. Gilis, S. V. Lambeets, E. Genty and T. V. Bocarmé, Structure reactivity relationships during N₂O hydrogenation over Au-Ag alloys: a study by field emission techniques. *Appl. Surf. Sci.* **435**, 914–919(2018).
44. T. D. Chau, T. V. Bocarmé and N. Kruse, Kinetic instabilities in the NO/H₂ reaction on platinum. *Surf. Interface Anal.* **36**, 528–532(2004).
45. T. V. Bocarmé, T. D. Chau and N. Kruse, Imaging and probing catalytic surface reactions on the nanoscale: Field Ion Microscopy and atom-probe studies of O₂–H₂/Rh and NO–H₂/Pt. *Top. Catal.* **39**, 111–120(2006).
46. T. Bär, T. V. Bocarmé, B. E. Nieuwenhuys and N. Kruse, CO oxidation on gold surfaces studied on the atomic scale. *Catal. Lett.* **74**, 127–131(2001).
47. V. K. Medvedev, Y. Suchorski, C. Voss, T. V. Bocarmé, T. Bär and N. Kruse, Oxygen-induced reconstruction and surface oxidation of rhodium. *Langmuir* **14**, 6151–6157(1998).

48. T. V. Bocarmé, G. Beketov and N. Kruse, Water formation from O₂ and H₂ on Rh tips: studies by field ion microscopy and pulsed field desorption mass spectrometry. *Surf. Interface Anal.* **36**, 522–527 (2004).
49. T. V. Bocarmé, T. D. Chau and N. Kruse, The interaction of CO–O₂ gas mixtures with Au tips: *in situ* imaging and local chemical probing. *Surf. Interface Anal.* **39**, 166–171 (2007).

CHAPTER 2 EXPERIMENTAL METHOD

The AP specimen preparation method and AP experimental protocol are explained in this chapter in detail. The AP instrument in our lab has been designed, assembled, and modified by our members since 2006. The various hardware components and the operation principle of AP are clearly introduced in **section 2.3**.

2.1 Specimen Preparation Methods

In the AP experiment, a specimen sharpness is the key to a successful experiment. The elementary geometry of an AP specimen is a sharp needle, whose taper is a modest angle ($<10^\circ$ semi-angle) to an apex between 50 and 150 nm radius. The surface of the specimen should be smooth and free from protrusions, grooves or cracks, which lead to artefacts in data reconstruction and rupture caused by stress concentration [1, 2].

In the development of the preparation method, there has been an explosion of new ideas and methods for AP specimen preparation, such as electropolishing method, broad ion beam, and focused ion beam (FIB) method. Among all these methods, the electropolishing method and FIB-based method are regarded as the primary methods [1].

2.1.1 Electropolishing Method

The electropolishing method is the most conventional method for preparing needle-shaped AP specimen. This method refers to an electrochemical process in which the material is immersed in an electrolyte and supplied by a direct current(DC) or alternating current (AC) power together with a counter electrode. Therefore, it requires the material possesses great electrical conductivity, and metal wires are commonly used in AP specimen preparation[3].

The general experimental set-ups of the electropolishing are shown in the figure 2.1. Traditionally, a double-layer method was employed for rough polishing. A layer of electrolyte is used to break the wire into two parts or significantly reduce the central region. In the fine electropolishing process, only the very front part of the specimen is dipped into electrolyte. If the diameter of the metal wire is small enough, the rough electropolishing step can be omitted. Another widely used set-up for the fine

electropolishing is exhibited in figure 2.2. The electrolyte is suspended within a wire loop, and the specimen is repeatedly dipped into the wire loop and polished until the tip is sharp enough for AP analysis. This method is also referred to as micro-polishing.

The current density curve as a function of applied voltage is shown in figure 2.3. The curve can be divided into three sections. In the lower voltage region (A–B), the reactive points on the surface of the needle are preferentially dissolved, which is called etching process. It cannot result into an smooth and shiny surface. The region BC is the polishing plateau which is the optimal conditions for electropolishing. At high voltage (C–D), the pitting occurs. The precise shape of the curve relies on the nature of materials and electrolytes. And the temperature also affects the current-voltage curve.

The type of electrolyte, the solution, and the concentration of electrolyte are heavily dependent on the materials and electropolishing steps. Some recommended electrolytes and conditions for various materials are provided as a guide in appendix E. The success rate and sample shape heavily depend on practical skills [1, 2].

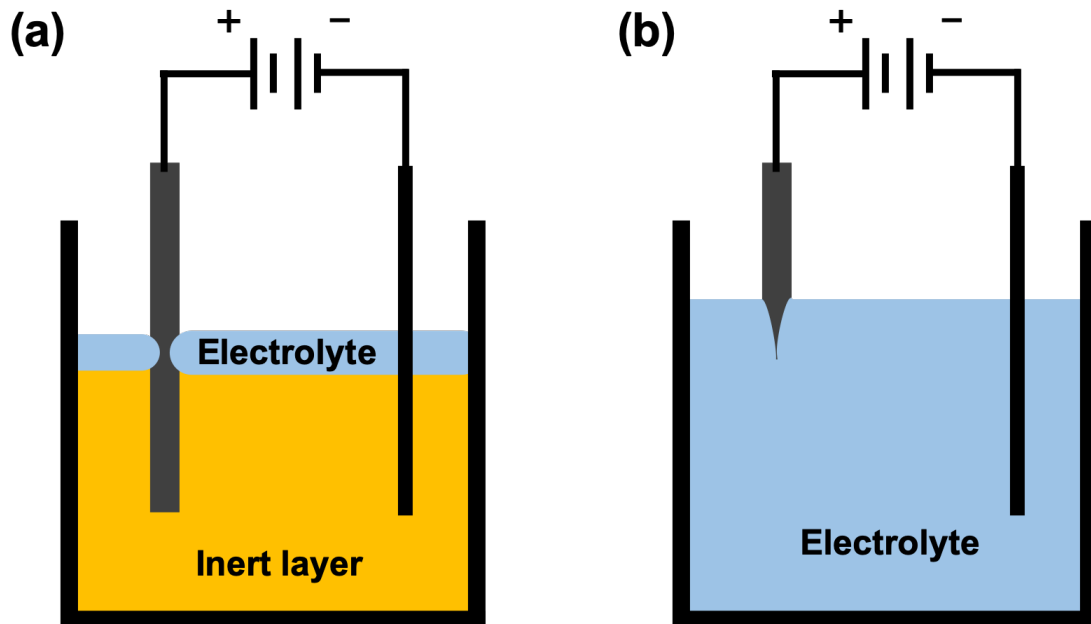


Figure 2.1 (a) a double layer electropolishing method; (b) a fine electropolishing method.

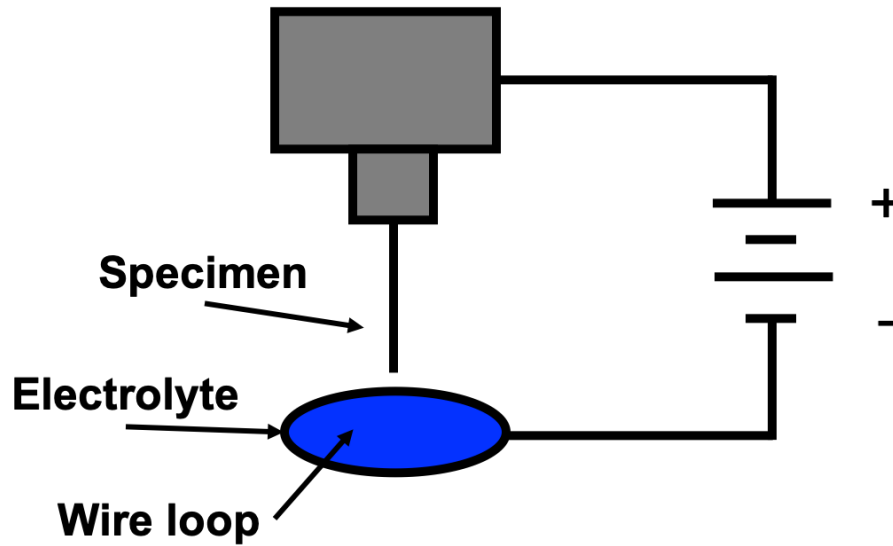


Figure 2.2 A schematic diagram of micro-polishing method.

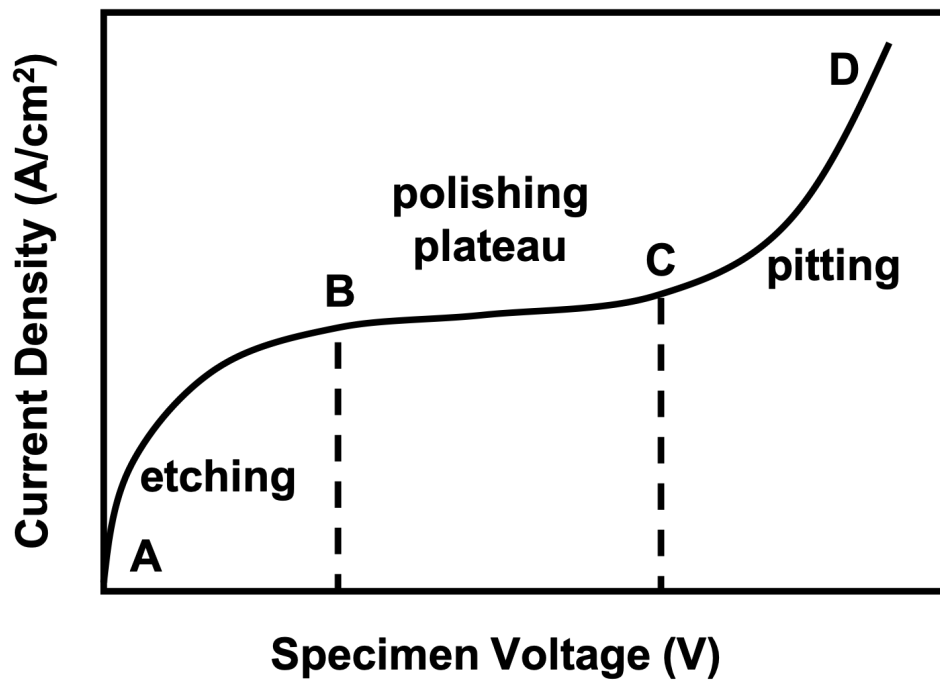


Figure 2.3 A change in current with applied voltage in a typical electropolishing process: (A–B): etching takes place at lower voltages; (B–C): optimum electropolishing can be conducted; (C–D): pitting occurs at higher voltages.

2.1.2 Focused Ion Beam Based Method

FIB-based method has emerged as one of the most useful methods for shaping nanomaterials for its versatility. It involves removing materials from a bulk to make a

specimen or being employed as final step for an electropolished specimen to correct the artifacts. FIB method makes it possible to fabricate atom probe specimens from a significantly more extensive range of materials and alternative specimen geometries than traditional electropolishing methods. Not only metals, even the semiconductor and insulator can be analyzed by AP. Besides, by the FIB method, a specific area in materials can be selected, such as multilayer film, interphase interfaces and heterogeneously distributed phase.[1,4]. A FIB instrument with SEM built-in is used worldwide as shown in figure 2.4. Usually, the stage can rotate up to 50 ° in operation, and the SEM can monitor the sample preparation process.

A lift-out method developed by Thompson et al. has been widely adopted by AP community since 2007[5]. This method involves transferring a section of interest to a prefabricated Si or W post by temporarily welding the sample to the manipulator, putting it on a post, and then annular milling it to a needle-shaped AP specimen. Figure 2.5 shows a series of images of the lift-out process. This method can choose the material to be analyzed with excellent site specificity and positional accuracy. Now the lift-out method has been automated, which is the final step of the automated AP sample preparation process.

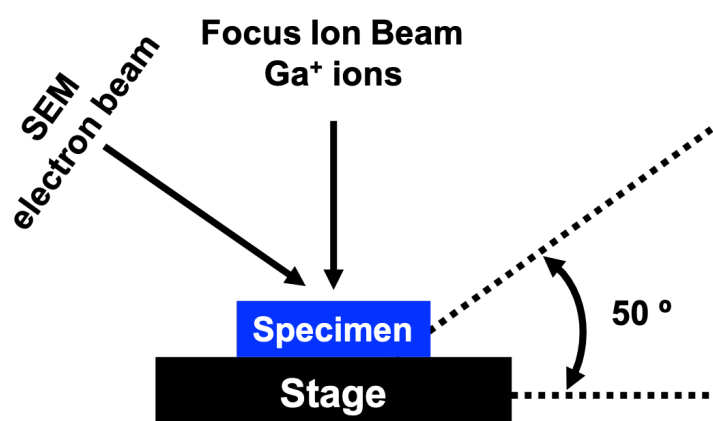


Figure 2.4 A schematic diagram of FIB-SEM instrument.

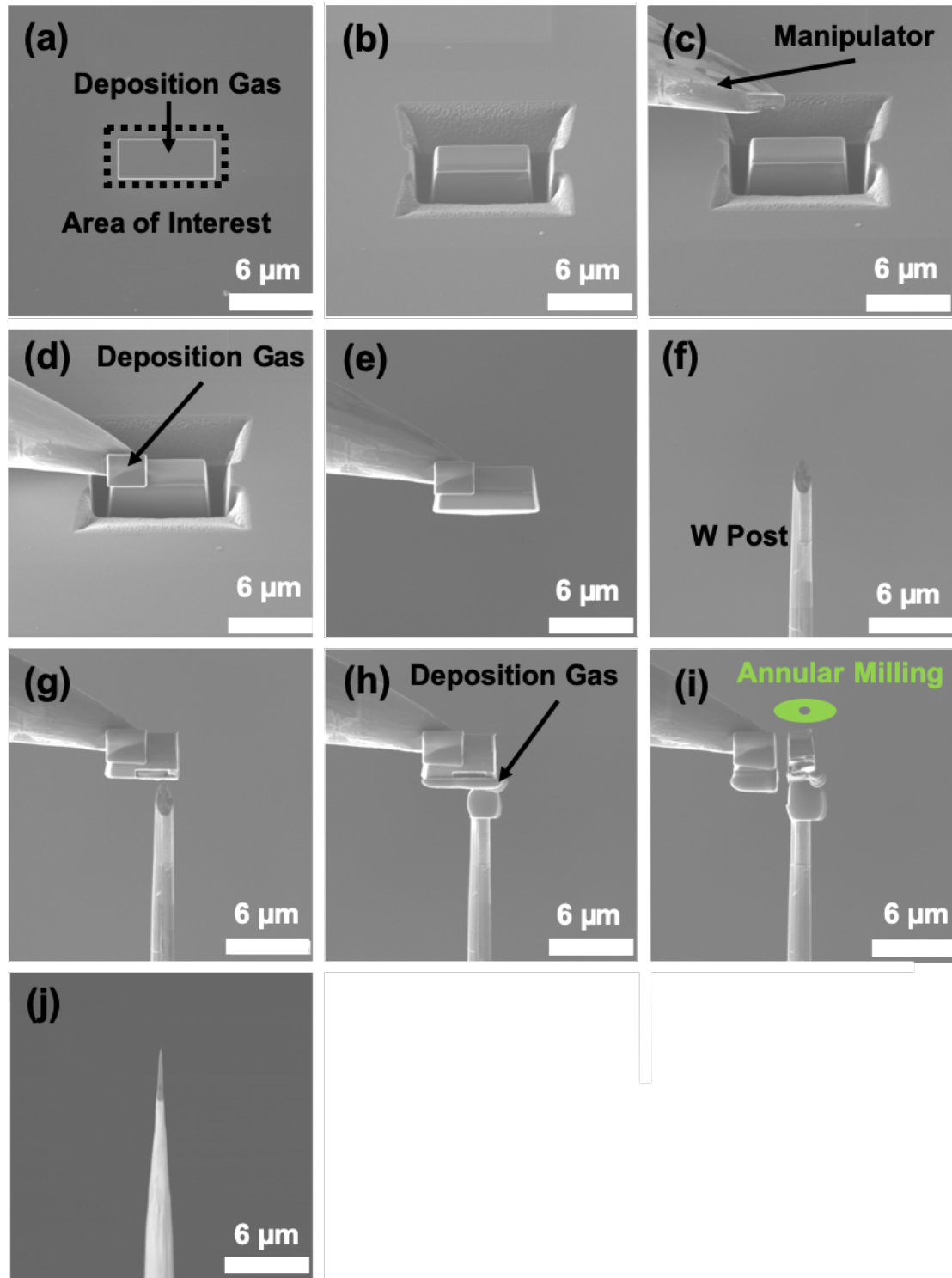


Figure 2.5 SEM image of the steps of the lift-out method. (a) a lay of Pt deposit on the targeted area ; (b) lifting the material out; (c) a manipulate; (d) welding the material to the manipulator; (e) picking the material out; (f) W post; (g) the material positioned on the post; (h) welding the material to the post; (i) manipulator cut-free and rest of material left at the top of the support post; (j) final specimen prepared by annular milling.

2.2 Specimen Preparation in This Research

In this research, three kinds of metals, platinum (Pt), platinum (80 %)-palladium (20 %) (PtPd) alloy, and tungsten(W), are chosen as experimental materials. The specific preparation methods of these three metals will be introduced as follows.

2.2.1 The Preparation Method of Tungsten

Only the electropolishing method was employed in the process of W preparation. As shown in figure 2.6, a W wire (Nilaco, $\phi = 0.1$ mm, 99.99%), is immersed in 100 % saturated sodium hydroxide (NaOH) electrolyte [6]. The electrolyte and the other end of W wire are connected to alternative current. The current is controlled between 3 V and 5 V. During electropolishing process, the immersed W will be gradually corroded, and the electropolishing should be ended at the point that all the immersed part disappears. Close attention should be paid at the last stage, in that the sharpness of the nanosized W is fragile. By this method, the final radius of the W specimen is below 50 nm.

Electropolish

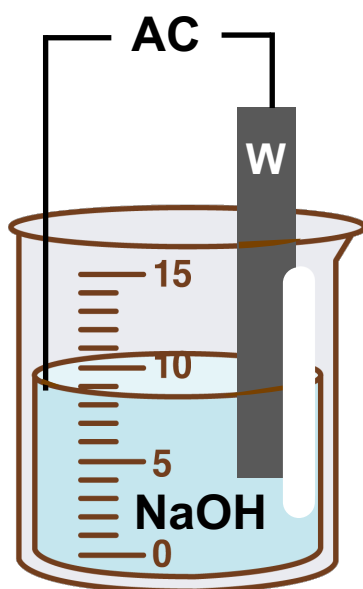


Figure 2.6 The schematic diagram of W preparation by electropolishing method. The W wire ($\phi = 0.1$ mm) is immersed in 100 % saturated NaOH electrolyte. The electrolyte and the other end of W wire are connected to alternative current (3 V–5 V).

2.2.2 The Preparation Methods of Platinum and Platinum/Palladium Alloy

In the Pt specimen fabrication process, both electropolishing method and FIB method are employed. Platinum tips were prepared as shown in figure 2.7. Pt (Nilaco, $\phi = 0.1$ mm, 99.99%) wire is tightly fixed in a copper holder. The Pt wire is suspended in a layer of 100 % saturated CaCl_2 electrolyte that is floated in a carbon electrode [4]. The carbon electrode and the other end of Pt wire (or copper holder) are connected to alternative current (5 V–10 V). After electropolishing, a focused ion beam scanning electron microscope (FIB-SEM, SII Nanotechnology Inc., SMI-3050 SE) with a gallium liquid metal ion source (LMIS) is employed to cut the Pt tip with a cone shape to $4\text{ }\mu\text{m} \times 2\text{ }\mu\text{m} \times 2\text{ }\mu\text{m}$ cuboid standing on Pt wire (figure 2.7d and figure 2.8a). The cuboid is sharpened into the AP needle-shaped specimen by an annular milling technique, in which the outer and inner diameters of a circular mask and the milling current should be set to decrease progressively (figure 2.7e and figure 2.8b).

As for the PtPd alloy, the fabrication process is almost as same as that of Pt. In the case of PtPd alloy, the electropolishing time is longer because the PtPd alloy is hard to be corroded.

Finally, the diameter of the sample tip was measured by TEM (JEOL, JEM1010), as shown in figure 2.9.

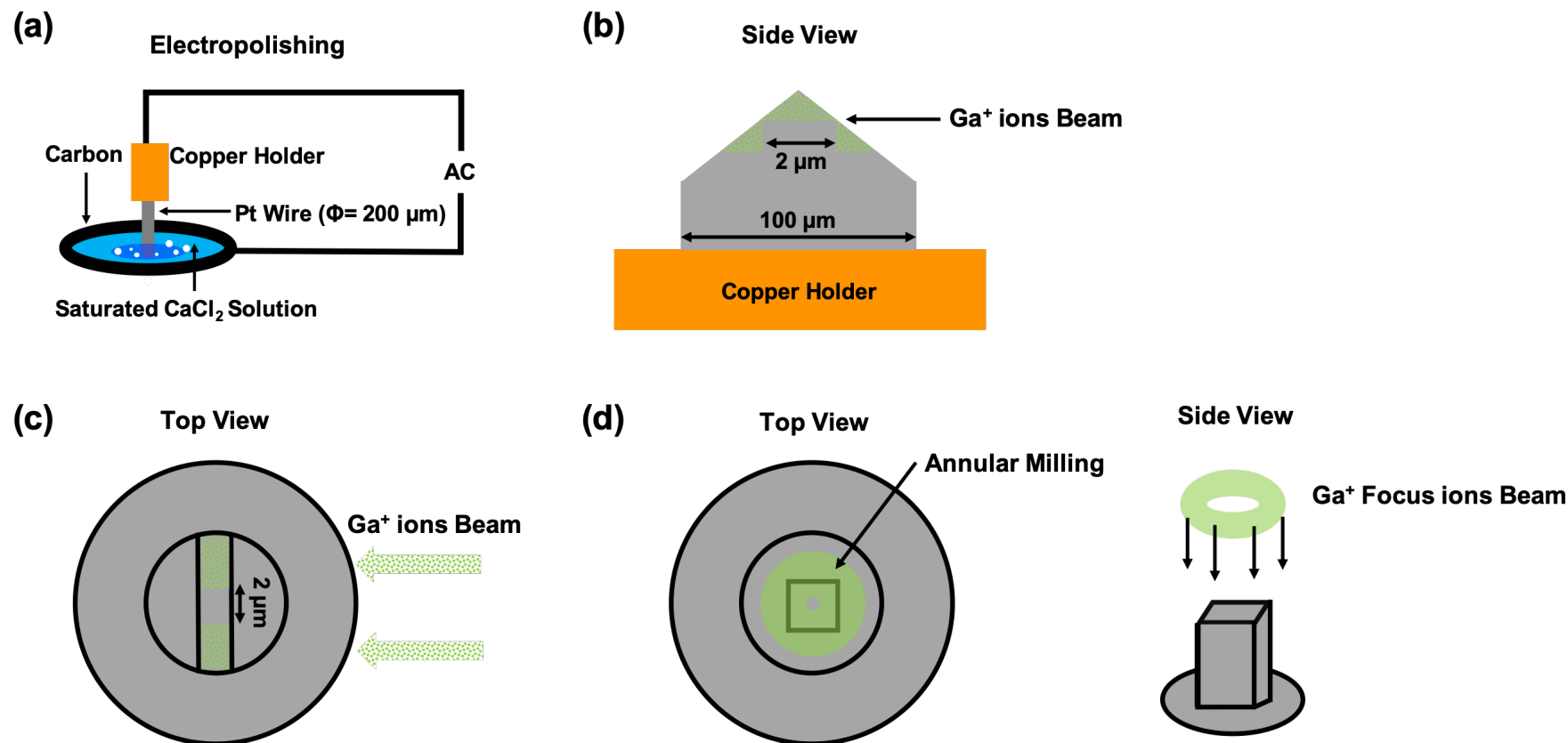


Figure 2.7 (a) The schematic diagram of Pt preparation by electropolishing method. Pt is tightly fixed in a copper holder. The Pt wire ($\phi = 0.1 \text{ mm}$) is suspended in a layer of 100 % saturated CaCl_2 electrolyte that is floated in carbon electrode. The carbon electrolyte and the other end of Pt wire (or copper holder) are connected to alternative current (5 V–10 V). (b) and (c): after electropolishing, the Ga^+ focus ions beam is employed to cut the Pt tip with a cone sharp to $4 \mu\text{m} \times 2 \mu\text{m} \times 2 \mu\text{m}$ cuboid standing on Pt wire. (e) The cuboid is sharpened into the AP needle-shaped specimen by an annular milling technique.

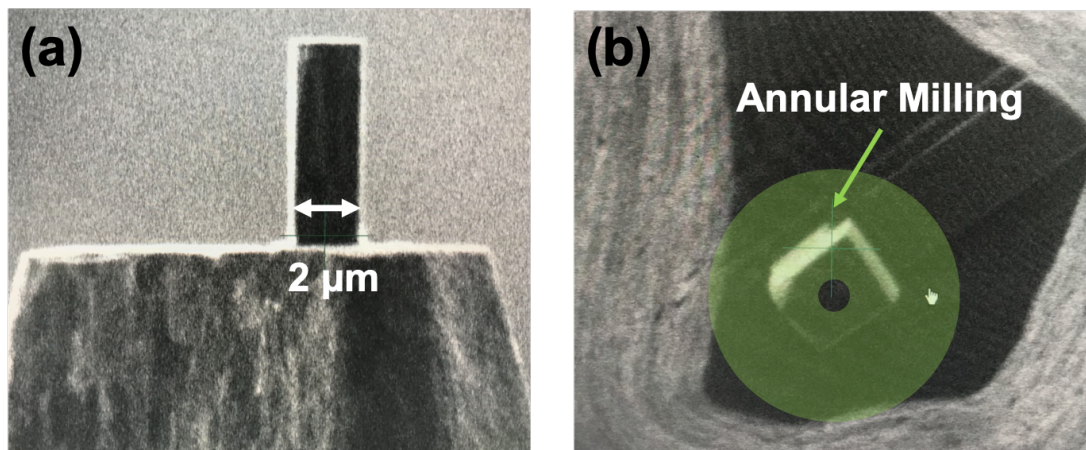


Figure 2.8 The SEM images of Pt specimen in FIB process: (a) the Pt specimen after the (c) step in figure 2.7 ; (b) the top view of Pt specimen before annular milling.

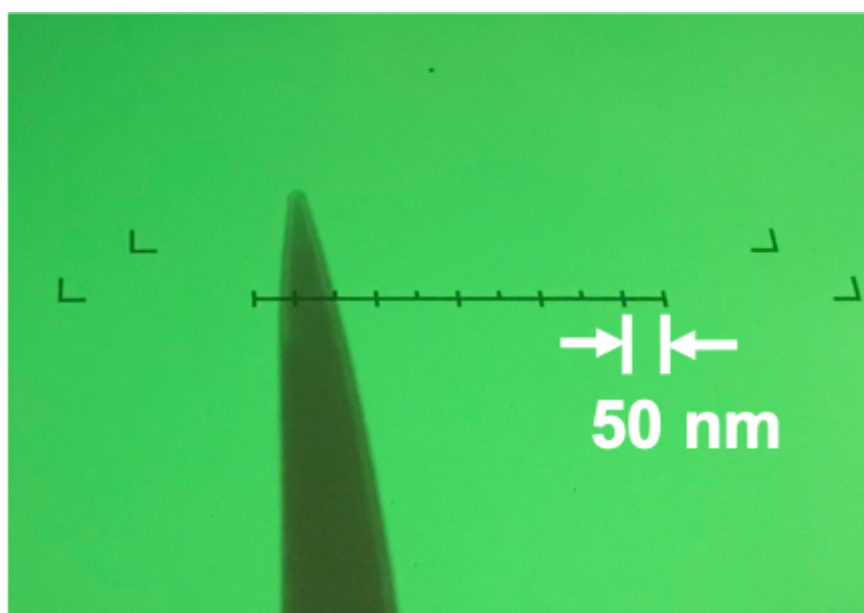


Figure 2.9 TEM image of the Pt specimen with a radius below 50 nm for AP analysis.

2.3 Atom Probe Instrument

The AP instrument in our lab has been designed, assembled and modified by our members since 2006 [7-9].

The AP consists of three chambers: the main analysis chamber including the specimen stage, cryostat, FIM system, and mass spectrometer, an optional preparation chamber for transferring and storing specimen prior to analysis, and a fast entry airlock for quickly introducing and removing specimen, as shown in figure 2.10.

The vacuum system of the main chamber is designed to operate at ultra-high vacuum (UHV), which could be down to 10^{-8} Pa in AP analysis. The pressure is measured by means of a Bayard-Alpert ion gauge. Four turbomolecular pumps (TMP) work together to keep the main chamber in UHV condition. Besides, the construction and all the internal components are capable to be operated under UHV condition without significant outgassing. The vacuum vessel is constructed from welded stainless steel tubes with titanium coating inside. The typical materials used in UHV are copper, alumina, stainless steel, sapphire, machinable glass, and Kapton® or polytetrafluoroethylene (PTFE) insulations. Baking the vacuum chamber out is a normal step to remove the leftover every time the vacuum chamber is exposed to atmosphere. The vacuum vessel is usually heated up to 200 °C–300 °C for several hours, and the maximum bakeout temperature is 300 °C limited by MCP, as a higher temperature damages its detection efficiency. Bakeout can significantly shorten the pumping time, because this process dramatically increases the desorption and diffusion rates. The pressure of the optional preparation chamber is kept at 10^{-5} Pa, and the pressure of the fast entry airlock is about 1 Pa by a rotary pump (RP) during sample transferred into the preparation chamber. The optional preparation chamber and fast entry airlock chamber are mainly used for sample exchange. This structure can keep the UHV of the main chamber.

A schematic diagram of main chamber and all the components connected to main chamber is exhibited in figure 2.11. The sample stage, cryostat system, gas introduction system, voltage system, laser pulse, ion detection system, and data analysis methods will be explained in detail.

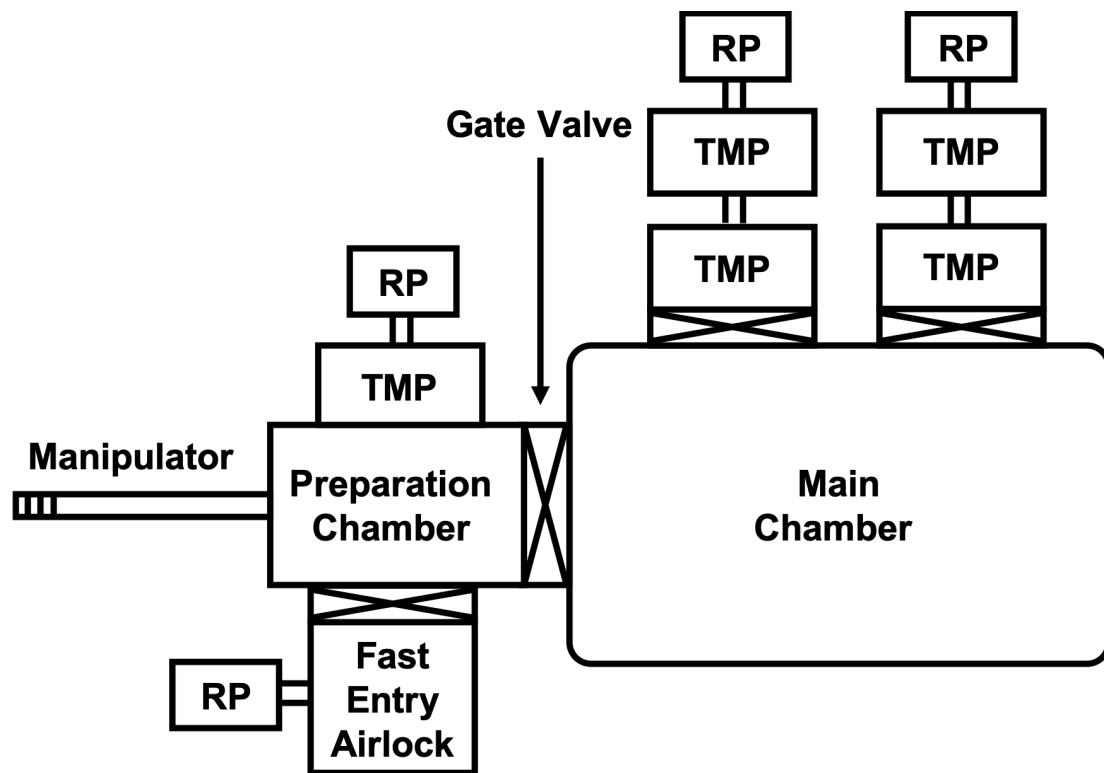


Figure 2.10 A schematic diagram of chamber systems.

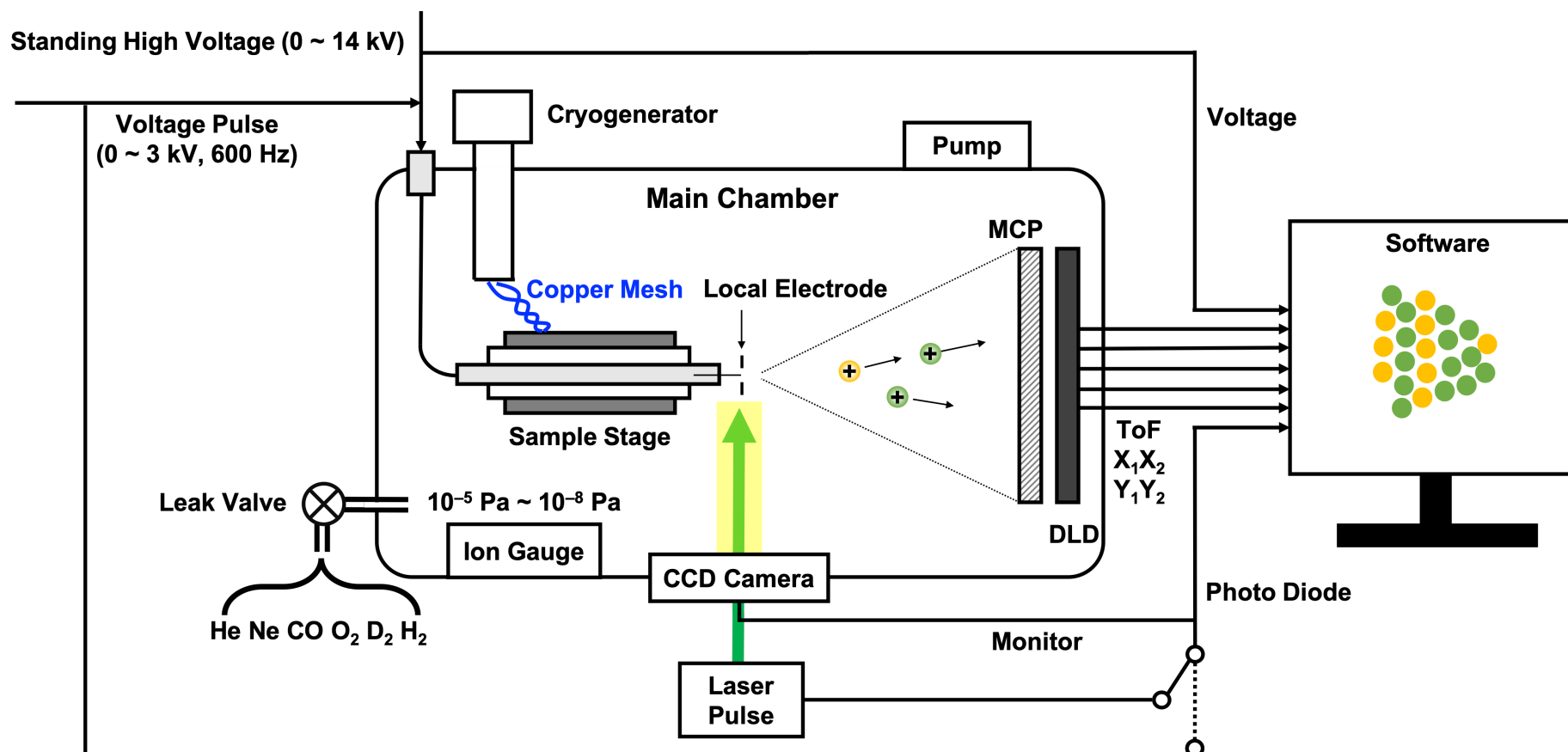


Figure 2.11 A schematic diagram of the AP in our lab.

2.3.1 Sample Stage

The sample holder was originally developed by this group. As shown in figure 2.12, it is in a cylindrical shape and consists of two metal layers made of copper and an insulating part made of ceramic residing between two metal layers. The inside metal layer can connect to high voltage and the insulator prevents the high voltage from leaking to the outside. This sample holder is equipped with a local electrode with a hole of 200 μm diameter[10]. The tip of the specimen should be adjusted on the central axis of the electrode with a distance of 50 μm away from the electrode. Therefore, most ions can pass through the electrode and be detected by PSD. The local extraction electrode was originated by Prof. Nishikawa in Kanazawa Institute of Technology [15]. Actually, a local electrode is not necessary for APT. The benefit of local electrode might be the localization of electric field to a small region around tip apex. And it increase the local electric field on the sample surface in order to reduce the possibility of tip fracture. The local electrode has got common tool by being introduced in local electrode atom probe (LEAP) by IMAGO company of USA, now a division of CAMECA company.

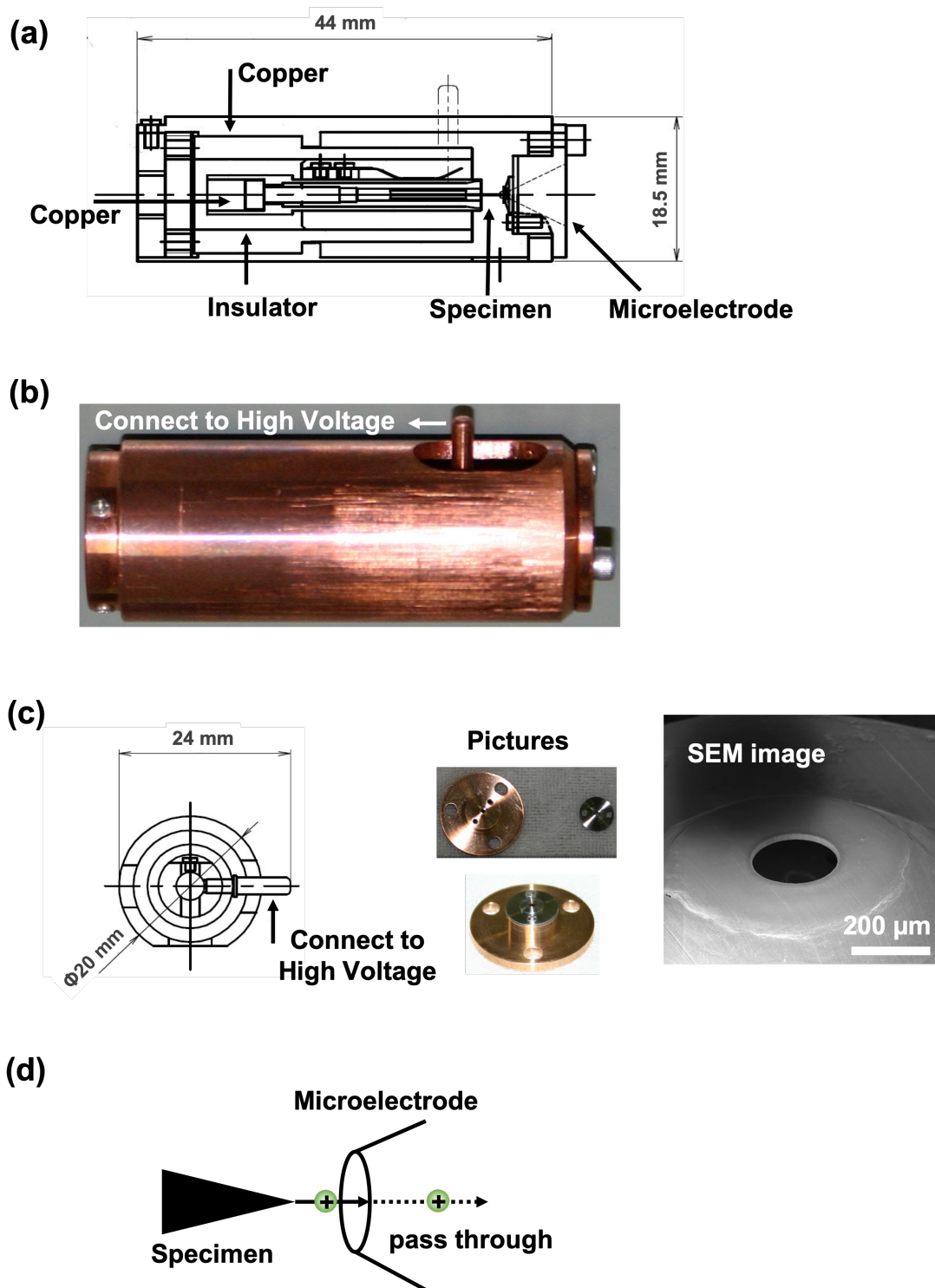


Figure 2.12 (a) a schematic diagram of the sample stage; (b) the image of the sample stage; (c) a schematic diagram, pictures, and SEM image of the local electrode; (d) the electrode allowing ions to pass through.

2.3.2 Cryostat

A standard operation temperature of FIM and AP should be below 70 K. A commercial closed-cycle helium (He) cryogenerator is employed to control the temperature of the sample. In this cycle, the He gas is first compressed by a piston and the heat of the compression is removed by a heat exchanger. Then the compressed He is subsequently to expand and extracts the heat from sample holder end. The cryogenerator and sample holder are connected by a copper mesh. The soft copper mesh can weaken the vibration effects caused by the piston, thereby make sample holder vibration-insensitive. In addition, the copper mesh with the temperature lower than 60 K can work as a sublimation pump to condense some gas its cold surface.

2.3.3 Position Sensitive Detector

The position sensitive detector(PSD) consists of MCP in chevron configuration (v-like) and 12 cm DLD (Roentdek, DLD120) with improved multi-hit capabilities, high time resolution (25 ps), and high position resolution (100 μm), as shown in figure 2.15. The ToF signal from MCP and four signals (X_1 , X_2 , Y_1 , Y_2) from DLD is transferred to computer through the time-to-digital converter (TDC).

The operation principle of MCP is shown in figure 2.13. The MCP set in this PSD is consist of two microchannel plates with angled channels rotated 180° from each other in a chevron shape. The two MCPs are stacked closely to improve spatial resolution. Every single MCP, a planar component, is employed to amplify the signal of each particle, such as electron, ion, and neutron, and the radiation like X-ray. In each MCP plate, an array of a large number of separated electron multipliers channels ($\phi = 8 \mu\text{m}$) parallelly crosses the plate. As a single incident particle enters a channel, 2-3 electrons emits from the channel wall due to a high-resistance semiconductor coated on the inside wall of each channel. A positive voltage (2375 V) is applied on the outlet side (back) of MCP, while the inlet side (front) is grounded. The emitted electrons will accelerate and travel along in channel via a positive bias voltage and repeatedly strike the inside wall to produce more secondary electrons, called the cascade process. As a result, the output can be as 10^3 times as the input signal[11–12].

The operation principle of DLD is shown in figure 2.14. The critical component of DLD is two sets of parallel-pair delay-line (X and Y) independently fixed on the

holder (figure 2.14a). The delay line is made of copper with a diameter of 100 μm , wound on the DLD holder. 4 sets of delay liners, X_1 , X_2 , Y_1 , and Y_2 , are isolated from each other. A high voltage (2625 V) is applied to each delay line, and 2375 V to DLD holder. When an electron beam hit the DLD, both X delay lines and Y delay lines receive the current. Take Y delay line as an example (figure 2.14b), as an electric cloud induces two electric signals, they can propagate along the Y delay line to Y_1 end and Y_2 . This difference in propagation times can be used to identify the electron beam position, Y_D in Y-axis according to

$$Y_D = L_Y \frac{(T_{Y_1} - T_{Y_2})}{2T_Y} \quad (2.1)$$

where L_Y is the physical length of the line, T_{Y_1} and T_{Y_2} are the times of Y_1 end and Y_2 end, T_Y is the total propagation time along the Y delay line. Similarly, the X position can be detected by the X delay lines. As a result, the position of the detected particle can be encoded by the current arriving time difference at both ends of each parallel-pair delay-line [13–14]. And the Z position is determined by the arriving sequence.

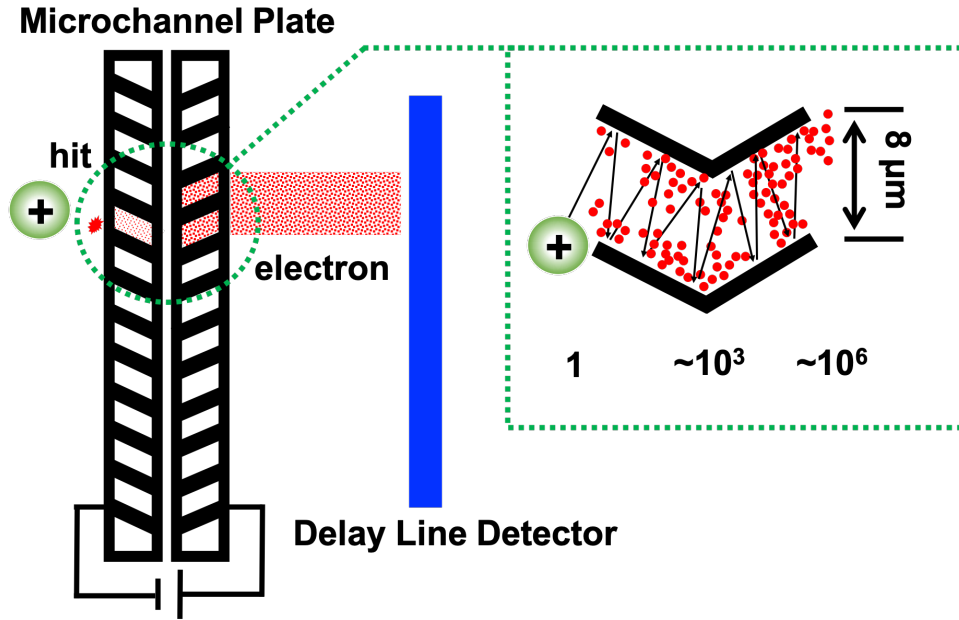


Figure 2.13 The operation principle of microchannel plate.

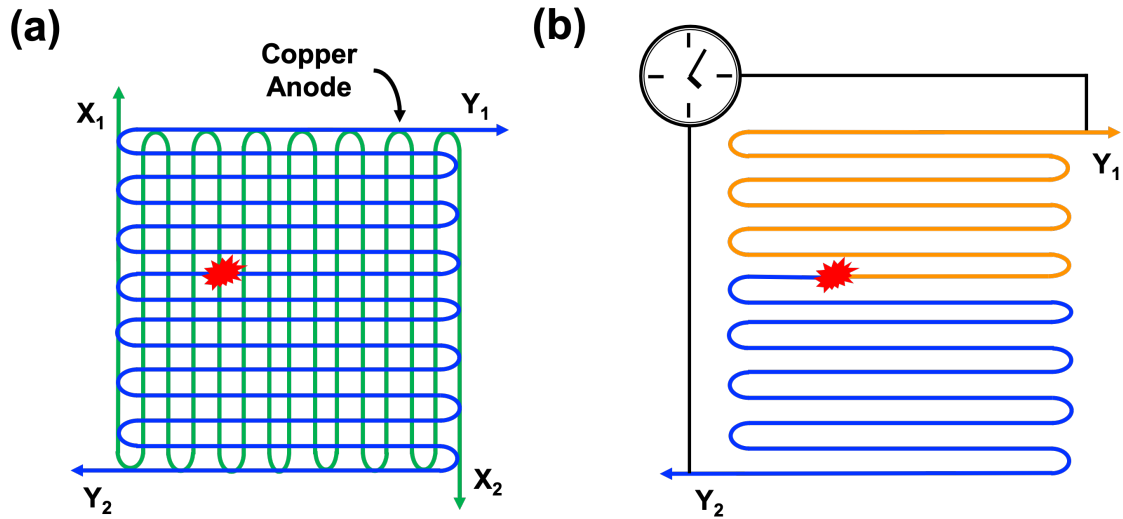


Figure 2.14 The operation principle of delay line detector. (a) The key component of DLD is two sets of parallel-pair delay-line (X and Y), (b) the time difference of the current arriving Y_1 end and Y_2 end is employed to encode the Y position.

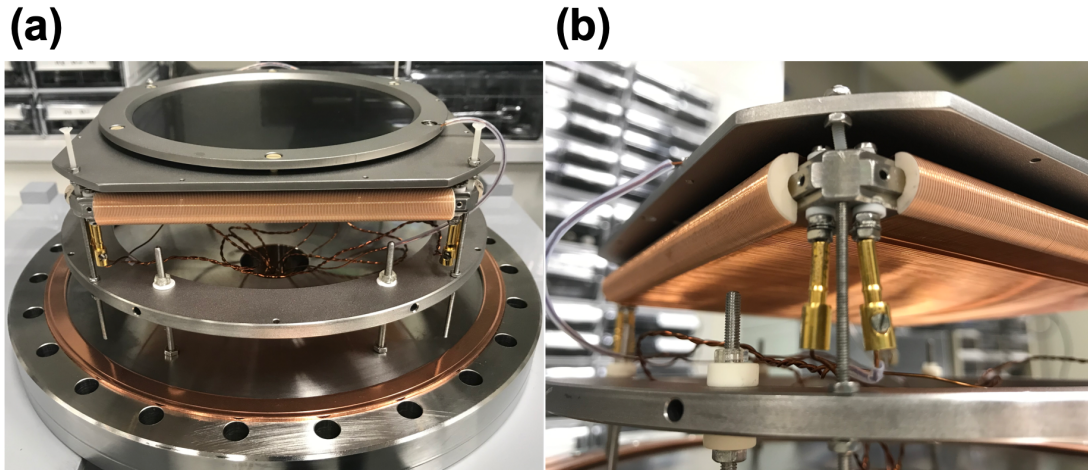


Figure 2.15 The images of PSD: The MCP and DLD are assembled together.

2.2.4. Laser Pulse System

The conditions of the laser pulse is shown in the table 2.1 The setup of the laser system is shown in figure 2.16. It is constituted by a Yb-doped fiber laser with a 3 W output power, 50 MHz repetition frequency, 1064 nm wavelength. After the laser pass through the pulse picker (AVESTA PROJECT Ltd. MODEL OG8-25), the laser with 5 kHz repetition frequency is generated. A photodiode (THORLABS DET10C) is used to pick up the exact moment of the pulsed laser shining on the specimen, which is regarded as the starting time of ToF. Then the laser pulse (532 nm) is generated by the second-harmonic generator. The linear polarization can also be rotated by means of a

half-wave plate. Then the laser pulse can be focused and introduced onto the specimen tip via a sapphire window. The size of the focused laser spot is approximately 10–20 μm . To align the laser spot on the specimen apex, a CCD camera is set with its optical axis as same course as that of the laser beam.

Table 2.1 The conditions of the laser pulse.

Wavelength	532 nm
Repetition frequency	5 KHz
Pulse width	300 fs
Pulse energy	2.5 nJ/pulse
Diameter of laser spot	10–20 μm

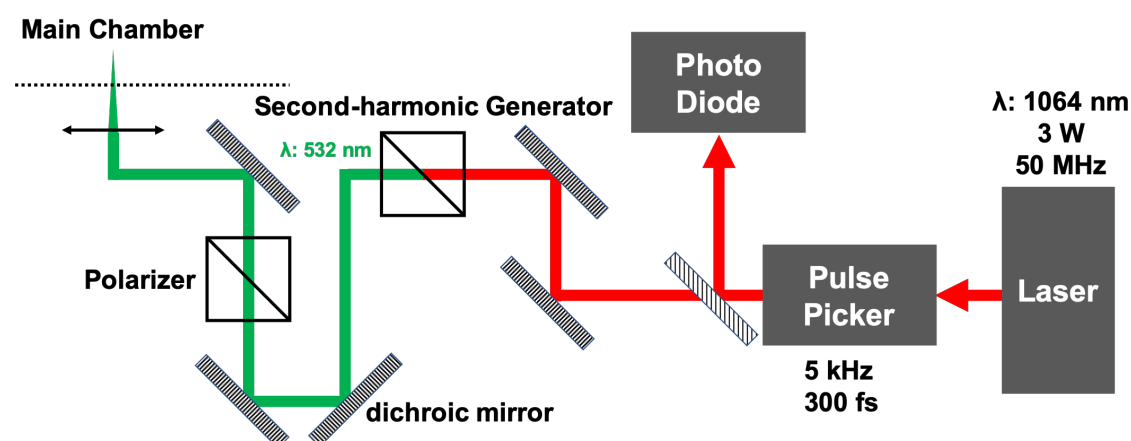


Figure 2.16 The setup of the laser system.

2.2.5 Voltage System

In FIM and AP measurements, a DC voltage is necessary to be applied on the specimen to generate a strong static electric ($\sim\text{V/nm}$) field. A high voltage power supply is equipped to provide a high voltage of up to 20 kV. The condition of the voltage pulse is shown in the table 2.2. The repetition frequency is usually set at 600 Hz in practice. The shape of a typical voltage pulse observed by oscilloscope is displayed in figure 2.17. The rise time of the pulse is about 3–5 ns, which is remarkably larger than that of laser pulse. In consequence, it may lead to an energy spread in mass-to-charge analysis.

Table 2.2 The conditions of voltage pulse.

Repetition frequency	< 1.5 KHz
Pulse width	10 ns
Pulse amplitude	< 3 kV
Rise time	< 5 ns

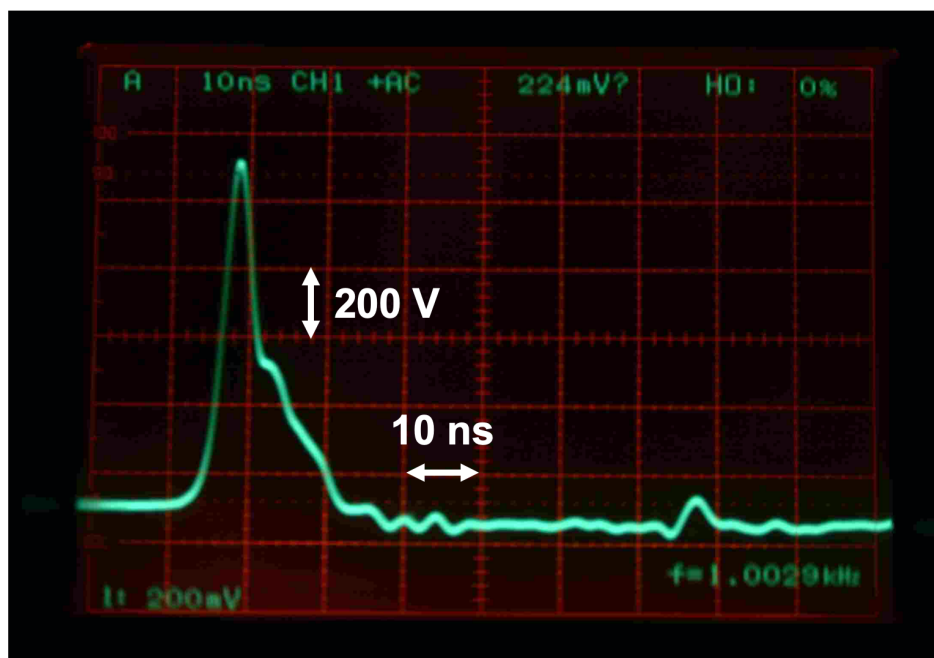


Figure 2.17 The voltage pulse observed by oscilloscope.

2.2.6 Gas Introduction System

Two kind of gases are used in this research: the imaging gases and reactant gases. The imaging gases include helium (He), argon (Ar) and neon (Ne). And the reactant gases comprise carbon monoxide (CO), hydrogen gas (H₂), deuterium gas (D₂), and oxygen gas (O₂). These gases can be introduced into main chamber by 2 sets of gas introduction systems. As shown in figure 2.18, Ne, Ar, D₂, He, and O₂ gas tubes are assembled in one system, while H₂ and CO gases can be introduced from the bottom of the main chamber. Two kinds of gases can be introduced into main chamber at the same time. The pressure (from 10⁻⁸ Pa to 10⁻⁵ Pa) of the gases can be controlled by variable leak valves. The rotary pumps in these two systems are used to degas the tubes when exchanging gases.

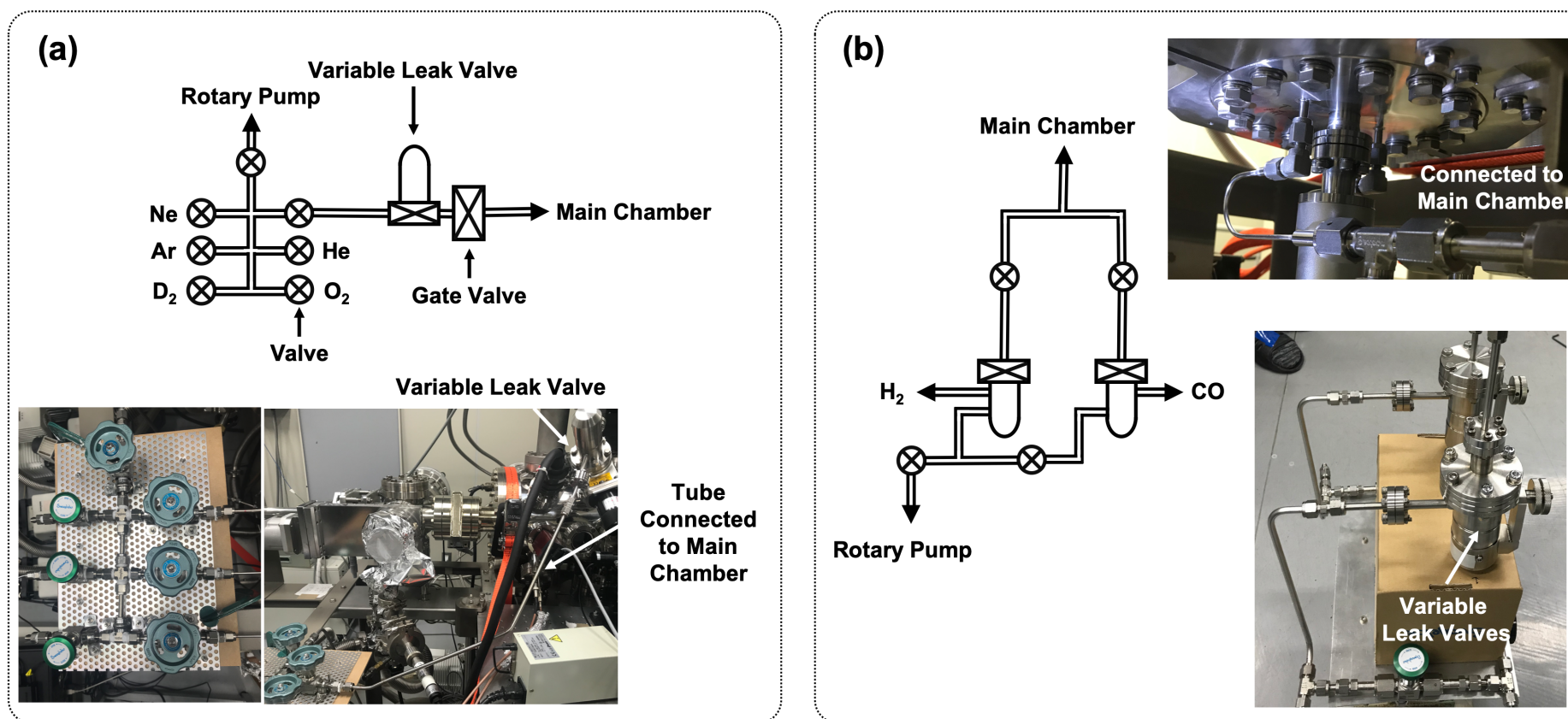


Figure 2.18 Two sets of gas introduction systems: (a) Ne, He, Ar, D₂, and O₂ can be introduced from upside; CO and H₂ can be introduced from the bottom of the main chamber.

2.2.7 Mass Spectrometer

The ToF mass spectrometer is used to determine the mass-to-charge ratio of the ions. Generally, the mass-to-charge is calculated by

$$\frac{m}{n} = \frac{2eVt^2}{L^2} \quad (2.2)$$

where m is the weight of the ion, n is the charge number of the ion, t is the ToF, e is the elementary charge, V is the total applied voltage L is the flight distance. When an ion hitting the point (x, y) on MCP, where the x and y are provided by PSD (figure 2.19), the ion trajectory can be approximately calculated as

$$L = \sqrt{L_o^2 + x^2 + y^2} \quad (2.3)$$

where L_o is the distance from sample apex to MCP centre.

In practice, the surface of the MCP is hardly normal to the axis of the sample (figure 2.19). The X and Y axes of MCP are tilted with angles α and β , respectively. Therefore, the flight path of the ion can be obtained by

$$L = \sqrt{(L_o + x\sin\alpha + y\sin\beta)^2 + x^2\cos^2\alpha + y^2\cos^2\beta}. \quad (2.4)$$

Therefore, the mass-to-charge ratio can be rewritten as [9]

$$\frac{m}{n} = \frac{2eVt^2}{(L_o + x\sin\alpha + y\sin\beta)^2 + x^2\cos^2\alpha + y^2\cos^2\beta}. \quad (2.5)$$

The ToF of the same ions with respect to X and Y axes are showed in figure 2.20. The raw data of the ToF in figure 2.20a and c show a clear slope along X and Y axes. After adjusting the α and β parameters, the ToF can be corrected (figure 2.20b and d).

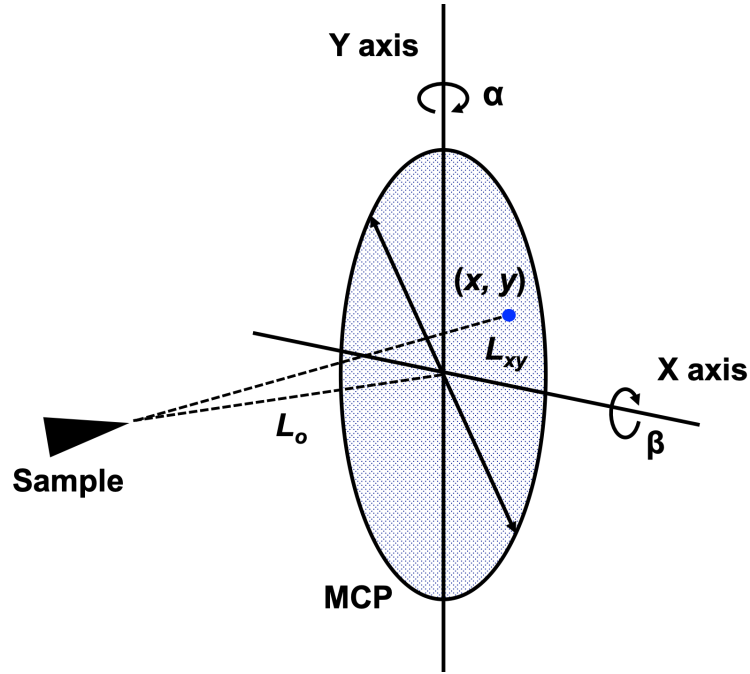


Figure 2.19 A Schematic diagram of the flight path of ions

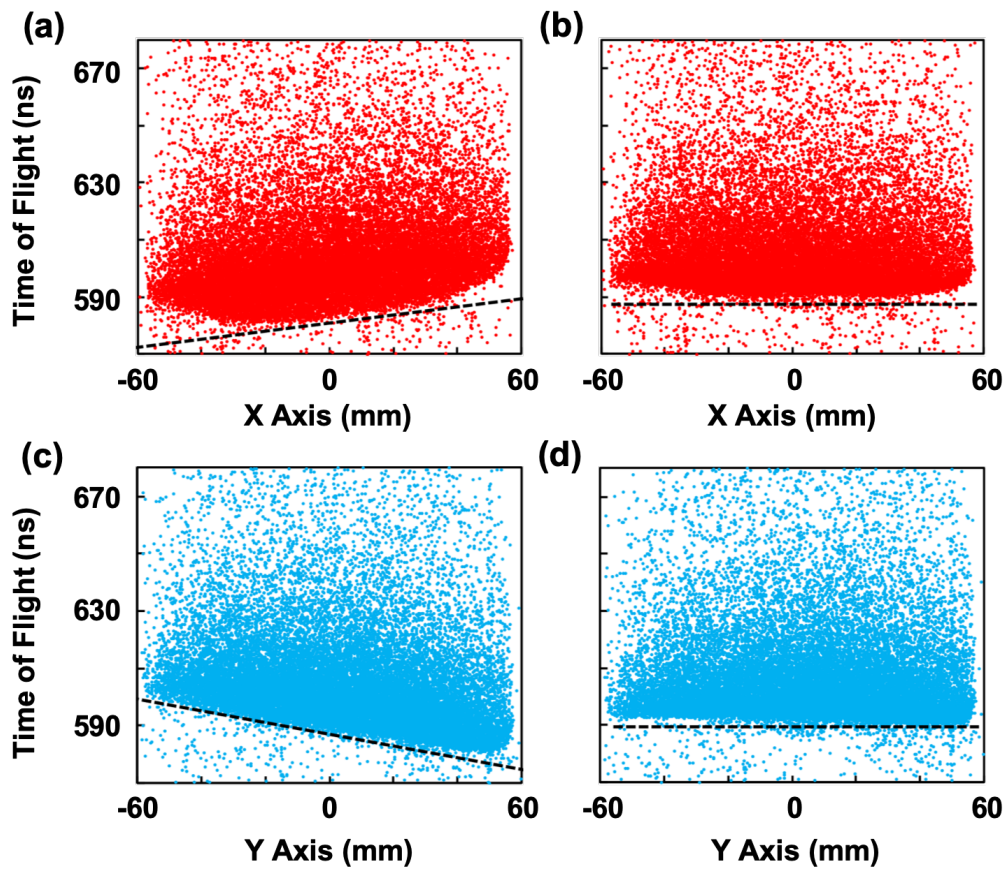


Figure 2.20 (a) The ToF of ions as a function of X axis without correction; (b) The ToF of ions as a function of X axis after correction; (a) The ToF of ions as a function of X axis without correction; (b) The ToF of ions as a function of X axis after correction.

2.4 Reference

1. T. F. Kelly and M. K. Miller, Atom probe tomography. *Rev. Sci. Instrum.* **78**, 031101 1–20 (2007).
2. B. Gault, M. P. Moody, J. M. Cairney and S. P. Ringer, Atom Probe Microscopy (Springer Science+Business Media, New York, 2012), Chapter 4.
3. A. J. Melmed, The art and science and other aspects of making sharp tips. *J. Vac. Sci. Technol. B*, **9**, 601–608 (1991).
4. M. K. Miller. *ATOM PROBE TOMOGRAPHY: Analysis at the Atomic Level* (Springer Science+Business Media, New York, 2012), Chapter 2.
5. K. Thompson, D. Lawrence, D. J. Larson, J. D. Olson, T. F. Kelly, B. Gorman, In situ site-specific specimen preparation for atom probe tomography. *Ultramicroscopy* **107**(2–3), 131–139 (2007).
6. J. Lindahl, T. Takanen and L. Montelius, Easy and reproducible method for making sharp tips of Pt/Ir. *J. Vac. Sci. Technol. B* **16**, 3077–3081 (1998).
7. N. Mayama, T. Iwata, C. Yamashita, S. Ito, T. Kaneko, S. Mikami, Y. Hanaoka, Y. Kajiwara, T. Kaito, T. Adachi, H. Hoshino, K. Nikawa M. Nojima, M. Taniguchi, M. Owari, Present State of development of laser-assisted wide angle three-dimensional atom probe. *Surf. Interface Anal.* **42**, 1616–1621 (2010).
8. Y. Hanaoka, N. Mayama, T. Terakawa, T. Yamamoto, Y. Kajiwara, T. Iwata, M. Taniguchi and M. Owari. Development of Laser-Assisted Wide Angle 3D Atom Probe. *J. Surf. Anal.* **17**, 237–240 (2011).
9. N. Mayama, Y. Kajiwara, S. Mikami, S. Ito, T. Kaneko, T. Iwata and M. Owari, Improvement of mass resolution in wide-angle laser-assisted atom probe by flight path compensation. *E-J. Surf. Sci. Nanotech.* **7**, 35–38 (2009).
10. T. Kaneko, S. Ito, C. Yamashita, N. Mayama, T. Iwata, M. Nojima, M. Taniguchi and M. Owari, Evaluation of the instrument for three-dimensional atom probe (3DAP). *Surf. Interface Anal.* **40**, 1688–1691 (2008).
11. M. Lampton, O. Siegmund and R. Raffanti, Delay line anodes for microchannel-plate spectrometers. *Rev. Sci. Instrum.* **58**, 2298–2305 (1987).
12. O. Jagutzki, V. Mergel, K. Ullmann-Pfleger, L. Spielberger, U. Spillmann, R. Dörner, H. S. Böcking, A broad-application microchannel-plate detector

- system for advanced particle or photon detection tasks: large area imaging, precise multi-hit timing information and high detection rate. *Nucl. Instrum. Meth. A* **477**, 244–249 (2002).
13. A. Oelsner, O. Schmidt, M. Schicketanz, M. Klais, and G. Schönhense, Microspectroscopy and imaging using a delay line detector in time-of-flight photoemission microscopy. *Rev. Sci. Instrum.* **72**, 3968–3974 (2001).
 14. G. Da Costa, F. Vurpillot, A. Bostel, M. Bouet, and B. Deconihouta, Design of a delay-line position-sensitive detector with improved performance. *Rev. Sci. Instrum.* **76**, 013304 1–8 (2005).
 15. O. Nishikawa, Y. Ohtani, K. Maeda, M. Watanabe, and K. Tanaka, Development of the Scanning Atom Probe and Atomic Level Analysis. *Mater. Charact.* **44**, 29–57 (2000).

CHAPTER 3 ELECTRIC FIELD DISTRIBUTION

To study the reaction by AP, the variation of chemical composition distribution of reactant, intermediate and product should be recorded to deduce the reaction process and identify the active sites. For example, the product is generated on AP sample surface as shown in Figure 3.1a. The generation speed varies on different planes on this nanosized specimen surface. The product molecules could desorb, be ionized in AP analysis to get a 2D mapping of the product. The detected ion intensity not only depends on the local molecules quantity but also the electric field (EF).

The ion intensity is proportional to the evaporation rate (ϕ), which obeys the Maxwell-Boltzmann law, which is expressed as [1]:

$$\phi \approx \nu \exp\left(\frac{-Q(F_o)}{k_B T}\right) \quad (3.1)$$

where ν is the vibrational frequency of a surface atom, k_B is the Boltzmann constant, T is the temperature, and $Q(F_o)$ is the field-dependent potential barrier. Two basic theories have developed to explain the field desorption, the image force model (image hump or Müller-Schottky model) and the charge exchange model (charge draining model) [2]. Though neither can be considered to be exactly accurate, it was illustrated that energy barrier is negatively correlated to the applied EF. Inspired by other researchers' works [3,4], we presume that the potential barrier is proportional to minus EF. EF is, therefore, one of the fundamental parameters for field desorption analysis. As shown in Figure 3.2b, When the static EF is below the threshold evaporation field (TEF), while the total EF, which represents the EF after applying a trigger pulse is above the TEF, synchronous ions can be detected. Evaporation will however not take place in case where the total EF is lower than TEF (Figure 3.2a). In contrast, a static EF value higher than that of the threshold will cause asynchronous ions (Figure 3.2c). Only the synchronous ions emitted from the sample under a proper EF thereby provide the exact mass-to-charge information obtained from time-of-flight (TOF).

In consequence, a proper static EF should be set to refrain from asynchronous ions. In addition, a nonuniform EF distribution all over specimen surface may result into a difference between real distribution on specimen surface and 2D mapping. Provided that the EF on a whole sample surface shows a gradient distribution, the highest EF stands on the apex of the sample, and the EF gradually decreases as the emitting area

getting away from the sample apex. As shown in Figure 3.1b, despite the product is denser on the orange area, the evaporation rate on red area could be higher due to its larger local EF. Therefore, the obtained 2D mapping of the product may not reflect the real distribution of the product on specimen surface (Figure 3.1c).

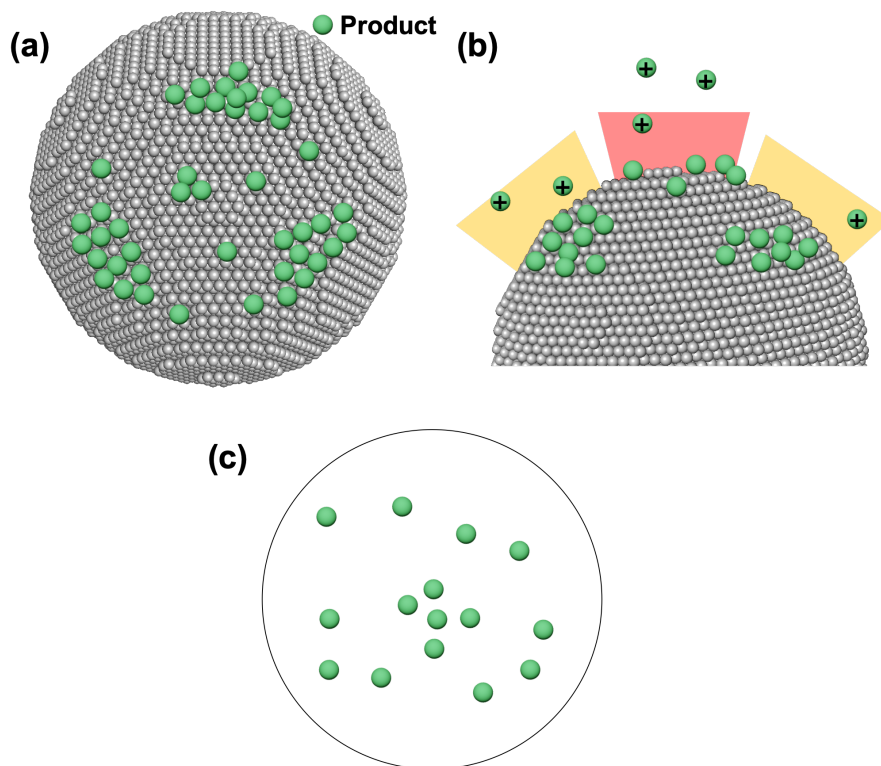


Figure 3.1 (a) The distribution of products on real specimen surface; (b) larger evaporation rate on red area (relative large EF) than that of orange area (relative small EF); (c) a possible 2D mapping of the product in AP analysis.

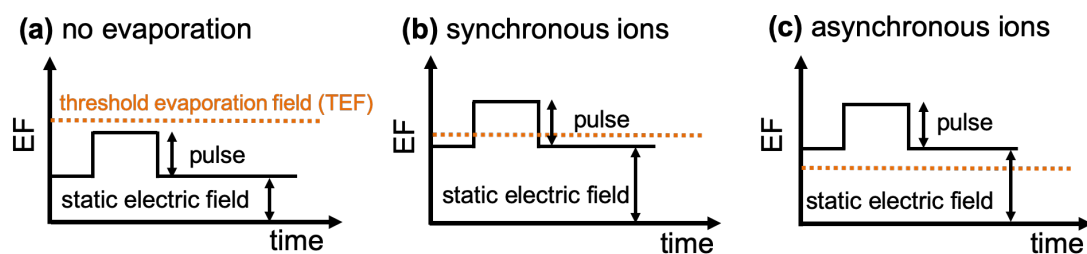


Figure 3.2 Schematic representation of the field evaporation conditions under different electric fields. (a) When the total EF, the sum of static EF and pulse EF is below the TEF, no evaporation takes place. (b) When the static EF is below the TEF while the total EF is above the TEF, ions synchronously evaporate. (c) When the static EF is above the TEF, ions asynchronously evaporate.

As a result, to accurately and quantitatively compare the active sites, it is crucial to calculate the EF distribution on the sample surface

In this chapter, the author presented a method to experimentally evaluate the EF distribution on a sample surface based on the evaporation rate of ions in AP analysis via a non-destructive way for the first time. Specifically, the apex of the Pt sample surface was determined through the comparison of the quantitative field ion microscopy (FIM) image on a three-fold symmetric surface. A series of contour maps of evaporated ions (e.g. H^+) were obtained upon applying various static EFs. Finally, a plot of relative EF with respect to the emitting angle was depicted.

3.1 Simulation

Before experiment, a simulation method was employed to evaluate the EF distribution on an ideally hemispheric specimen surface. The EF distribution on the sample surface was simulated by SIMION 8.1, a software package primarily used to calculate the electric fields and trajectories of charged particles in electromagnetic fields (Scientific Instrument Services).

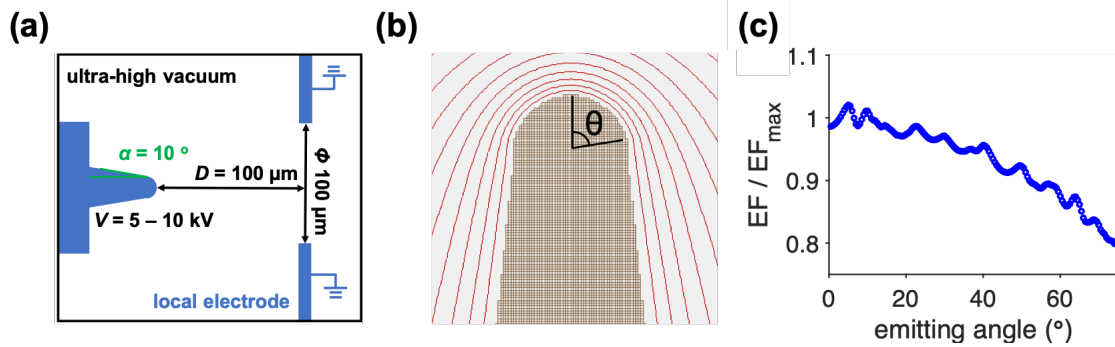


Figure 3.3 Simulation of the EF distribution on an ideal hemisphere. (a) A sample tip with the shank angle of 10° under a specific standing voltage. (b) The electric field distribution around a sample surface. θ indicates the emitting angle of the emitting ion trajectory and the sample axis. (c) The relative EF (EF/EF_{max}) with respect to θ . EF_{max} indicates the EF on the sample apex.

The simulation study consists of two steps, sample modelling and EF calculations. As illustrated in Figure 3.3a, an emitting electrode, composed of stacked and closely packed nanocubes (0.2 nm^3) representing the atoms, was regarded as an approximately ideal specimen shape. The local electrode with a hole ($\phi = 100 \mu\text{m}$) in the centre, positioned vertically to the tip axis with a distance of $100 \mu\text{m}$ away from the emitting

tip, acted as a grounded flat electrode. A positive voltage within a range of 5–10 kV was applied on the tip. The EF was computed by numerical solving of the Laplace equation ($\Delta V = 0$) using SIMION 8.1. Figure 3.3b clearly shows that the equipotential lines on the apex of the sample surface are much denser than that on the other positions, indicative of the highest EF residing on the apex. The calculated EF distribution over the sample surface steadily decreased as the emitting angle, θ representing the angle between the emitting ion trajectory and the sample axis increases from 0° to 80° (Figure 3.3c). Thus, the EF contour maps can be drawn as a series of concentric rings with the same central point, the sample apex on the sample surface. In addition, the observed tempestuous changes on the curve suggest the existence of abrupt alternation of EF, probably owing to the fine microstructures on the surface, such as terraces, steps, and kinks, where the EF dramatically raises on the protrusions and falls down in the valleys. A general trend for EF distribution of the sample surface was observed, despite the fluctuations of the EFs. As each sample inherently features a unique shape and specific surface curve, the simulation results of the EF distribution cannot accurately describe the EF distribution on a real sample surface.

3.2 Experimental Method

3.2.1 Determination of the Sample Apex on a Sample Surface

In order to identify the location of the sample apex to precisely map the EF contours. The FIM image of the Pt tip was obtained with helium gas (10^{-5} Pa) at 60 K (Figure 3. 4a). The radius of the hemispherical sample was estimated to be 28 nm by counting the number of steps between the (111) and $\{113\}$ planes. According to the FIM image, the sample apex was in the vicinity of the centre of the (111) plane, and the angle between the (111) and $\{113\}$ planes was determined to be 29.5° . For the sake of simplicity, we assumed that the EF decreases proportionally from (111) plane to $\{113\}$ planes. The ion intensities of the FIM image were subsequently laid on a coordinate system (Figure 3. 4b). The weight factors of the (311), (131), and (113) planes were calculated to be 1, 1.33, and 1.29, respectively, which are the relative ion intensity normalized by the ion intensity on (311) plane. As a result, the coordinate of the sample apex was determined to be $(-7.7 \text{ nm}, -14.3 \text{ nm})$, shown in Figure 3. 4c. It is worthy to mention that the sample axis was not perpendicular to the detector surface.

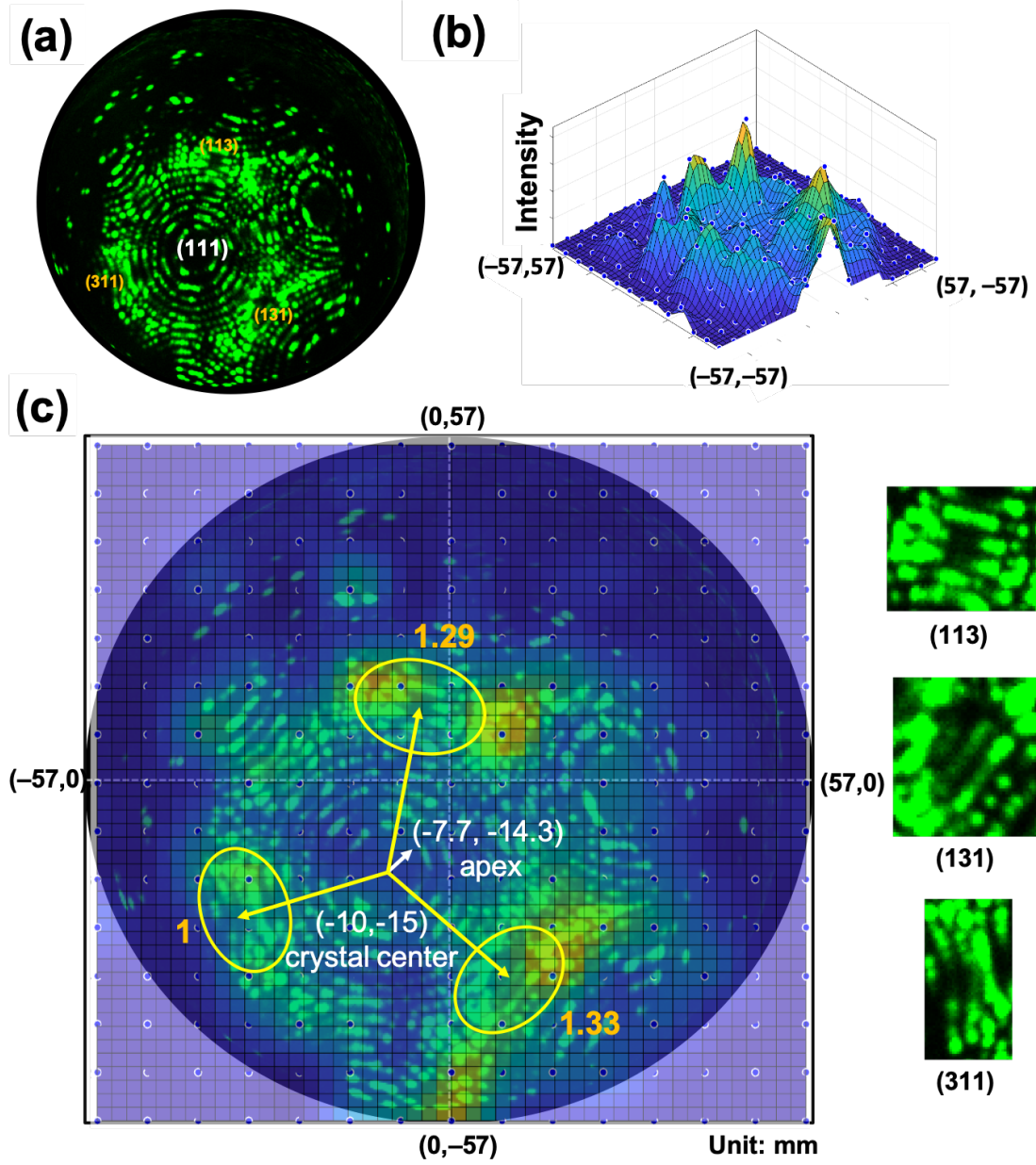


Figure 3. 4 (a) A field ion micrograph (FIM) of the Pt surface imaged in helium gas (10⁻⁵ Pa) at 60 K. (b) The intensity of the FIM ions on the sample surface. (c) Location of the sample apex. The FIM image laid on a coordinate system. The weight factors of (311), (131), and (113) planes are 1, 1.33 and 1.29, respectively, where the weight factor is the relative ion intensity normalized by the ion intensity on (311) plane. The coordinate of the sample apex is (-7.7 mm, -14.3 mm). (113) plane center is (-4.0 mm, 13.5mm). (311) plane center is (-34.2 mm, -24.2mm). (131) plane center is (8.5 mm, -34.0 mm). Sample apex = $1.29/(1 + 1.33 + 1.29) \times (-4 \text{ mm}, -13.5 \text{ mm}) + 1/(1 + 1.33 + 1.29) \times (-34.2 \text{ mm}, -24.2 \text{ mm}) + 1.33/(1 + 1.33 + 1.29) \times (8.5 \text{ mm}, -34.0 \text{ mm})$. The angular displacement between the centre and the corner edge of the detection area is 1 rad (57.3°), corresponding to 57 mm in the coordinate used here.

3.2.2 Ion Intensity Contour Maps on a Sample Surface

In this report, H^+ ions were utilized as the probe ions, which were generated from the residual hydrogen (H) remaining in the chamber under an ultra-high vacuum (8.0×10^{-8} Pa). The relative ion intensity can be calculated according to the following equation:

$$\text{relative ion intensity} = \frac{(\text{probe ions counts in a specific area})}{(\text{relative emitting area}) \times (\text{detection time})} \quad (3.2)$$

The projected area was divided into a series of concentric rings with a same central point, the apex of the Pt sample (Figure 3.5a). The areas of the projected rings were rectified to estimate the relative emitting areas on the spherical surface by trigonometric functions (Figure 3.5b).

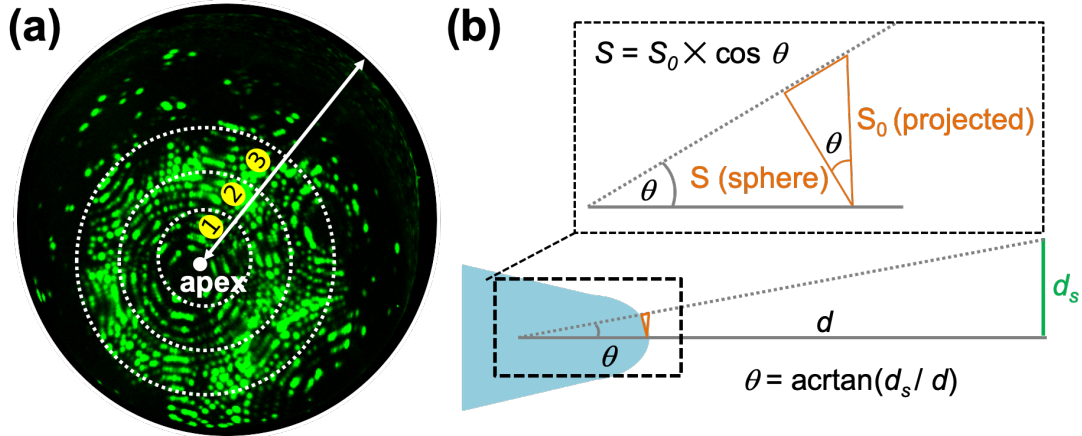


Figure 3.5 A FIM image separated into a series of concentric rings, whose centre are the apex. The concentric rings are numbered from inside to outside. (b) Schematic presentation of the relative emitting area (S) was calculated according to the trigonometric functions. θ indicates the angle between the emitted ion trajectory and the sample axis. d indicates the flying distance from the sample to TPSD and d_s indicates the distance from the centre of TPSD to the edge of the projected area.

Utilizing the approach described above, we prepared the contour maps of the **relative** H^+ intensity on the Pt sample surface (Figure 3.6). In the calculation, the detected surface was divided into 10 concentric rings. When the applied EF was low, such as 21.5 V nm^{-1} , and 23.7 V nm^{-1} , the H^+ ion on the **sample apex** was solely detected. Upon increasing EF, **the H^+ ionization area** gradually extended to the **other** concentric rings, and the **relative** H^+ intensity on the apex increased as shown by the colour change from blue to yellow.

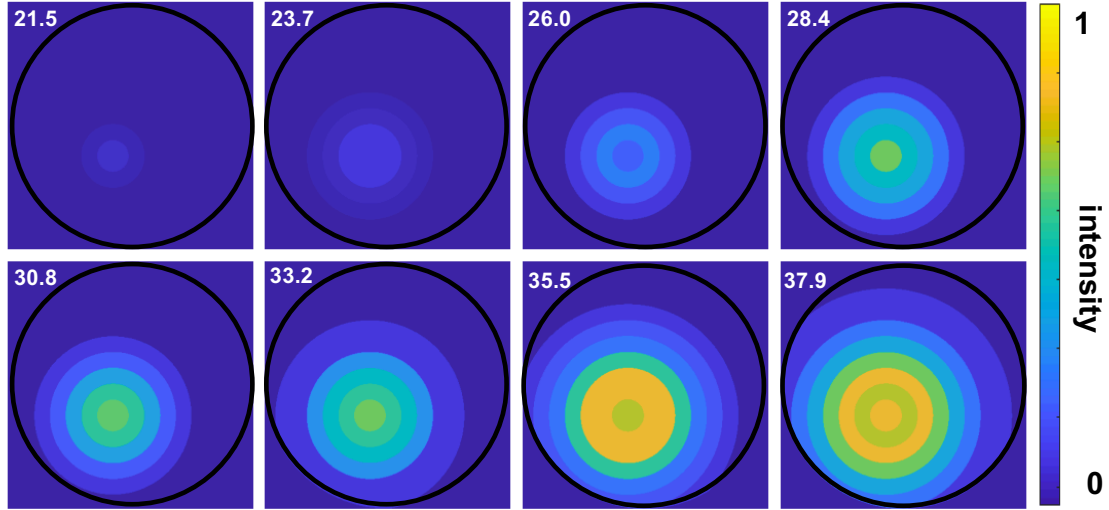


Figure 3.6 The contour maps of the normalized H^+ intensity, I on the Pt sample surface under various EFs. The EF values on the sample apex are shown in the upper left corner of each contour map with a unit of $V\ nm^{-1}$. The colour bar on the right of the figure indicates the normalized H^+ intensity.

The maximum evaporation rate of H^+ ion was 17 counts/s. With regard to the source of H, they can be traced in terms of (1) the H stored in Pt, (2) the residual H_2 gas in the chamber under ultra-high vacuum, (3) the H or H_2 diffused from the sample shank to the sample apex. Considering the fact that the pure Pt is a poor H storage material [5], H supplied from Pt bulk can be neglected. As H_2 is the predominant gas at ultra-high vacuum, hit frequency of H_2 to the sample surface can provide the insights into the source of H. Hit frequency can be calculated using the Langmuir Equation:

$$hit\ frequency = N/A\tau = P/(2\pi mk_B T)^{1/2} \quad (3.3)$$

where N is the number of molecules, A is the hit area, τ is the time, P is the pressure, m is molecular mass, k_B is the Boltzmann constant, and T is the temperature. The hit frequency of H_2 at 8×10^{-8} Pa and 273 K was estimated to be $0.026\ nm^{-2}\ s^{-1}$. Accordingly, about 32 molecules of H_2 will hit on the sample surface, a hemisphere with a diameter of 28 nm, per second, which is larger than the maximum evaporation rate determined experimentally, indicating that the H_2 remaining in the chamber can supply sufficient amount of H source for evaporation. Additionally, the H_2 gas polarized by a ultra-high EF will be adsorbed on the Pt surface under cryogenic temperature due to the thermal accommodation process [1], giving rise to an accumulation of H_2 gas on the sample surface, though appropriate model has not been established to estimate the gas concentration on the sample surface [6]. Moreover, H_2

quickly dissociates to H on the Pt surface and the dissociated H atoms would be adsorbed on the Pt surface [7]. Based on the discussion above, we concluded that H₂ gas on sample surface is enough for AP analysis and H ionization is a field desorption process on Pt surface.

3.2.3. EF Distribution Calculation

After preparing the contour maps (Figure 3.6) of the relative H⁺ intensity, we are able to calculate the EF distribution on the Pt sample surface. The relative intensity, I_n/I_1 can be simply calculated by comparing the normalized intensities of H⁺ on ring n and ring 1. The EF distribution is expressed by modifying Eq. 3.1

$$I_n/I_1 = \exp\left(\frac{-Q_n+Q_1}{k_B T}\right) = \exp(A \times EF_1(f(n) - 1)) \quad (3.4)$$

where Q_n and Q_1 represent the energy barriers for ring n and ring 1, respectively. A is the constant. EF_1 is the EF on the sample apex. $f(n)$ is a function describing the relationship between the relative EF (EF_n/EF_1) with respect to ring number, n . The fitting code was given in appendix F. The change of the mean value of H⁺ intensity against ring number was plotted in Figure 3.7a. The function $f(n)$ was resolved by fitting Eq. 3.4 using least squares method

$$f(n) = 1 - 0.005(n - 0.5)^2 \quad (3.5)$$

A linear relationship between θ , the emitting angle between the emitting ion trajectory and the sample axis and ring number, n was obtained (Figure 3.7a inset). Next, the relationship between the relative EF and emitting angle θ was determined (Figure 3.7b). The error bars (up side and down side) of the relative EF on each ring number n were calculated as follows:

$$error_up = (\ln(\overline{I_n/I_1} + e_n) / (A \times EF_1) + 1) - f(n) \quad (3.6)$$

$$error_down = f(n) - (\ln(\overline{I_n/I_1} - e_n) / (A \times EF_1) + 1) \quad (3.7)$$

where e_n represents the error of H⁺ intensity on ring n in figure 6a. The curve of relative EF obtained experimentally is in accordance with the simulation curve (Figure 3.3c) that the relative EF gradually decreases with the increasing of the emitting angle on the sample surface. The variation of EF is small as the emitting angle is less than 30°. When the emitting angle is larger than 30°, the rate of change becomes faster, probably due to the larger curvature close to the edge of hemispherical surface. Additionally, the error

bars at the emitting angle ranging from 30° to 50° is much larger than that on the other emitting angles. This can be ascribed to the accumulation of fine microstructures on this region.

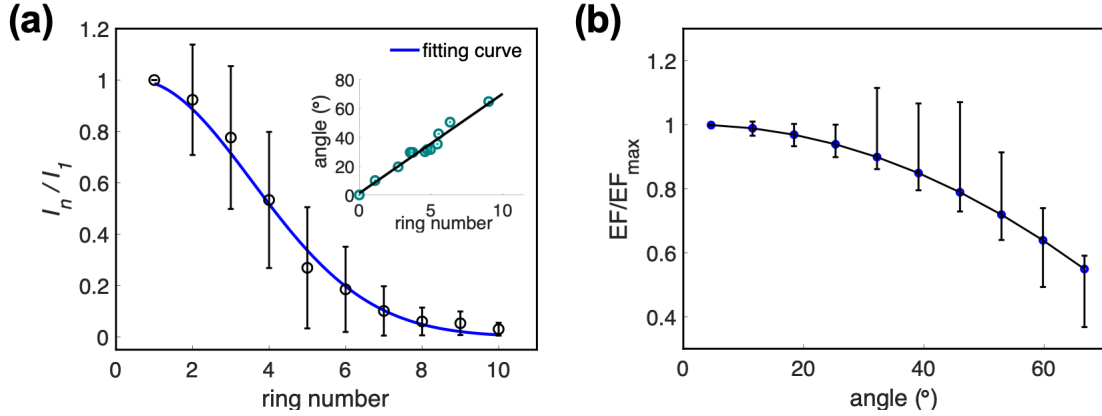


Figure 3.7 (a) The change in the relative intensity I_n/I_1 (intensity of n ring number/Intensity of its 1st ring number) with respect to ring number. The curve is fitted by Eq. 3.4. (Insert) The correlation of θ against ring number. (b) The change in the relative EF with respect to θ .

3.3 Specimen Shape Effect

The EF distribution varies on every AP specimen of specific shape.

As for a fresh sample, just made by FIB milling, the shape close to a dome as shown in Figure 3.8. The EF distribution on this fresh sample has been calculated in **section 3.2** Figure 3.7b, where the EF decreased dramatically as the emitting angle increased.

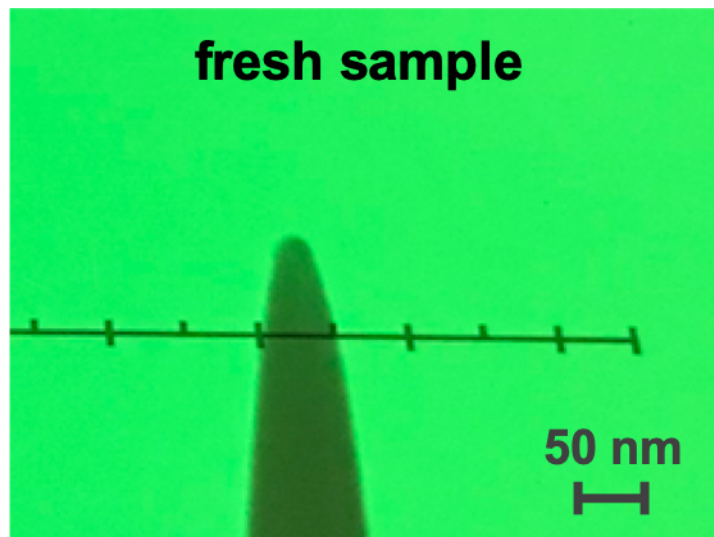


Figure 3.8 A TEM image of the sample surface for the fresh sample.

In AP analysis, field evaporation occurs selectively at sharpest places, where the EF is relatively higher. On a fresh emitter surface, the atoms originally from specimen surface on the apex area would preferentially evaporate. Besides, any small irregularities remaining on the surface could be removed to create a smooth atomically clean surface. After sufficient field evaporation, almost all the emitters will develop into a dynamic field evaporation end-form, as shown in Figure 3.9.

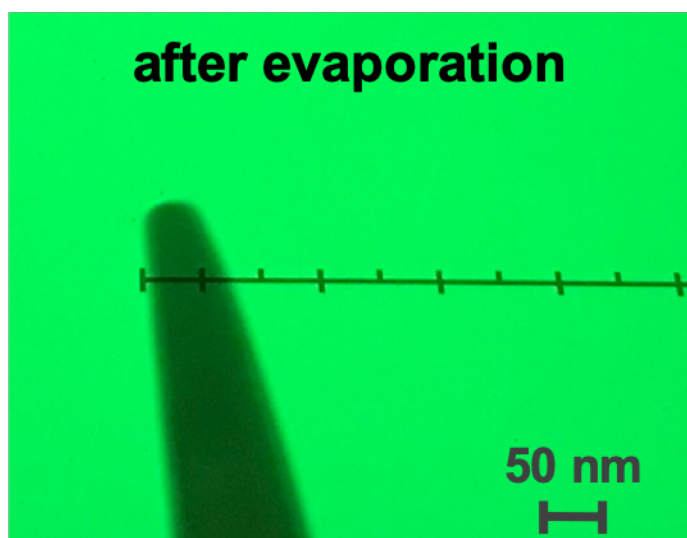


Figure 3.9 A TEM image of the sample surface for the fully evaporated sample.

The EF distribution on the sample after evaporation was further determined by the method described above (Figure 3.10). The relative EF almost kept constant in an angle region of 0° to 50° , which suggests that the sufficiently evaporated shape makes the field evaporation rate-constant almost the same everywhere across the evaporating area, except the outer boundary.

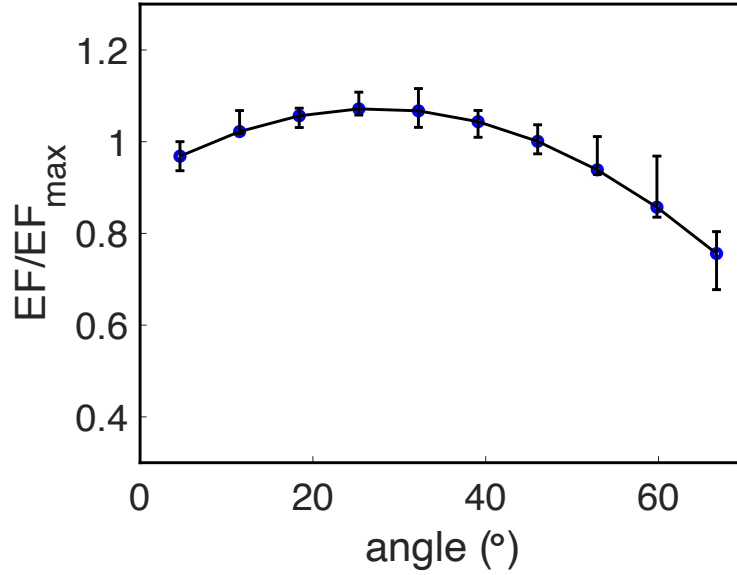


Figure 3.10 The relative EF on a sufficient evaporated emitter with respect to θ . The plot of the relative EF with respect to θ . $f(n) = 1.07 - 0.0097(n - 3.778)^2$. The original data are listed in appendix G.

3.4 Conclusion

Conclusively, the author developed an approach to experimentally calculate the EF distribution on a nano-sized sample surface by comparing the normalized ion intensity in AP analysis. To determine the EF distribution on a real sample surface, first the author located the sample apex of the sample surface by comparing the ion intensity of the FIM image. Next, the contour maps with various EF_{\max} showing the intensity of the H^+ was obtained. Finally, a plot of relative EF with respect to the emitting angle can be extracted from the contour maps. The fact that the evaporation EF for H^+ is lower than that of Pt atoms suggests that our analysis approach is non-destructive. This fast and non-destructive method could be employed to determine the appropriate EF for accurate AP analysis.

In addition, the specimen emitter will evolve to be an EF-constant surface except the outer boundary, after sufficient field evaporation where the emitter develops into an equilibrium end shape. As a result, the ion intensity of the 2D mapping of such surface can exactly reflect the real distribution of the chemical composition on the emitter.

3.5 Reference

1. Baptiste Gault, Micheal P. Moody, Julie M. Cairney, Simon P. Ringer, *Atom probe Microscopy*. (Springer Science + Business Media, New York, 2012), Chapter 2.
2. M. K. Miller. *ATOM PROBE TOMOGRAPHY: Analysis ay the Atomic Level* (Springer Science+Business Media, New York, New York, 2000), Chapter 2.
3. E. A. Marquis and B. Gault. Determination of the tip temperature in laser assisted atom-probe tomography using charge state distributions. *J. Appl. Phys.* **104**, 084914(1–8) (2008).
4. M. K. Miller, R. J. Forbes. *Atom Probe Tomography: The Local Electrode Atom Probe*. (Springer, New York, 2014), Chapter 2.
5. H. D. Beckey. *Principles of Field Ionization and Field Desorption Mass Spectrometry*. (Elsevier Ltd.; 1977), Chapter 1.
6. Z. M. Stepien, T.T. Tsong, Formation of metal hydride ions in low-temperature field evaporation. *Surf. Sci.* **409**, 57-68 (1998).
7. N. B. Arboreta. Jr., H. Kasai, W. A. Diño, H. Nakanishi, Potential energy of H₂ dissociation and adsorption on Pt(111) Surface: First-Principles Calculation. *Jpn. J. Appl. Phys.* **46**, 4233–4237, (2007).

CHAPTER 4 QUANTITATIVE ANALYSIS OF RESIDUAL HYDROGEN

For the first time to *in-situ* observe the reaction process by AP, the author prefers a simple reaction, hydrogen oxidation reaction catalyzed by Pt metal, as a tentative model in this research. In this reaction, two kinds of gases (H_2 and O_2) are expected to be introduced into the main chamber. However, the residual hydrogen signals (H^+ and H_2^+) could be always detected on Pt surface even without introducing any H_2 gas into the main chamber. As a main residual gas in ultra-high vacuum, the behaviors of hydrogen (H) on Pt surface should be explored before conducting a hydrogen oxidation reaction on Pt surface.

In addition, studies of hydrogen content on/in metal deserve more attentions. For one thing, hydrogen-related materials hydrogen embrittlement and corrosion are fundamental problems of material. For another, quantitative analysis of the hydrogen remain a great challenge due to tiny size, small mass to charge ratio and near-ubiquitous character of hydrogen element. Several methods have been developed to study the relationship between hydrogen and metal. Thermal desorption spectroscopy can provide the adsorption and desorption information about hydrogen gas [1]. Secondary ion mass spectrometry can directly image hydrogen but cannot identify the precise location of hydrogen atom [2]. TEM can only be used in specific case, because of its projection and diffraction effects [3]. Atom Probe (AP) is another potential candidate, which is capable of resolving individual atom and identifying chemical position with near-atomic resolution.

Several pioneer works have been made to detect H in AP analysis. Seidman found that Nb had a high solubility for hydrogen, which can be stored as deep as whole detection range [4]. Advances have been made using $^2_1H(D)$ charging method as a substitute for 1_1H in AP analysis [5–7]. However, the residual H remaining in AP ultra-high vacuum chamber limited the ability to quantify H concentration in metal. The hydrogen gas (H_2) remaining in ultra-high vacuum chamber could accumulate on the AP sample surface through a thermal accommodation process by virtue of high electric field. In consequence, a significant amount of H_2^+ may cause an unwanted overlap with D^+ in mass spectrum. Furthermore, the adsorbed residual gas also promotes the

formation of metal hydride complex ions, further complicating hydrogen detection [8,9]. Hence, improved insight and understanding into the effect of experimental parameters on the behavior of residual H₂ gas on specimen tip surface is necessary for more accurate analysis of the H content in metal and alloy.

Several authors have investigated the relationship between residual H signals and experimental parameters in AP analysis. Prakash Kolli has systemically studied the laser pulse energy, laser pulse frequency and tip base temperature effects on residual hydrogen detection, and suggested that the total quantity of residual H₂ gas can be changed in mass spectra by varying the laser pulse energy and pulse frequency [8]. Sundell holds the opinion that high DC voltage can remove the H₂⁺ from the spectrum [10]. It is considered that the electric field has a significant effect on residual H signals in the aforementioned studies [10, 11]. Nevertheless, no systematic investigation has been performed to define the relationship between electric field and residual H signals. Additionally, the occurrence of the H₃⁺ signal still remains unsolved.

This research would systematically study electric field effects on residual H signals by AP in laser pulse mode. Platinum (Pt) metal was utilized in this study because it has a high evaporation field, and was reported to be hard to form hydrides in AP analysis. A comparison between residual H signals and deuterium gas (D₂) signals was also performed to ascertain the source of the residual H. We also discussed the formation of all residual H signals.

4.1 Residual Hydrogen in AP analysis

The residual hydrogen in the chamber in ultra-high vacuum condition (10⁻⁸ Pa) and low temperature (60 K) was measured by AP. Figure 4.1a shows a typical mass spectra of H species on the Pt surface under various electric fields. In the MS spectra, three signals with the mass-to-charge state (*m/n*) ratio of 1 Da, 2 Da and 3 Da were observed, which are assignable to H⁺, H₂⁺ and H₃⁺, respectively. Upon increasing electric field, the relative intensity of H⁺ dramatically increased, while the relative ratio of H₂⁺ ions decrease, as shown in Figure 4.2a. On the other hand, the ratio of H₃⁺ was not strongly affected by electric field.

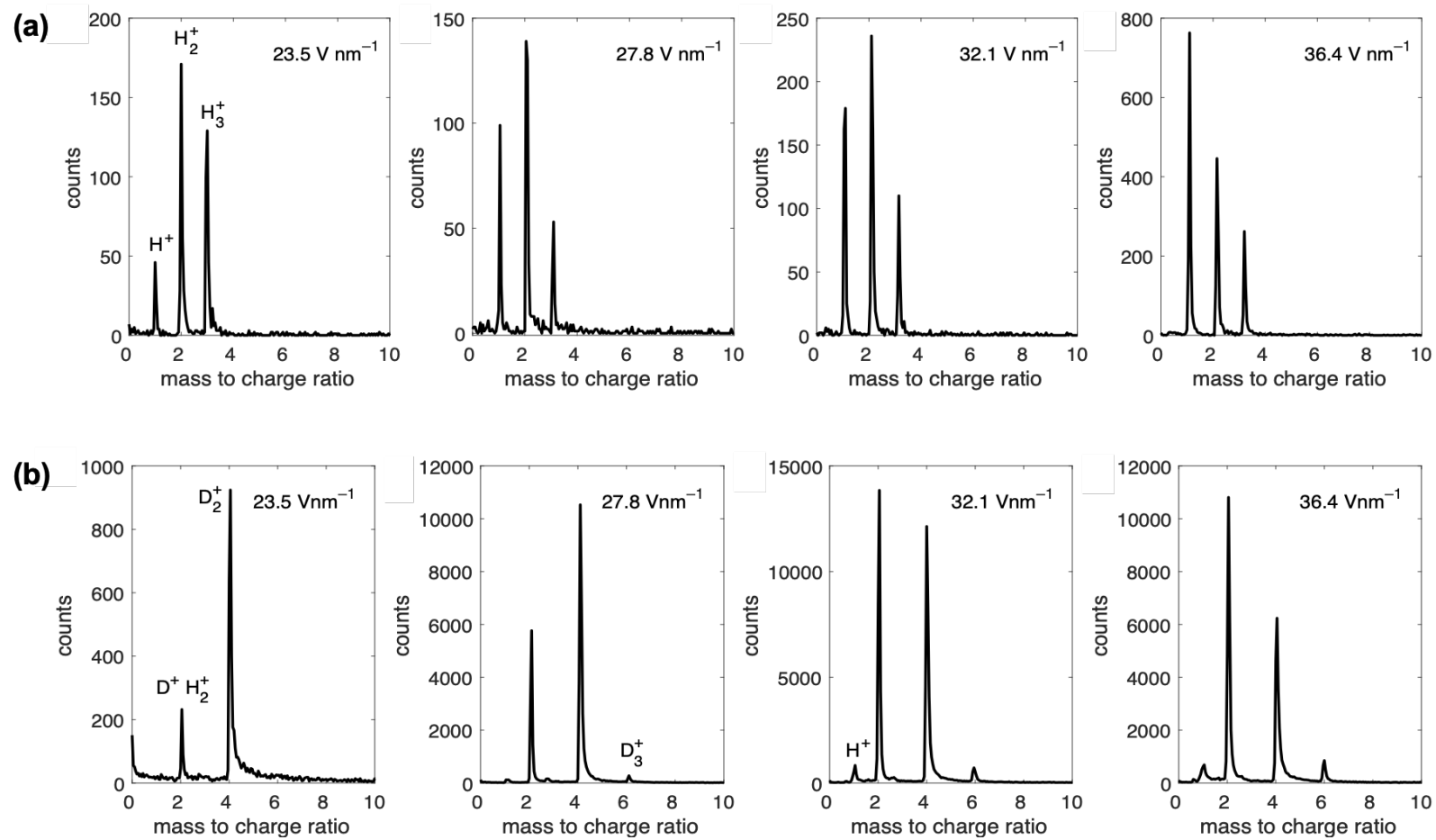


Figure 4.1 (a) Mass Spectra of the residual H on Pt surface under different electric field in AP measurements (60 K). The background pressure was 10^{-8} Pa. (b) Mass Spectra of D₂ gas on Pt surface under different electric field (60 K). The pressure of D₂ gas was 2.0×10^{-6} Pa.

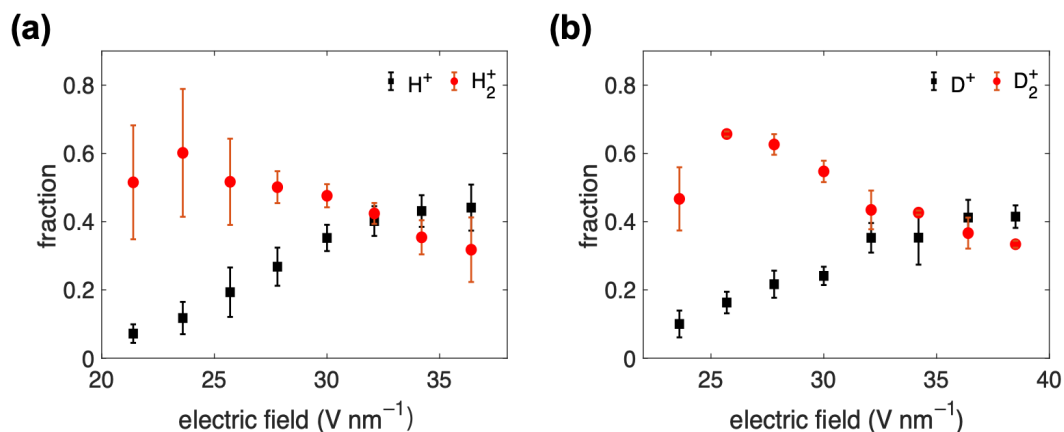


Figure 4.2 A plot of (a) hydrogen (Pt, 60 K, background pressure: 10^{-8} Pa) signal fractions and (b) deuterium (Pt, 60 K, D_2 pressure: 2.0×10^{-6} Pa) signal fractions with respect to electric field from 21.4 V nm^{-1} to 40 V nm^{-1} . Black spots indicate the ratio of H^+/D^+ against total ions counts. Red spots indicate the ratio of H_2^+/D_2^+ against total ions counts.

In order to evaluate the correlation of the signal intensity of H^+ and H_2^+ with respect to electric field, the contour maps showing the normalized intensity of H^+ and H_2^+ under various electric field were prepared (Figure 4.3 and Figure 4.4). The contour maps of Figure 4.3 presents the distribution of ions on a real sample under certain electric field during AP analysis. In each contour map, the surface is divided into 10 rings and the distribution of relative signal intensities of ions (H^+ and H_2^+) from low to high are indicated by the colour change from blue to yellow. The highest electric field stands on the 1st ring, suggesting the apex of the Pt sample. The electric field of the apex area was indicated on the upper left corner of each contour map. The relative values of the electric field (EF/EF_{apex}) on these 10 concentric rings were calculated based on our previous work [12] (Figure 4.4).

Upon increasing the electric field from 21.5 V nm^{-1} to 28.4 V nm^{-1} , the contour maps of H_2^+ showed a clear gradient that the H_2^+ intensity increased from the outside to central rings. It is noted that substantial amount of H_2^+ was detectable even under a low electric field of 21.5 V nm^{-1} . Continuous increase of the electric field, nevertheless, led to a decrease of H_2^+ intensity on the apex but an increase on the edge of the sample surface. In contrast, few H^+ was detected under 21.5 V nm^{-1} . The intensity of H^+ exhibited a monotonic increase on Pt surface and the highest intensity constantly resides on the apex, as the electric field increased from 21.5 V nm^{-1} to 37.9 V nm^{-1} . These

results indicate that higher electric field is requisite to generate H^+ than that for H_2^+ , which is in accordance with previous reports by Sundell and Kellogg [10, 11].

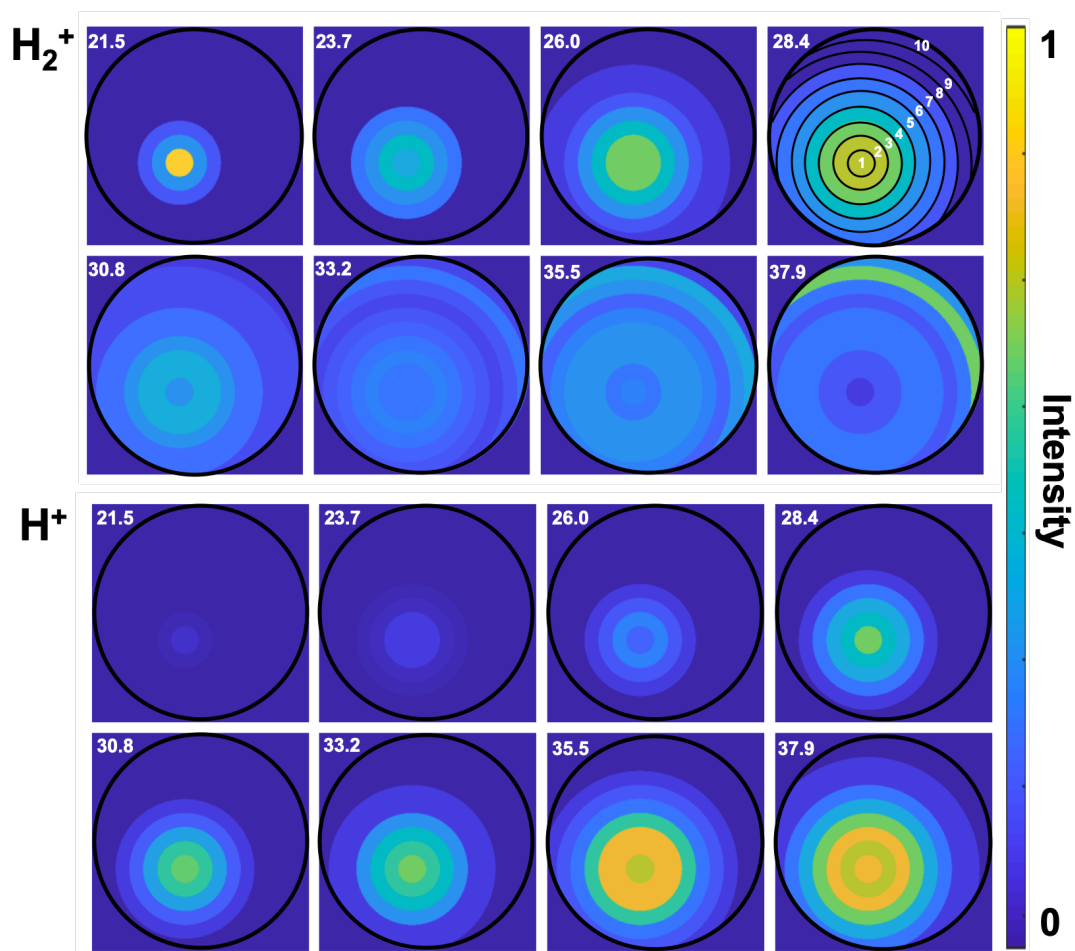


Figure 4.3 Contour maps of normalized (a) H_2^+ intensity, and (b) H^+ intensity on Pt sample surface under various electric fields. The electric field values on the sample apex are shown in the upper left corner of each contour map with a unit of V nm^{-1} . The colour bar indicates the normalized ion intensity.

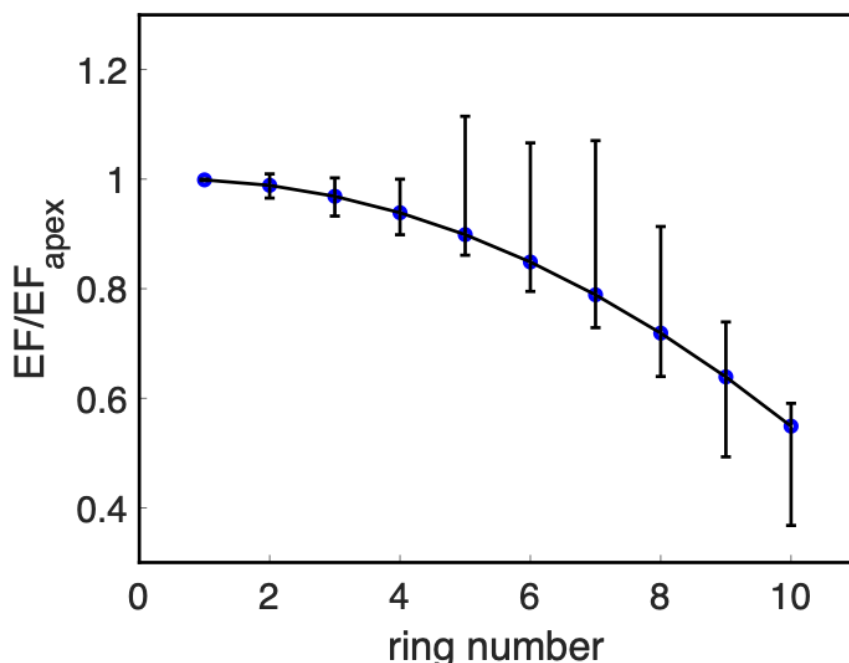


Figure 4.4 A plot of relative electric field (EF/EF_{apex}) with respect to ring number.

4.2 Source of Residual Hydrogen

With regard to the source of residual hydrogen observed by AP analysis, we speculated that there are two candidates: (1) the adsorbed H_2 molecules on the Pt surface; (2) the hydrogen atom/molecule embedded in the Pt metal. To seek the origin of residual hydrogen, we designed an AP measurement by introducing additional D_2 gas prior to 2.0×10^{-8} Pa (Figure 4.1b). The pressure increased to 2.0×10^{-6} Pa after introducing D_2 gas. Upon applying electric field on the Pt surface, several signals with the values of 1 Da, 2 Da, 4 Da and 6 Da were observed. While the signals of 1 Da, 4 Da and 6 Da can be clearly assigned to H^+ , D_2^+ and D_3^+ , respectively, the 2 Da signals would be the overlap of H_2^+ and D^+ . Considering the fact that the D_2 gas pressure was far larger than the base pressure (2.0×10^{-8} Pa), which is mainly caused by the residual H_2 gas, the majority component of the 2 Da signals is composed of D^+ ions. Additionally, it has been found that the intensity of H_2^+ is comparable to that of H^+ after applying an electric field as confirmed by Figure 4.1a, so the significantly small peak derived from H^+ infers a negligible small amount of H_2^+ , which would contribute to the 2 Da signal. Therefore, the signals of 2 Da and 4 Da can be used to discuss the variation of the D^+ and D_2^+ ions as a function of electric field. As shown in Figure 4.2b, with an increase of electric field, the signal intensity of D^+ increases while that of D_2^+ decreases,

which is consistent with the H^+ and H_2^+ fraction alterations measured under base pressure (2.0×10^{-8} Pa).

Next, the D_2 pressure was reduced to 6.0×10^{-8} Pa, where three signals of 1 Da, 2 Da, and 4 Da with comparable intensity were observed in mass spectrum, suggesting the coexistence of hydrogen and deuterium on Pt surface (Figure 4.5a) so that the 2 Da signal is composed of both H_2^+ and D^+ ions. To clarify the ratio of these two ions, the intensity of H_2^+ ions and D^+ ions could be calculated as follow,

$$I_{H_2^+} = I_{H^+} \times (H_2^+/H^+) \quad (4.1)$$

$$I_{D^+} = I_{2D} - I_{H_2^+} \quad (4.2)$$

where $I_{H_2^+}$ is the intensity of H_2^+ ions, I_{H^+} is the intensity of H^+ , H_2^+/H^+ is the ratio of H_2^+ intensity to H^+ intensity, I_{D^+} is the intensity of D^+ ions, I_{2D} is the peak intensity at a m/n ratio of 2 Da. The proportions of H^+/H_2^+ and D^+/D_2^+ against electric field was shown in Figure 4.5b that almost superimposable variation trends were obtained. Taking account of all the results thus obtained, we concluded that the residual H detected in AP measurement originates from the H_2 gas adsorbed on Pt surface rather than the hydrogen in the Pt tip. Figure 4.6 shows the surface distribution of D^+ and D_2^+ on Pt sample in D_2 gas atmosphere (2.0×10^{-6} Pa) by pulse laser with an electric field of 27.8 V nm^{-1} . The distribution of D_2^+ ions (green spots) on the Pt surface illustrated the areas with higher local electric fields on Pt surface. The D^+ ions (blue spots) distribution showed a similar pattern, but the ions intensity was weaker, which also implied that D_2^+ ions were more easier to be evaporated than D^+ ions.

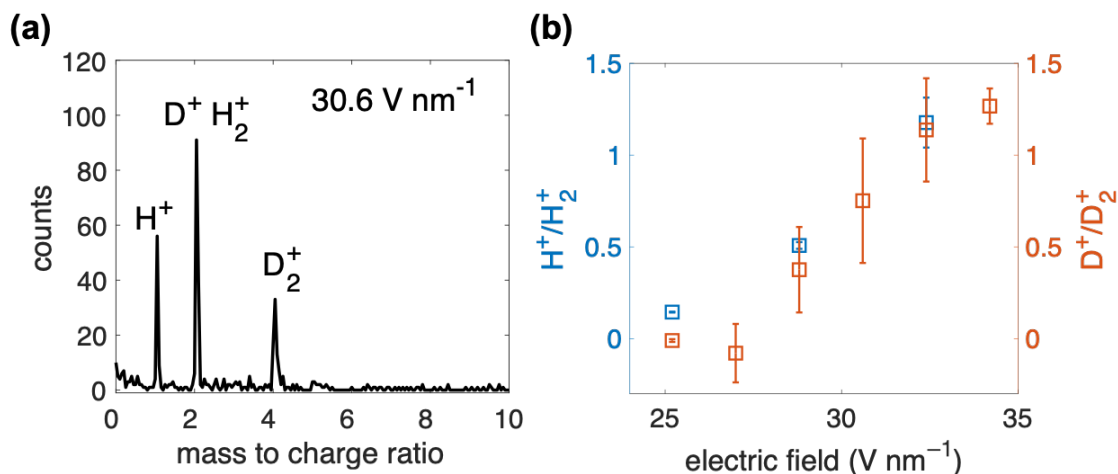


Figure 4.5 (a) Mass spectrum of residual hydrogen and deuterium on Pt surface by pulse laser with an electric field of 30.6 V nm^{-1} ($6.0 \times 10^{-8} \text{ Pa}$, 60 K). The D_2 gas pressure was reduced from $2.0 \times 10^{-6} \text{ Pa}$ to $6.0 \times 10^{-8} \text{ Pa}$. (b) A plot of the variation of the intensity ratios of H^+/H_2^+ and D^+/D_2^+ against electric field.

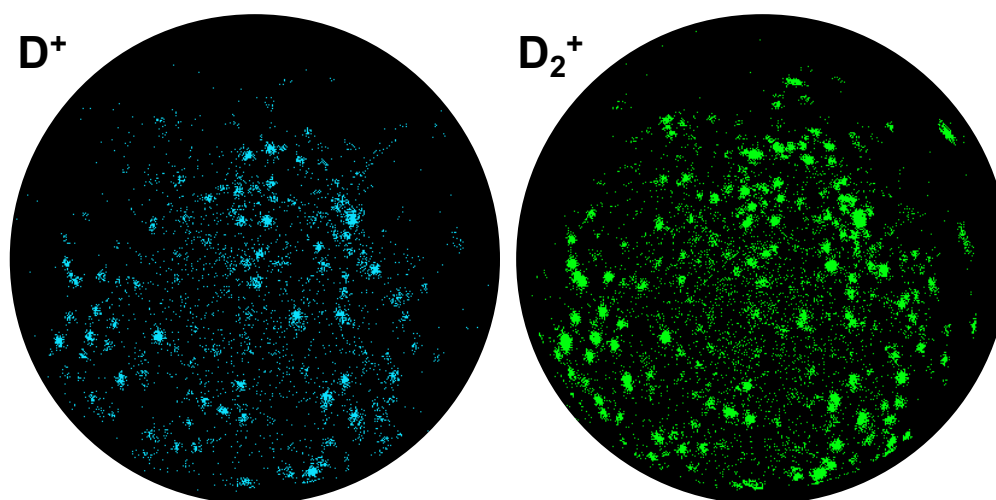


Figure 4.6 The 2D distribution maps of (left) D^+ ions and (right) D_2^+ ions on Pt surface by a pulse laser with an electric field of 27.8 V nm^{-1} with D_2 gas atmosphere ($2.0 \times 10^{-6} \text{ Pa}$) at 60 K. D_3^+ ions were not detected in this condition.

4.3 Specimen Shape Effect

The ratio of H^+ to H_2^+ varied as the specimen surface shape changed. As shown in Figure 4.7, the intensity of H^+ ions increased faster on a flat specimen surface than that of a sharp specimen surface as the electric field increased. The ratio of H^+ to H_2^+ was

even over 2 on a flat specimen surface with the electric field of 40 V nm^{-1} , in contrast, the ratio of H^+ to H_2^+ was less 2 on a sharp specimen at the same condition. This phenomenon can be explained that the electric field refers to the electric field on the apex. As shown in Figure 4.8, as a result, the on a flat specimen surface, the average electric field is larger than that on a sharp surface, which has been calculated in chapter 3.

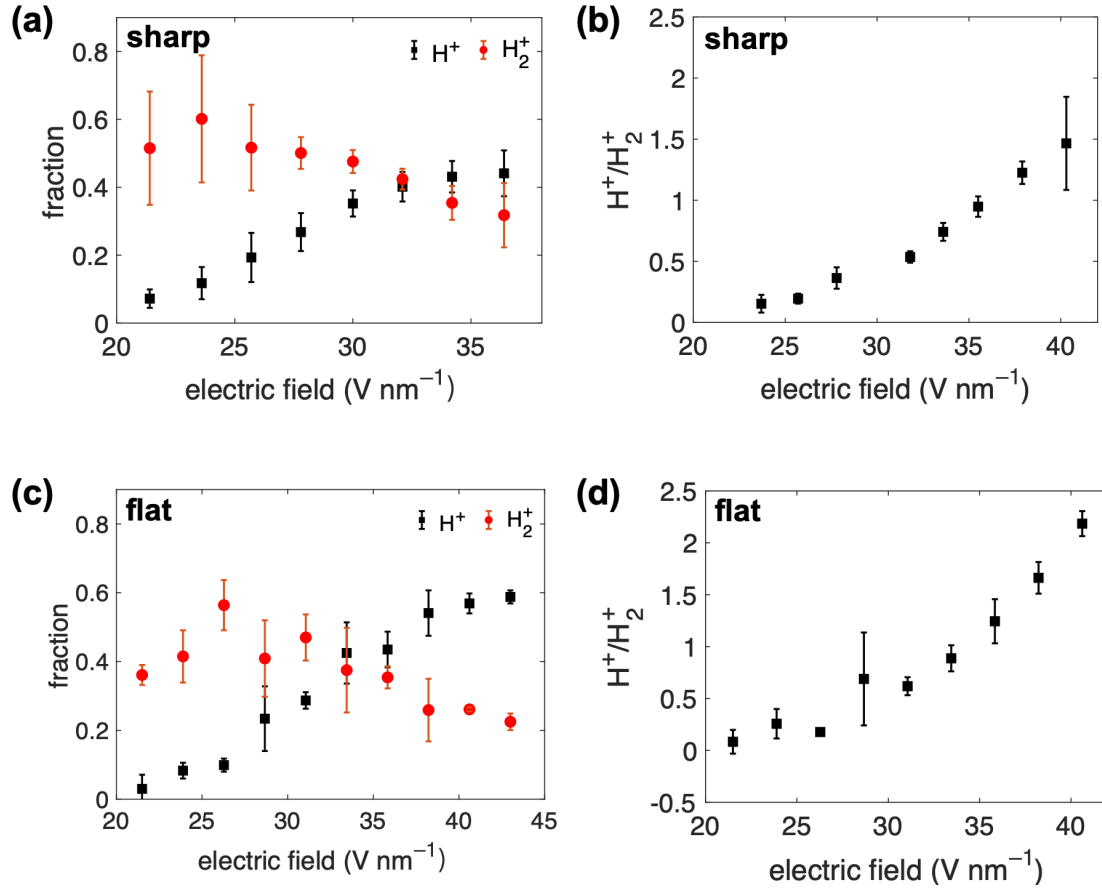


Figure 4.7 A plot of (a) hydrogen (Pt, 60 K, background pressure: 10^{-8} Pa) signal fractions and (b) ratio of H^+ to H_2^+ with respect to electric field from 21.4 V nm^{-1} to 36 V nm^{-1} on a sharp specimen surface. A plot of (c) hydrogen (Pt, 60 K, background pressure: 10^{-8} Pa) signal fractions and (d) ratio of H^+ to H_2^+ with respect to electric field from 21.4 V nm^{-1} to 42 V nm^{-1} on a flat specimen surface.

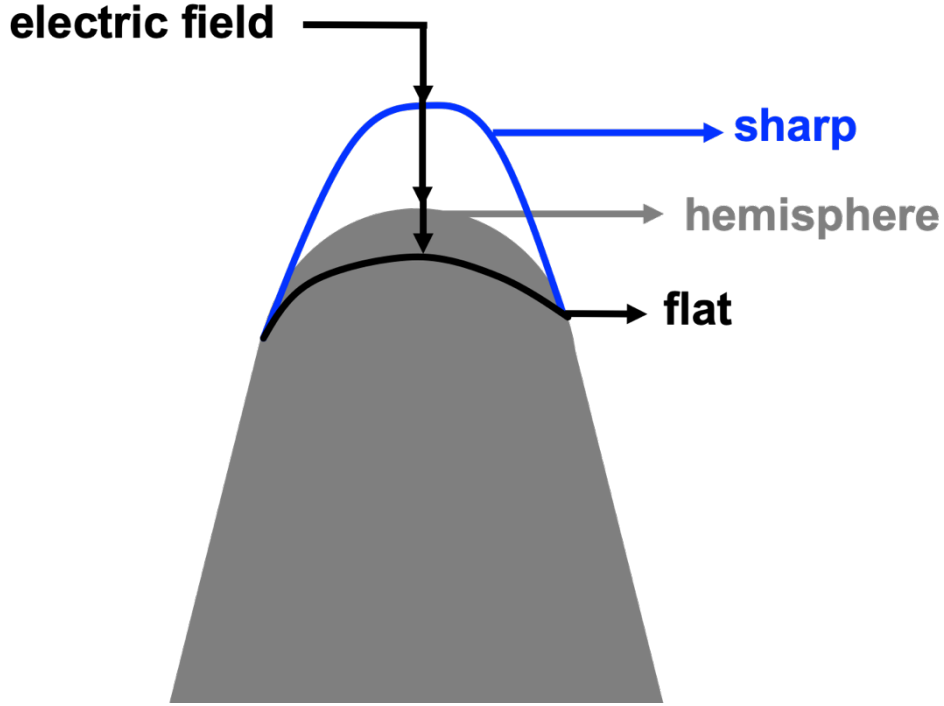


Figure 4.8 The schematic diagram of sharp and flat specimen surface and a hemisphere.

4.4 Field Adsorption

It was surprising to us that the maximum evaporation rate of H species is as high as 17 counts/second even in ultra-high vacuum (10^{-8} Pa). The accumulation and adsorption of H_2 gas on the AP sample surface can be ascribed to dipole-dipole interaction when subjected to a high electric field [8,11,13]. This model well describes the mechanism of gas adsorption in a short range. Here the short-range is defined as an atomic radius or less. The binding energy H_A is expressed by the following equation.

$$H_A = \frac{1}{2} \alpha_A (f_A - 1) F_0^2 \quad (4.3)$$

Where α_A is the polarizability of a gas atom or molecule; F_0 is the electric field; f_A is the enhancement factor given by

$$f_A = \left[\frac{1 + (\alpha_M/d^3)}{1 - (4\alpha_A\alpha_M/d^6)} \right]^2 \quad (4.4)$$

where α_M is the polarizability of the substrate surface atom and d is the equilibrium distance between the surface atom and the adsorbing species. Figure 4.9 exhibits the short-range binding energy of a H_2 gas molecule on Pt metal surface as a function of electric field calculated using Eqs. (3) and (4) that the binding energy is monotonically increasing with electric field, suggesting that H_2 gas molecule would

diffuse along the shank to sample apex due to electric field gradient, which considerably improve the H_2 gas concentration on the top of sample surface even in extremely high vacuum [14,15].

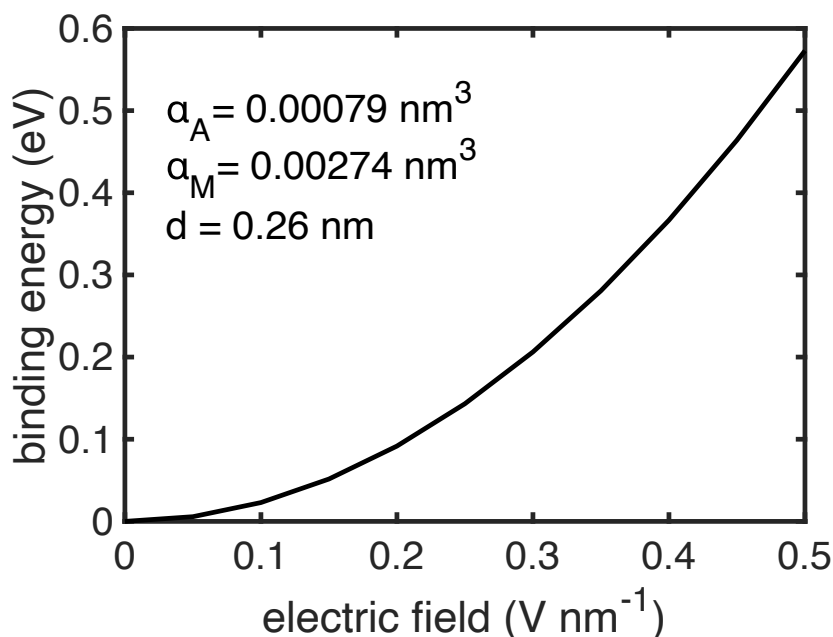


Figure 4.9 A plot of the binding energy for field-adsorbed residual H_2 gas on Pt metal surface atom as a function of electric field.

4.5 Field Desorption

Having demonstrated the hydrogen adsorption on Pt sample under ultra-high vacuum for AP measurement, we sought for the mechanism of the formation and desorption of H^+ , H_2^+ and H_3^+ on Pt sample surface. In Kellogg's model[11], the instantaneous temperature rise produced by laser pulse thermally desorbs the molecule as a neutral. This molecule then is ionized at the critical distance away from surface with a sufficient electric field. This study also suggested the formation of H_2^+ (D_2^+) ions is attributed to H_2 (D_2) gas desorption triggered by a thermally activated process.

For the formation of the H_3^+ (D_3^+) ion, three processes have been proposed: $H_2^+ + H \rightarrow H_3^+$, $H_2 + H^+ \rightarrow H_3^+$ and $H_3 \rightarrow H_3^+$ [9,13]. The first two processes argued that the ions (H_2^+ or H^+) collide a neutral atom or molecule to produce a H_3^+ ion. However, once the atom or molecule was ionized, it would fly away from sample surface so as to significantly reduce the collision possibility. Therefore, the formation H_3^+ (D_3^+) can be rationalized by the direct desorption of H_3 (D_3) molecule on Pt surface. Although H_3 (D_3) molecules are unstable in free space, they could be stabilized in the presence of a

high electric field. The formation of H_3 (D_3) molecule stems from the combination of H_2 (D_2) and $H(D)$, implying the coexistence of molecules $H_2(D_2)$ and atoms $H(D)$ on sample surface. We thus proposed that the formation of triatomic cation can be expressed by the following Eq. 4.5 [9]



Figure 4.10 shows the surface distribution of D^+ , D_2^+ and D_3^+ on Pt sample in D_2 gas atmosphere (2.0×10^{-6} Pa) by a pulse laser with an electric field of 32.1 V nm^{-1} . The 2D distribution maps show the predominance of D_2^+ ions and D_3^+ ions appears at the edge of sample surface, while the D^+ ions on the apex area, where the electric field was higher than the other area, indicating the electric field necessary to ionize H_3 (D_3) and H_2 (D_2) is lower than that for $H(D)$ atom.

In light of the conclusion drawn above, we interpret the formation of H^+ (D^+) as follows. In the $H_3(D_3)$ formation process, $H(D)$ atom is expected to originally exist on the Pt surface. The H^+ (D^+) ions may desorbed from the strongly adsorbed $H(D)$ atoms, which are generated from a dissociation of H_2 (D_2) on Pt surface. As the binding energy of $H(D)$ atoms were much larger than that of $H_2(D_2)$ molecules, $H^+(D^+)$ ions emitted by high electric fields, while $H_2^+(D_2^+)$ ions require a low electric field. Our scenario is different from Kellogg's. In Kellogg's model, it is suggested the occurrence of H^+ ions is due to the desorption of H_2^+ ions followed by ionization or dissociation of a subset of these ions, where high electric field permits this process [11]:

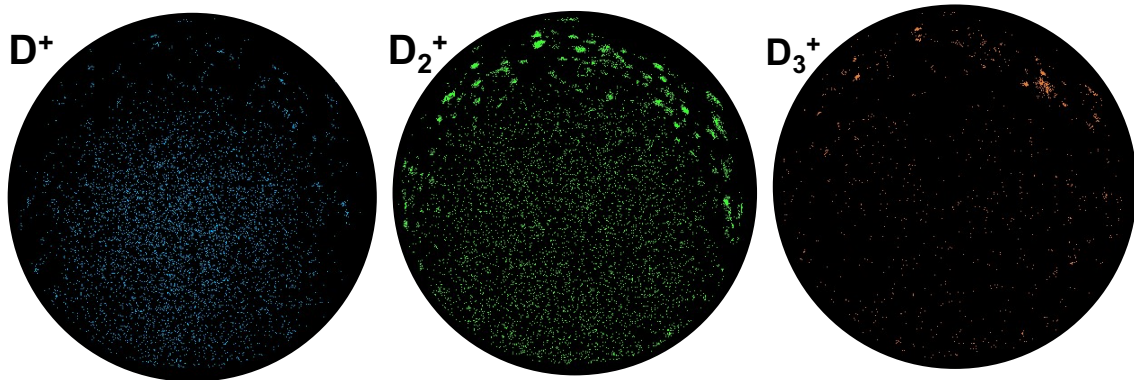


Figure 4.10. 2D distribution maps of (left) D^+ ions, (middle) D_2^+ , and (right) D_3^+ ions on Pt surface by a pulse laser with an electric field of 32.1 V nm^{-1} in D_2 gas atmosphere (2.0×10^{-6} Pa) at 60 K.

4.6 Conclusion

In summary, the residual hydrogen in ultra-high vacuum on Pt surface was systematically investigated by AP analyses. Three hydrogen species, H^+ , H_2^+ , and H_3^+ ions, can be detected on Pt surface with background pressure of 2×10^{-8} Pa. H^+ ions are more likely to be detected at high electric field; the observation of H_2^+ and H_3^+ requires relatively low electric field. In isotope labelling experiments using D_2 with two kinds of pressure conditions (2×10^{-6} Pa and 2×10^{-8} Pa), comparisons could be made between D^+/D_2^+ and H^+/H_2^+ with respect to electric field, which revealed that the residual hydrogen is from the H_2 gas in the UHV chamber. Calculation of field-induced binding energy of H_2 gas and sample surface suggested a considerable enhancement the H_2 gas concentration on the sample surface upon applying high electric field. The accumulated hydrogen gas on Pt sample surface can be regarded as a reactant gas in my future research.

This study further suggests when studying the H or D trapping in an AP sample, the background intensity of H^+ , H_2^+ and H_3^+ ions in certain operation parameters need to be carefully analysed, as these signals may overlap with the probed ions signal in mass spectra.

4.7 Reference

1. R. Lewis and R. Gomer, Adsorption of hydrogen on platinum. *Surf. Sci.* **17**, 333–345 (1969).
2. P. Kesten, A. Pundt, G. Schmitz, M. Weisheit, H.U. Krebs, R. Kirchheim, H- and D-distribution in metallic multilayers studied by 3-dimensional atom probe analysis and secondary ion mass spectrometry. *J. Alloys Compd.* **330**, 225–228 (2002).
3. K. Tatsumi, S. Muto, T. Yoshida, Detection of hydrogen at localized regions by unoccupied electronic states in iron carbides: Towards high spatial resolution mapping of hydrogen distributions. *J. Appl. Phys.* **101**, 023523 (2007).
4. Y. J. Kim, R. Tao, R. F. Klie, D. N. Seidman, Direct atomic-scale imaging of hydrogen and oxygen interstitials in pure niobium using atom-probe tomography and aberration-corrected scanning transmission electron microscopy. *ACS nano.* **7**, 732–739 (2013).
5. Y.S. Chen, D. Haley, S. S. A. Gerstl, A. J. London, F. Sweeney, R. A. Wepf, W. M. Rainforth, P. A. J. Bagot, M. P. Moody, Direct observation of individual hydrogen atoms at trapping sites in a ferritic steel. *Science* **355**, 1196–1199 (2017).
6. H. Takamizawa, K. Hoshi, Y. Shimizu, F. Yano, K. Inoue, S. Nagata, T. Shikama and Y. Nagai, Three-dimensional characterization of deuterium implanted in silicon using atom probe tomography. *Appl. Phys. Express* **6**, 066602 (2013).
7. J. Takahashi, K. Kawakami, Y. Kobayashia and Toshimi Tarui, The first direct observation of hydrogen trapping sites in TiC precipitation-hardening steel through atom probe tomography. *Scri. Mater.* **63**, 261–264 (2010).
8. R. Prakash Kolli, Controlling residual hydrogen gas in mass spectra during pulsed laser atom probe tomography. *Adv. Struct. Chem. Imag.* **3**, 10 (2017).
9. Z. M. Stepien, T. T. Tsong, Formation of metal hydride ions in low-temperature field evaporation. *Surf. Sci.* **409**, 57–68 (1998).
10. G. Sundell, M. Thuvander, H.-O. Andrén, Hydrogen analysis in APT: Methods to control adsorption and dissociation of H₂. *Ultramicroscopy* **132**, 285–289 (2013).

11. G. J. Kellogg, Pulsed laser stimulated field desorption of hydrogen from molybdenum. *J. Chem. Phys.* **74**, 1479–1487 (1981).
12. S. Chen, T. Suzuki, B. Tomiyasu, M. Owari, *Surf. Interface Anal.* (in press)
13. T. T. Tsong, E. W. Muller, Field adsorption of inert-gas atoms. *J. Chem. Phys.* **55**, 2884–2889 (1971).
14. M. J. Southon, *Image formation in the field ion microscope*, PhD Thesis, University of Cambridge, (1963).
15. H. D. Beckey. Principle of Field Ionization and field Desorption Mass Spectrometry. (Pergamon Press, Oxford, 1977), Chapter 1.

CHAPTER 5 HYDROGEN OXIDATION REACTION ON Pt

The reaction of O₂ and residual hydrogen (H) over platinum in high vacuum, at temperatures from 60 K to room temperature, was studied by using field-evaporation techniques, including field ion microscopy (FIM) and atom probe (AP), which enabled *in-situ* analysis of surface structure and chemical composition analysis at atomic scale. This study aimed to obtain detailed information about the reaction of O₂ and residual H on a Pt surface. The factors affecting the reaction were also investigated in detail.

The experiments were performed as follows. FIM images of clean tip specimens were taken in the helium gas at 60 K. Surface reactions were studied using an *in-situ* AP at the oxygen pressure of 10⁻⁵ Pa and at temperatures ranging from 60 K to 300 K. For all the experiments, no H₂ gas was introduced into the chamber. A reaction at the temperature of interest was monitored by implementing the experiment at the specific time after turning off the cryogenerator. The temperature of the sample holder as a function of time is shown in Figure 5.1.

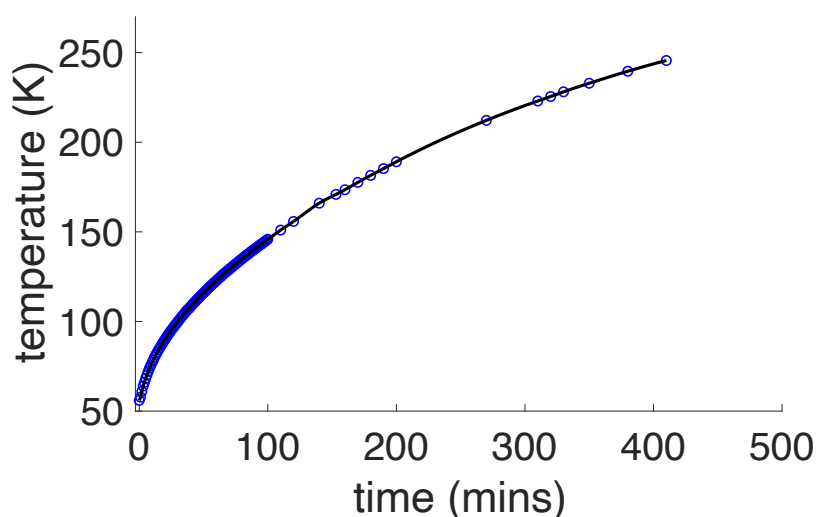


Figure 5.1 The temperature of specimen holder as a function of the time since turning off the cryogenerator.

5.1 FIM Image

An FIM image of a Pt tip prepared as described in the experimental section is shown in figure 5.2a. The tip was imaged in helium at 60 K with a static voltage 8.6 kV (the field strength around of 44 V nm⁻¹), after cleaning the tip by cycles of evaporation.

The concentric rings observed in FIM images demonstrates the specific geometry of the specimen surface, which can enable the determination of the radius of curvature or shank angle of the specimen. As shown in Figure 5.3, the successive terraces between two planes centers correspond to an increment equal to the interplanar spacing along the directions of planes. The θ is the angle between these two crystallographic directions of $h_1k_1l_1$ and $h_2k_2l_2$. Therefore, a relationship can be established to calculate the radius of curvature of the specimen R_o , as follows:

$$R_o(1 - \cos \theta) \approx nd_{h_1k_1l_1} \quad (5.1)$$

Where n is steps between two planes. The calculation method of interplanar spacings and angles between planes of different crystal structure are introduced in appendix B and C, respectively.

Therefore, the radius of curvature was estimated to be about 40 nm by counting the number of rings between the (111) and (131) planes.

A ball model (Figure 5.2b) with 40 nm radius shows a good similarity with the FIM image. The code to make a fcc crystal ball is given in appendix H. The planes on crystal surface can also be identified by the stereographic projections (appendix D).

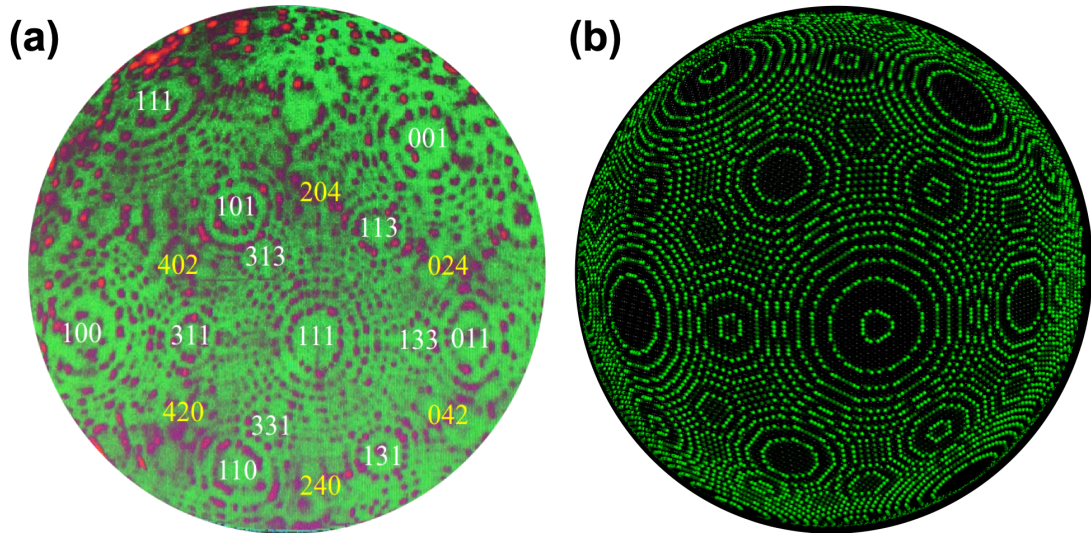


Figure 5.2 (a) Field ion micrograph of the Pt surface, imaged under helium gas (10^{-5} Pa) at 60 K. The radius of curvature was about 40 nm. (b) A ball model demonstrating a similar pattern to identify the planes on specimen surface.

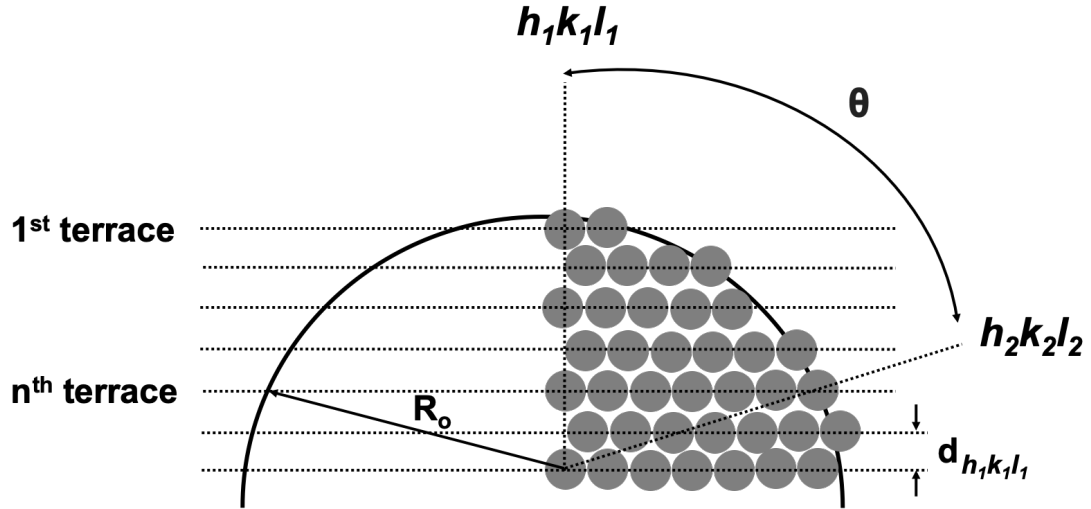


Figure 5.3 Schematic view of the interplanar successive terraces of the specimen. $h_1 k_1 l_1$ and $h_2 k_2 l_2$ are two crystallographic directions. θ is the angle between these two crystallographic directions. $d_{h_1 k_1 l_1}$ is the distance between each successive terrace of $h_1 k_1 l_1$ direction. R_o is the radius.

5.2 Temperature Effect

The detection of H species on the Pt surface under a high vacuum condition (10^{-8} Pa) and low temperature (60 K) condition was achieved using a pulse laser. Figure 4 shows the mass spectra of H species for different electric field. The signals of H_2^+ and H_3^+ appeared (Figure 5.4a) at a relatively low electric field of 20 V nm^{-1} . As electric field increased, H^+ species was detected (Figure 5.4b and Figure 5.4c). Note also that, H_2^+ was observed as dominant species.

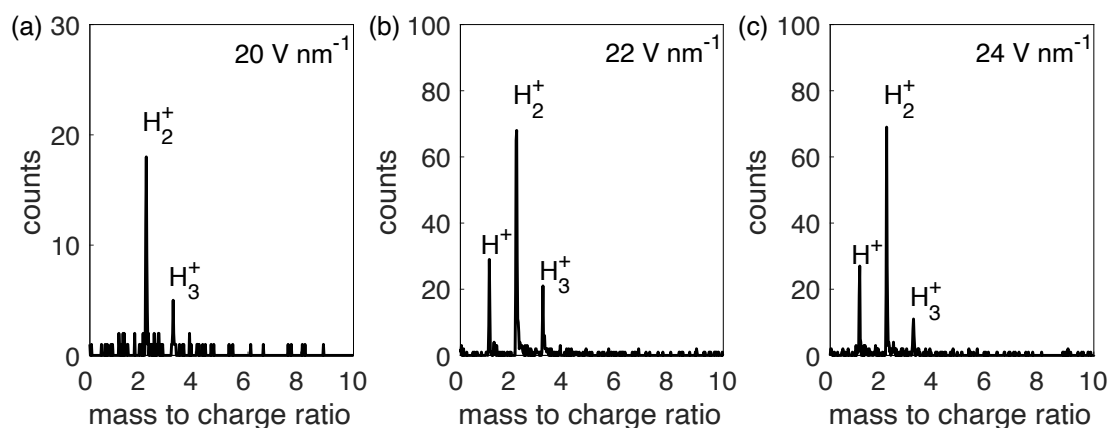


Figure 5.4 Mass Spectra of residual H acquired from the 60 K Pt surface in high vacuum (10^{-8} Pa) by pulse laser (pulse energy was constant at 2.5 nJ/pulse). Evaluated experimental conditions: (a) static field $\sim 20 \text{ V nm}^{-1}$; (b) static field $\sim 22 \text{ V nm}^{-1}$; (c) static field $\sim 24 \text{ V nm}^{-1}$.

O_2 gas (10^{-5} Pa) was introduced to the main chamber to study the reaction of O_2 with H species on the Pt surface. The chemical composition and distribution were recorded by AP at the temperature ranging from 60 K to room temperature. Four typical mass spectra were shown in Figure 5.5, and all the peaks appeared in the mass-to-charge (m/n) range from 10 to 50. Therefore, the enlarged figures were made to clearly exhibit the peaks (Figure 5.6). At 60 K, the signal of O_2^+ was solely detected on the Pt surface without the formation of H_2O (Figure 5.6a). When the temperature increased to 135 K, the H_2O^+ peak appeared as shown in Figure 5.6b. Upon further increasing the temperature, the signal of H_3O^+ and O^+ signals emerged, suggesting the protonation of H_2O species and the dissociation of O_2 , respectively. Apparently, H_2O^+ and H_3O^+ were the products of the reaction between oxygen and residual H on the Pt surface. These results suggest that an appropriate high temperature (125 K for the Pt tip) is essential for the formation of H_2O .

The intensity of the products, H_2O^+ and H_3O^+ increased significantly from 145 K to 210 K, compared with the reactant O_2^+ (Figure 5.6c and Figure 5.6d), which can be explained as the reaction accelerated as the temperature increased with sufficient H and O supply.

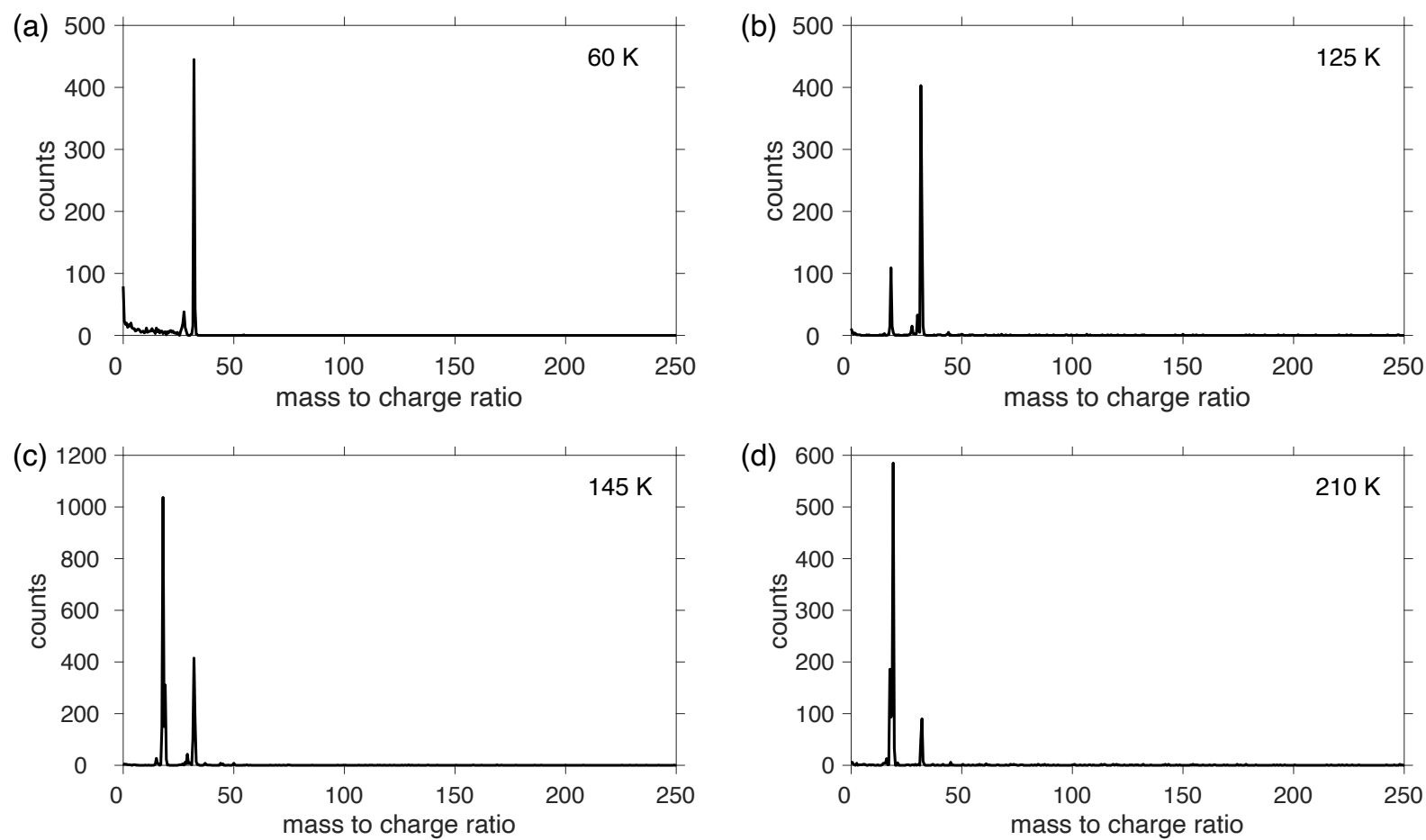


Figure 5.5 Mass Spectra (full scale) of the interaction of O_2 (10^{-5} Pa) and H species on the Pt tip by pulse voltage, for different temperature: (a) 60 K; (b) 130 K; (c) 145 K; (d) 210 K. The static voltage was ~ 5.0 kV, and the pulse voltage was 1.0 kV

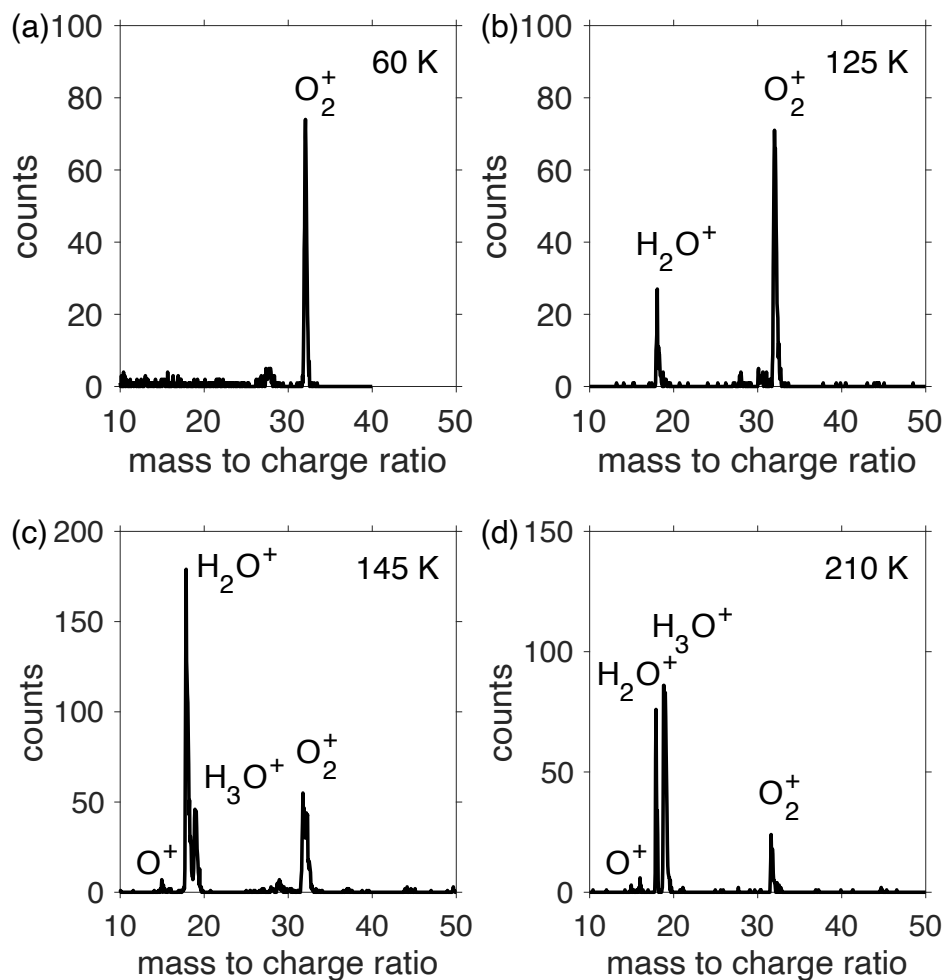


Figure 5.6 Mass Spectra (m/n from 10 to 50) of the interaction of O_2 (10^{-5} Pa) and H species on the Pt tip by pulse voltage, for different temperature: (a) 60 K; (b) 125 K; (c) 145 K; (d) 210 K. The static voltage was ~ 5.0 kV, and the pulse voltage was 1.0 kV.

5.3 Active Site

Next, AP was conducted to analyse the chemical species distribution on the metal surface. Four peaks, H_2O^+ , H_3O^+ , O_2^+ and $O_2H_{4-6}^+$, were clearly observed in the mass spectrum (Figure 5.7a) at 150 K. The distributions of H_2O^+ , H_3O^+ , O_2^+ and $O_2H_{4-6}^+$ on the Pt surface are shown in Figure 5.7b, c d and e, respectively. No target ions were evaporated from the black area. Generally, the green colour displays the distribution of those ions that were locally evaporated from the Pt surface during the detection duration. Several red spots imply that the intensity of the target ion is extremely high at those points.

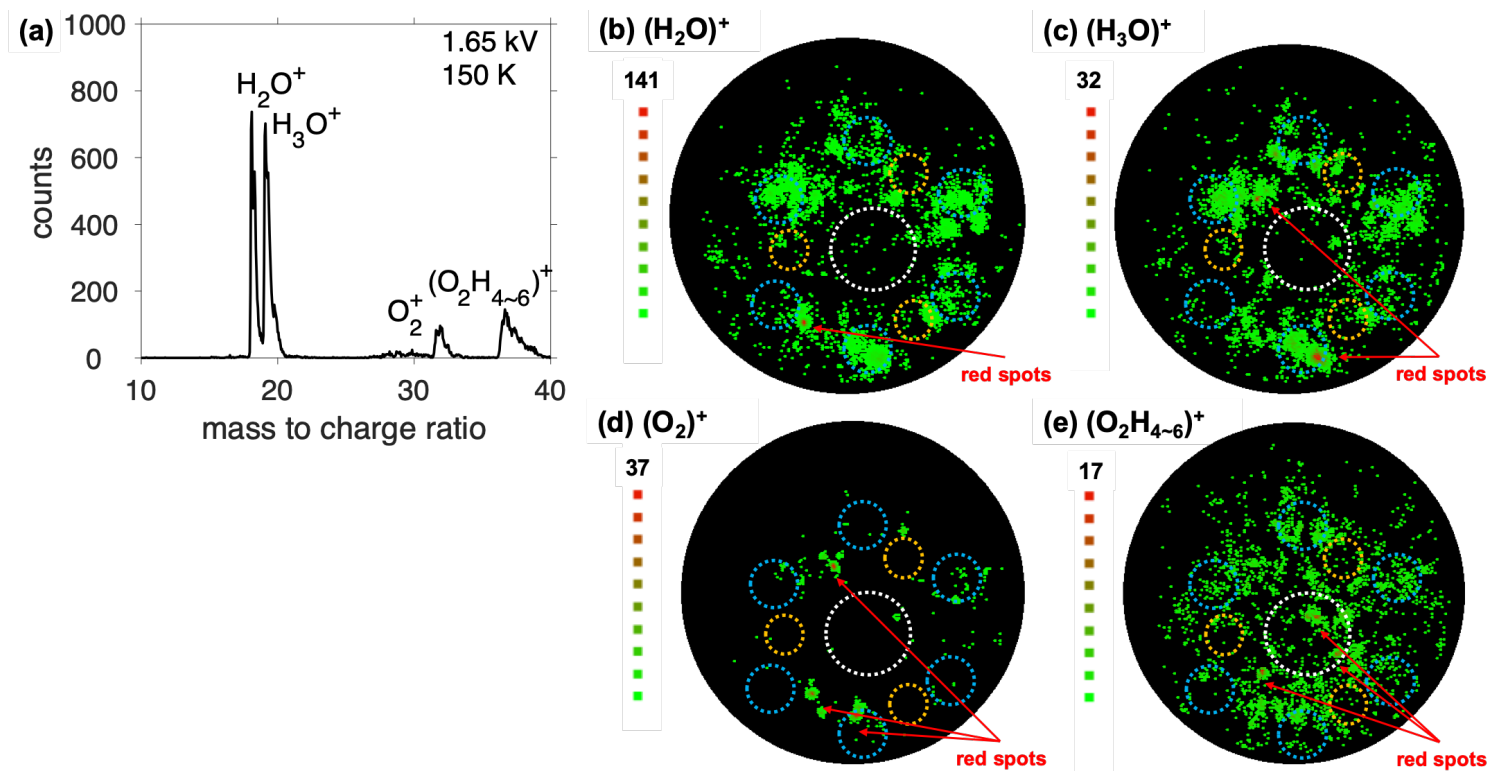


Figure 5.7 Mass spectrum of the reaction between O_2 (10^{-5} Pa) and H species on the Pt tip by pulse voltage at 150 K, with the standing voltage of 1.65 kV and pulse voltage of 0.4 kV; b) H_2O^+ distribution, c) H_3O^+ distribution, d) O_2^+ distribution, e) $\text{O}_2\text{H}_{4-6}^+$ distribution on the Pt surface. In each picture, the pixel spans 200×200 . The colour of the pixels represents the intensity of the chemical components. Black corresponds to no signal counts. The colour ranging green to red corresponds to the counts increasing linearly from 1 to a maximal number (shown on the top of the colour scale). The white dash ring, blue dash rings and orange dash rings in b) represent the $\{111\}$, $\{240\}$, and $\{113\}$ planes, respectively. The angular displacement between the center and the corner edge of the detection area is 1 rad (57.3°), corresponding to 57 mm in the coordinate used here

This could be explained as follows. The evaporation rate of the process obeys the Arrhenius law [1]. The evaporation rate at time t , $\Phi(t)$, at temperature T and pulse duration t can be expressed as

$$\Phi(t) \approx Nv\tau_t \exp\left(\frac{-Q_n(F_o)}{k_B T}\right) \quad (5.2)$$

where N is the number of the species present on the surface, v is the vibrational frequency of the surface atom, k_B is the Boltzmann's constant, and $Q_n(F_o)$ is the activation energy, which usually increases monotonically with electric field F_o . Therefore, the red spots may result from a large quantity of target ions produced or adsorbed around this point. Alternatively, the local electric field may be sufficiently high to induce evaporation of adsorbed molecules with sufficient supply. In short, there must be a mass of target ions adsorbed around red spots.

The O_2^+ and $O_2H_{4-6}^+$ chemical species representing O_2 , almost uniformly adsorbed on the Pt specimen surface. Comparison of these images with the FIM micrograph (Figure 5.2a) demonstrates that H_2O almost was not generated in the $\{111\}$ planes. The active sites for the H_2O generation, however, were in the $\{240\}$ planes, where the red spots were spread. In addition, H_3O^+ was sparsely distributed in the $\{111\}$ planes, but was clustered in the $\{240\}$ and $\{113\}$ planes, as indicated by the red spots, suggesting that the planes surrounding the $\{111\}$ planes have higher reactivity for H_2O^+ and H_3O^+ generation, such as the $\{240\}$ and $\{113\}$ planes. O_2^+ was likely evaporated on the rim of the planes. We attributed the particular reactivity of the planes surrounding the $\{111\}$ plane to their large specific surface area. Figure 5.8 shows the atomic structures of the $\{240\}$, $\{110\}$ and $\{111\}$ planes, based on which we speculated that the adsorption of molecular O_2 and the dissociation of O_2 to atomic O were stronger for the more corrugated planes. Accordingly, a possible reaction process was proposed. O_2 was adsorbed on the Pt surface and further dissociated to O atoms. The dissociated atomic O reacted with the residual H, which can be derived from the H_2 diffused on the Pt surface or the H atoms/molecules stored in the Pt tip on the Pt surface at temperatures above 135 K, for the formation of H_2O .

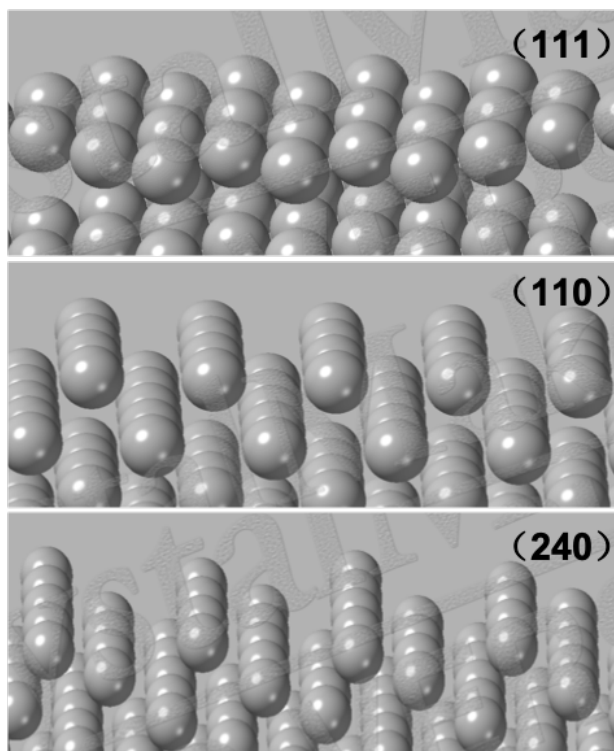


Figure 5.8 Surface corrugations of the Pt (111), (110), and (240) surfaces.

5.4 Laser Pulse

In **section 5.3**, the chemical species of on-going reaction were recorded in voltage pulse mode. The laser pulse was employed in this section compare the results with the above. As shown in Figure 5.9, at 60 K, the signal of O_2^+ could be detected on the Pt surface without the formation of H_2O (Figure 5.9a). However, when the temperature increased to 135 K, the H_2O^+ peak didn't appear as shown in Figure 5.9b. Upon further increasing the temperature to 145 K (Figure 5.9c), peaks of H_3O^+ and H_2O^+ signals emerged, but the intensity is far smaller than that in voltage mode. Then I switching the laser pulse to voltage pulse, the intensity of H_3O^+ and H_2O^+ signals exceeded the O_2 signals (Figure 5.9d). These results suggest that the thermal energy of laser pulse may decrease the local concentration of H_2 gas, which weaken the reaction speed on Pt surface.

Frankly speaking, field evaporation mechanism by laser pulse is still under debate and thermal desorption cannot explain all the field evaporation triggered by laser pulse due to its short duration (several femtosecond). However, in this experiment, the residual hydrogen is believed to be evaporated by laser thermal power. In that, all the

residual hydrogen can be only detected in the laser pulse mode rather than the voltage pulse mode. By voltage pulse, no hydrogen signals were shown in the mass spectra. Meanwhile, by changing the energy of laser pulse, only the hydrogen quantity decreased as the energy decreased, the ratio of H^+/H_2^+ was not affected, as shown in Figure 5.10.

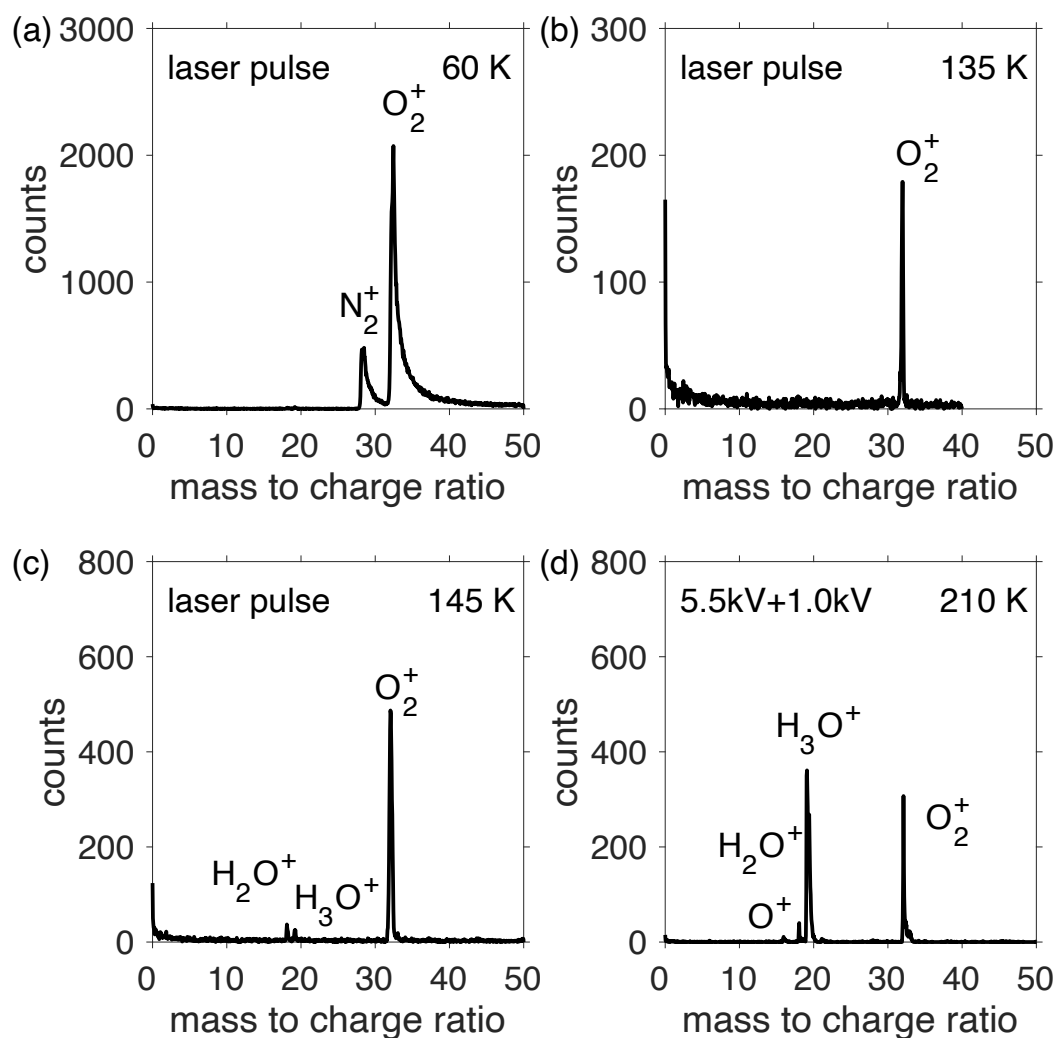


Figure 5.9 Mass Spectra (m/n from 0 to 50) of the interaction of O_2 (10^{-5} Pa) and H species on the Pt tip in different conditions: (a) 60 K, laser pulse; (b) 130 K, laser pulse; (c) 145 K, laser pulse; (d) 210 K, voltage pulse.

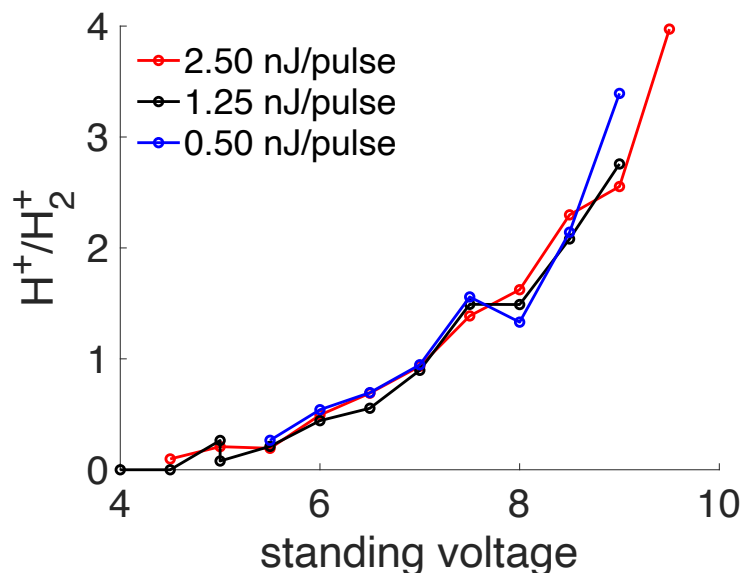


Figure 5.10 The intensity ratio of H^+ ions and H_2^+ ions with respect to standing voltage at different laser pulse energy, 2.5 nJ/ pulse, 1.25 nJ/ pulse, and 0.5 nJ/ pulse on 60 K Pt surface.

5.5 Electric Field

The electric field is a significant experimental parameter in AP operation, which is proportional to the applied voltage. In this section, the effects of static voltage and the value of static voltage in AP analysis will be explored.

5.5.1 The Static Voltage

To investigate the influence of the presence of static voltage in hydrogen oxidation reaction on Pt surface, the AP experiments were conducted in two conditions: (1) 2.5 kV static voltage plus 0.5 kV voltage pulse; (2) 3.0 voltage pulse. The total value was same. As shown in Figure 5.11, in the presence of static voltage (blue), the peaks of m/n of 18, 19, 32 and 36 corresponding to the H_2O^+ , H_3O^+ , O_2^+ and $O_2H_{4-6}^+$ ions, indicated the occurring of the hydrogen oxidation reaction. In the absence of static voltage, the mass resolution is dramatically decreased, where the peak width got broader. Nevertheless, it was clear that only O_2^+ was appeared in mass spectrum, but on signals in the m/n of 18, 19, implying no products generated. It may result from the concentration of residual hydrogen gas significantly decreased in the absence of static voltage, which leads to no reaction taking place on Pt surface.

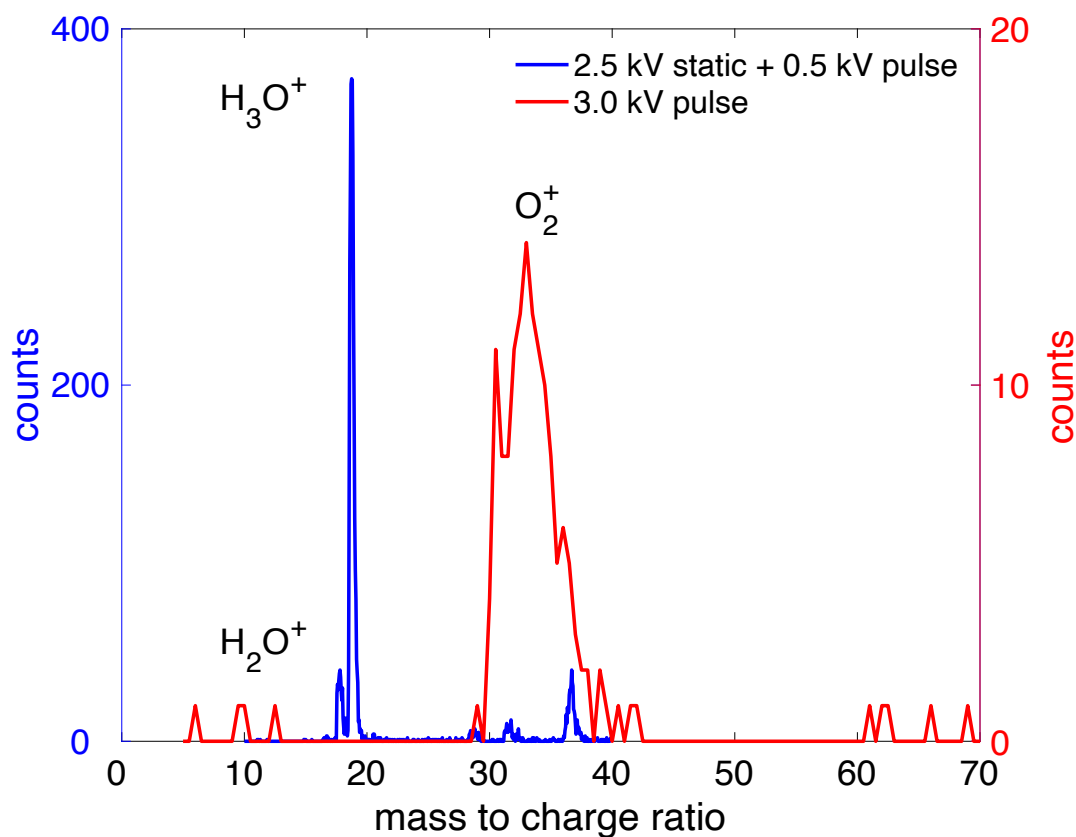


Figure 5.11 Mass Spectrum (m/n from 0 to 70) of the interaction of O_2 (10^{-5} Pa) and H species on the Pt tip in different conditions: 2.5 kV static voltage + 0.5 kV voltage pulse (blue line) and 3.0 voltage pulse.

5.5.2 The Value of Static Voltage

As explained in Chapter 3, an electric field is a key parameter to detect the signals as synchronous ions. Every specific chemical species has its own proper evaporation field. However, upon the on-going reaction, a mixture of reactants, products and intermediates may coexist on specimen surface. As a result, more attention should be paid to electric field (applied voltage) setting. For instance, at the temperature of 150, two mass spectra were obtained in different static voltage condition 1.65 kV and 2.0 kV with 0.4 kV voltage pulse. As can be seen in Figure 5.12, the peak of $O_2H_{4-6}^+$ ions disappeared as the static voltage increased from 1.65 kV to 2.0 kV. Therefore, the standing voltage and voltage pulse should be adjusted to find out all signals on AP sample surface.

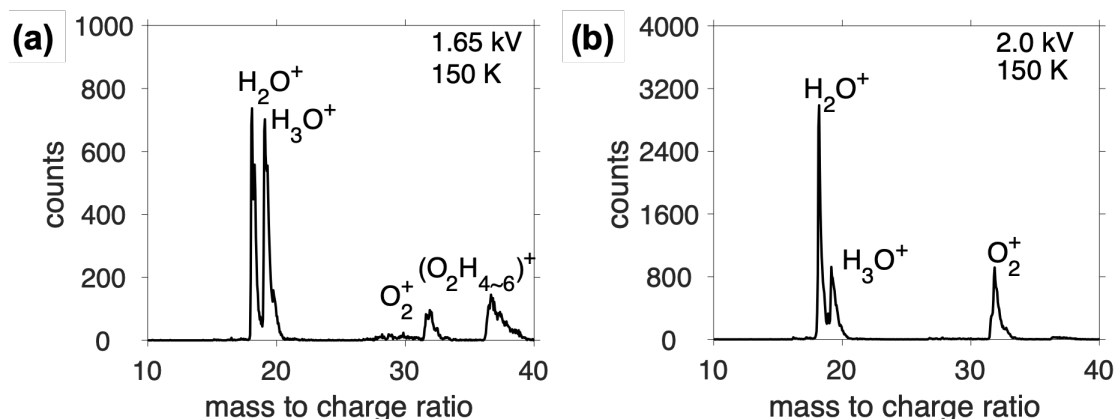


Figure 5.12 Mass spectra of the reaction between O_2 (10^{-5} Pa) and H species on the Pt tip by pulse voltage at 150 K, with the standing voltage of 1.65 kV (a), 2.0 kV (b) and pulse voltage of 0.4 kV.

5.6 Surface Corrosion

As the hydrogen oxidation reaction taking place on Pt catalyst, the specimen surface was corroded. At the 60 K, H_2 gas and O_2 physically adsorbed on Pt surface. Consequently, the signals at 60 K on Pt surface is merely H_2^+ and O_2^+ . As the temperature increased, a part of the physically adsorbed gas would desorb from Pt surface, but the remaining gas would chemically bonded to Pt surface. As a result, except reactants and products, some complex ions could be detected due to the strong chemical bond. As shown in Figure 5.13, $\text{Pt}_x\text{O}_y^{n+}$ signals were detected, suggesting that the Pt surface was oxidized during the hydrogen oxidation reaction. In contrast, the oxidized Pt surface can promote the oxidation reaction[2,3]. Another evidence proving the surface corrosion is the FIM images before and after reaction. The Figure 5.14a is the the FIM image of a fresh sample. After one round reaction (Figure 5.14b) and (Figure 5.14c), the surface was too rough to get a FIM image with clear concentric rings on each crystallographic direction. Besides, the radii of curvature got increased after every round.

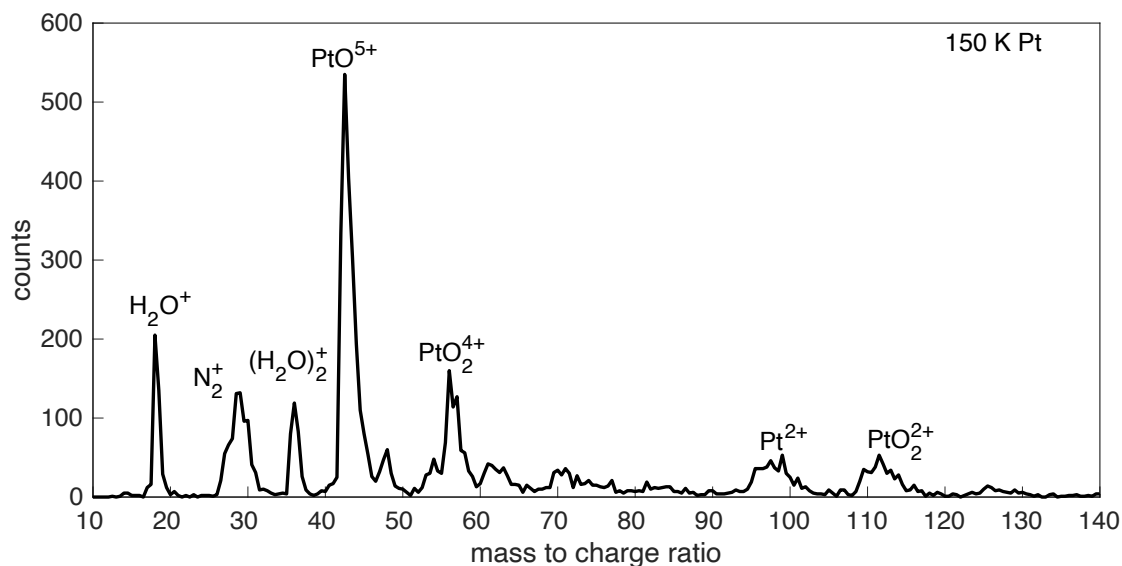


Figure 5.13 Mass spectrum of the reaction between O_2 (10^{-5} Pa) and H species on the Pt tip by pulse voltage at 150 K, with the standing voltage of 1.2 kV pulse voltage of 0.3 kV.

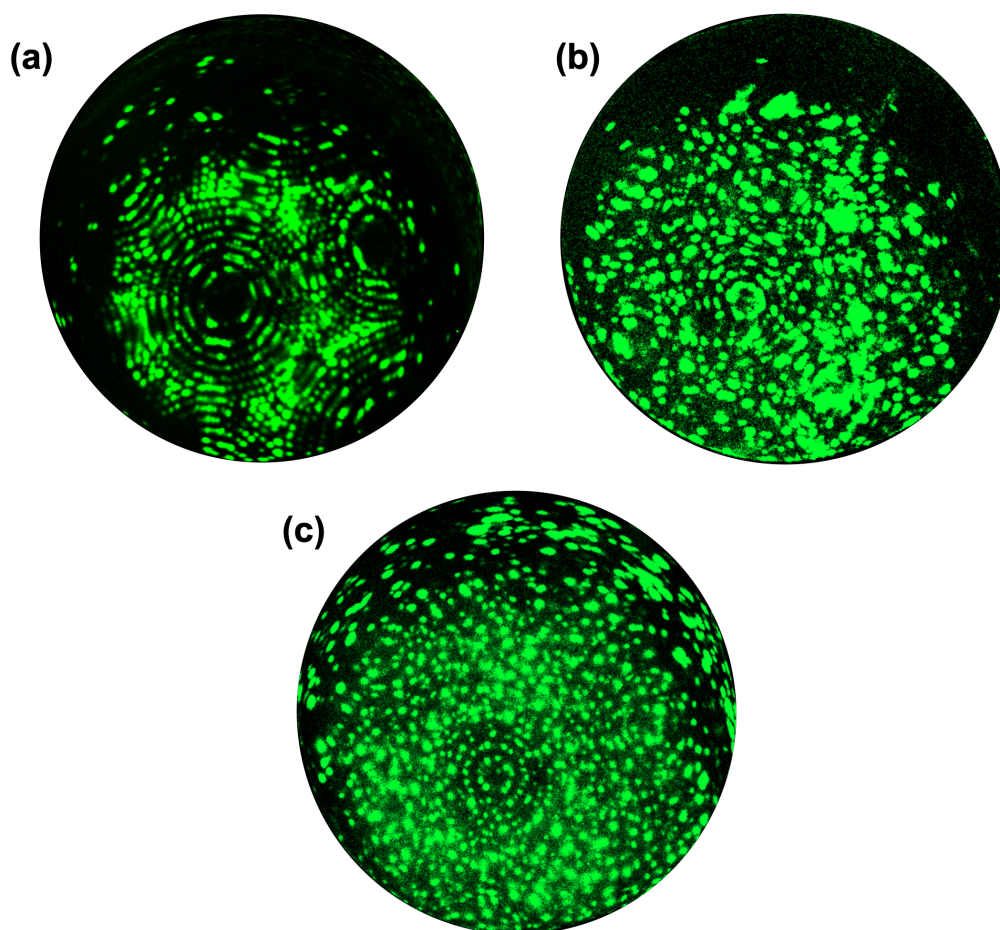
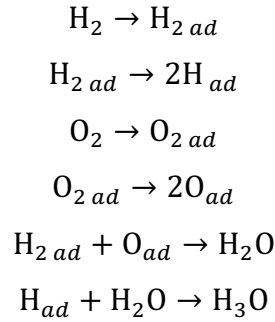


Figure 5.14 Field ion micrograph of the Pt surface, imaged under helium gas (10^{-5} Pa) at 60 K. (a) the fresh sample, (b) the surface after 1-round reaction, (c) the surface after 2-round reaction.

5.7 Conclusion

In conclusion, the author investigated the O₂ and residual H reaction on the Pt surface by FIM and AP. Three types of H species, H⁺, H₂⁺, and H₃⁺ on the Pt surface were observed in high vacuum (10⁻⁸ Pa). Upon exposing the nanoscale Pt metal surface to the O₂ atmosphere (10⁻⁵ Pa), H₂O was produced only at temperatures above 125 K. The speed of reaction accelerated as the temperature increased. Moreover, the planes surrounding the {111} planes were more active owing to their particular rough atomic corrugation. Accordingly, the process of hydrogen oxidation reaction can be summarized as:



The absence of static voltage and the thermal energy of laser pulse decreased the local concentration of residual H₂ gas on Pt surface, which declined the speed of the hydrogen oxidation reaction.

AP specimen surface was corroded by the hydrogen oxidation reaction. Pt was oxidized as the temperature increased. Various Pt-O complex ions could be detected, which in reverse promoted the hydrogen oxidation process.

FIM and surface AP proved to have the ability to *in-situ* observe catalytic surface reactions. The atomic-level surface structure obtained by FIM and chemical composition-related information obtained by AP allow us to study ongoing catalytic reactions with atomic lateral resolution.

5.8 Reference

1. F. Vurpillot, Thermal response of a field emitter subjected to ultra-fast laser illumination. *J. Phys. D: Appl. Phys.* **42**, 125502 (2009)
2. T. V. Bocarmé, T. D. Chau and N. Kruse, Imaging and probing catalytic surface reactions on the nanoscale: Field Ion Microscopy and atom-probe studies of O₂–H₂/Rh and NO–H₂/Pt. *Top. Catal.* **39**, 111–120(2006).
3. V. K. Medvedev, Y. Suchorski, C. Voss, T. V. Bocarmé, T. Bär and N. Kruse, Oxygen-induced reconstruction and surface oxidation of rhodium. *Langmuir* **14**, 6151–6157(1998).

CHAPTER 6 HYDROGEN OXIDATION REACTION ON W AND Pt/Pd ALLOY

In chapter 5, the hydrogen oxidation reaction on Pt surface was studied by AP. And several AP operation parameters (voltage/laser pulse, standing voltage and temperature) were also investigated.

In this section, the hydrogen oxidation reaction on Tungsten (W) and Platinum/Palladium (8/2 in weight ratio) alloy will be studied. The reason to choose W and PtPd alloy is that the PtPd alloy is usually regarded as more active catalyst than pure Pt metal, and reversely the W metal is rarely used as a catalyst. The reaction properties of PtPd alloy and W can be compared with that of Pt metal.

All AP experiments in this section were conducted in voltage pulse mode.

6.1 Reaction on Tungsten

6.1.1 FIM Image

An FIM image of a W tip prepared as described in the **section 2.2** was shown in Figure 6.1. The tip was imaged in helium at 60 K after cleaning the tip by cycles of evaporation.

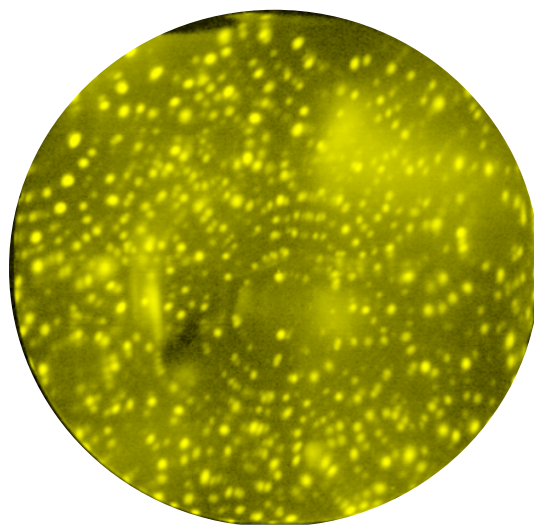
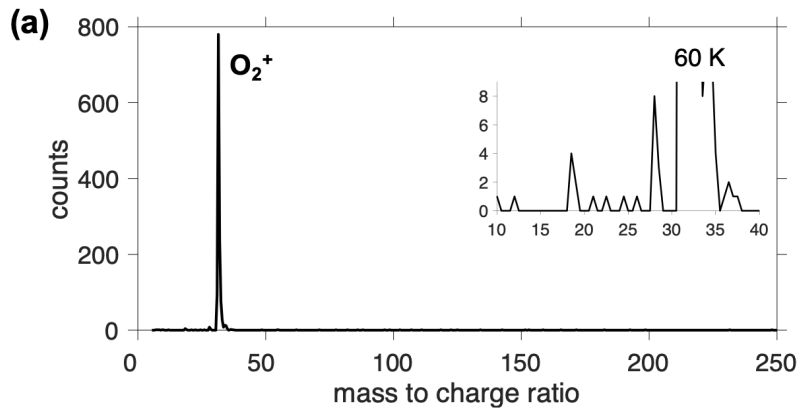


Figure 6.1 Field ion micrograph of the Pt surface, imaged under helium gas (10^{-5} Pa) at 60 K.

6.1.2 Temperature Effect

O₂ gas (10⁻⁵ Pa) was introduced to the main chamber to study the reaction of O₂ with residual H on the W surface. The chemical composition and distribution were recorded by AP at the temperature ranging from 60 K to room temperature. Five typical mass spectra, with m/n ranging from 10 to 250 were shown in Figure 6.2. At 60 K, the signal of O₂⁺ was solely detected on the W surface (Figure 6.2a). The background intensity of H₂O⁺ was shown in the inserted figure. When the temperature increased to 90 K, the WO₂⁵⁺ ions rather than O₂⁺ appeared as shown in Figure 6.2b, which inferred the W was oxidized even at a cryogenic temperature. Upon further increasing the temperature to 135 K, hydrogen oxidation reaction started to happen on W surface. The signal of H₃O⁺ and O⁺ signals emerged, suggesting the protonation of H₂O species and the dissociation of O₂, respectively. Besides, the O₂⁺, WO₃⁵⁺ and WO_xⁿ⁺ ions appeared in the mass spectrum, as shown in Figure 6.2c. When the temperature came to 158 K, WO₂⁴⁺ and WO₂³⁺ can be detected (Figure 6.2d). And the O₂H₅⁺ appeared in the mass spectrum. The intensity of the products, H₂O⁺ and H₃O⁺ increased significantly from 135 K to 158 K, compared with the intensity of reactant O₂⁺ ions. At the temperature of 240 K, not only H₃O⁺ and O⁺ but also WO₃⁺ were shown in the mass spectrum Figure 6.2e.



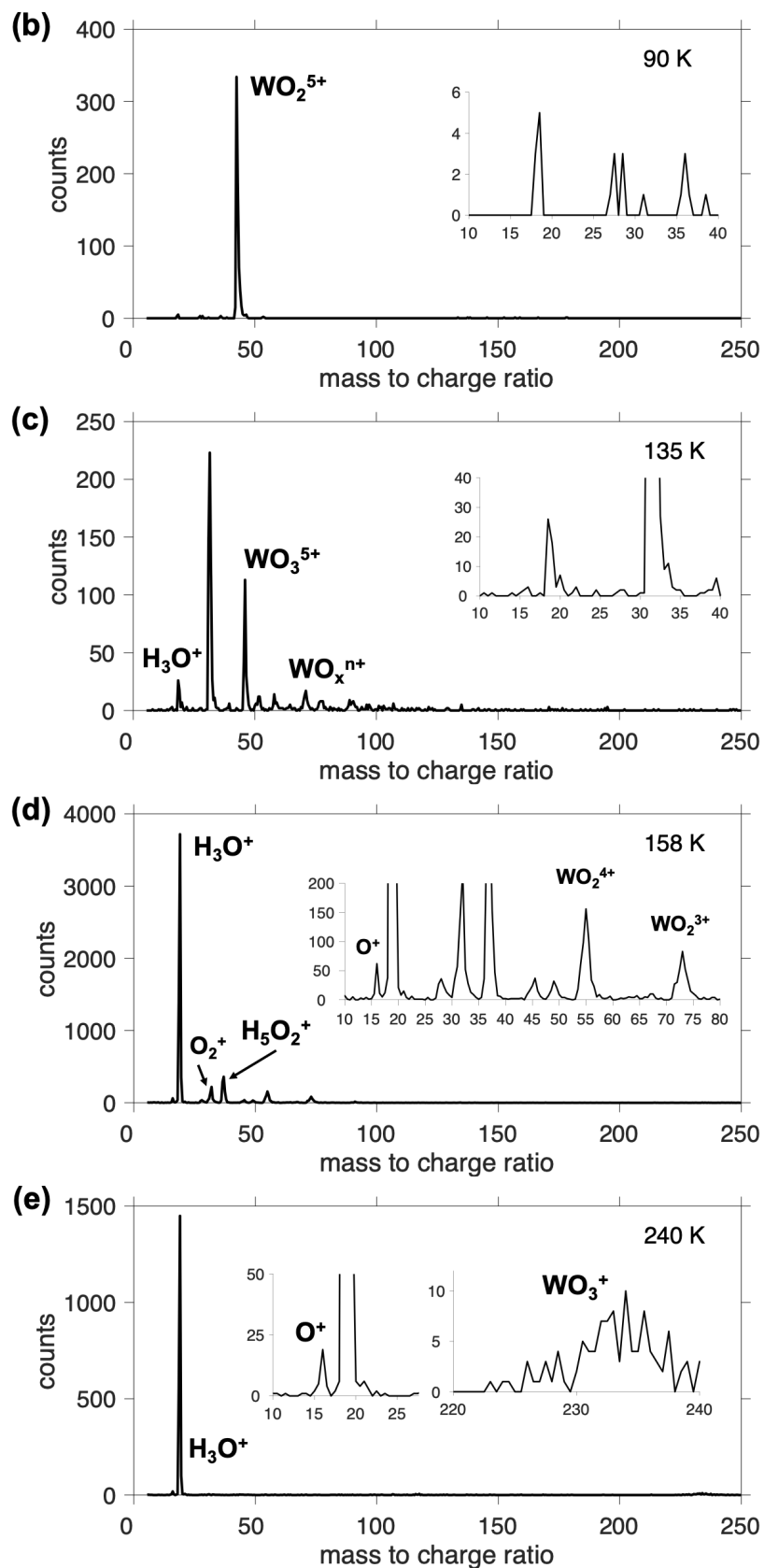


Figure 6.2 Mass Spectra of the interaction of O_2 (10^{-5} Pa) and H species on the W surface in different conditions: (a) 60 K, (b) 90 K, (c) 135 K, (d) 158 K and (e) 240 K in voltage pulse mode.

6.1.3 2D Mapping

Next, AP was conducted to analyse the chemical species distribution of H_3O^+ , O_2^+ and WO_3^{5+} ions on the W metal surface at 135 K (figure 6.3). The most active sites of H_3O^+ was overridden with that of WO_3^{5+} ions. The WO_3^{5+} ions indicated that the O_2 is dissociated and reacted with W, which inferred the oxidized W surface promoted the hydrogen oxidation reaction. As the temperature increased to 158 K, the chemical compositions and intensities on W were changed. As shown in Figure 6.4, the H_3O^+ ions resided on 4 areas which is similar to the distribution of O_2^+ ions. The O_2H_4^+ and WO_2^{3+} and WO_2^{4+} were more likely to be detected surrounding these 4 areas.

135 K

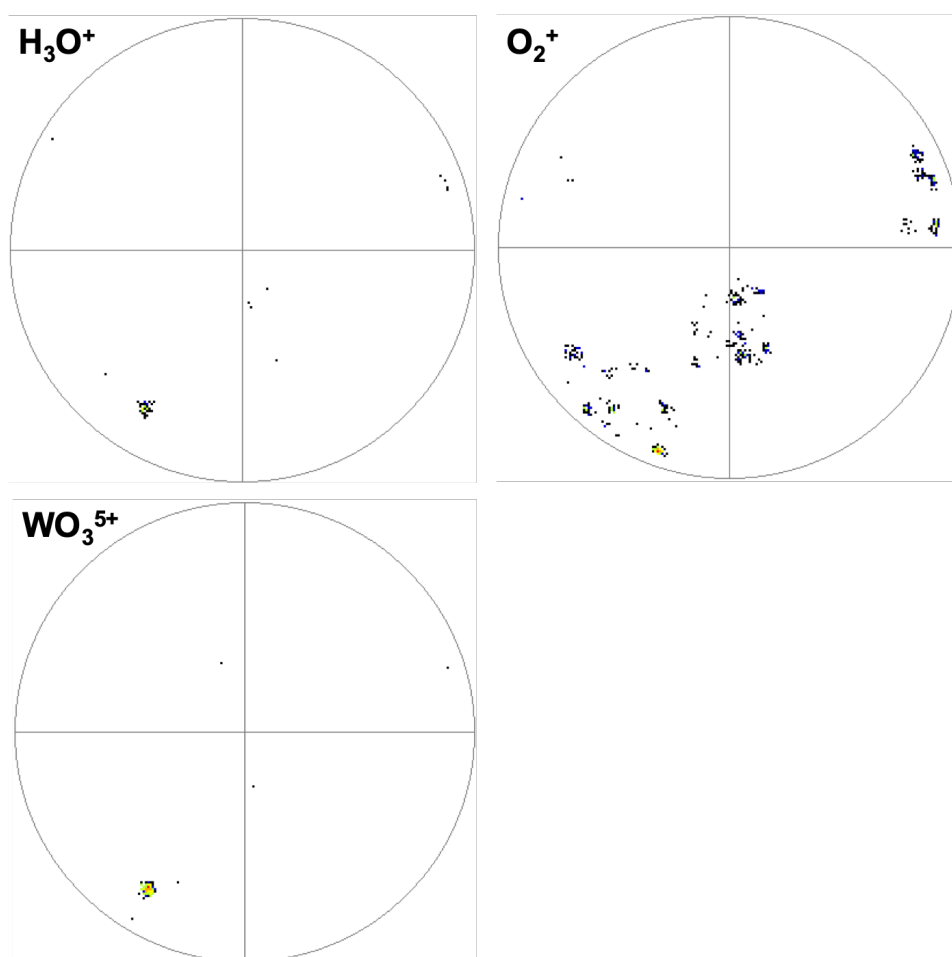


Figure 6.3 The 2D maps of H_2O^+ , H_3O^+ , WO_3^{5+} ions during the reaction between O_2 (10^{-5} Pa) and residual H on W surface at the temperature of 135 K. Black dot: 1 ion; blue dot: 2 ions; green dot: 2–5 ions; yellow dot: 5–10 ions; red dot: 20–50 ions.

158 K

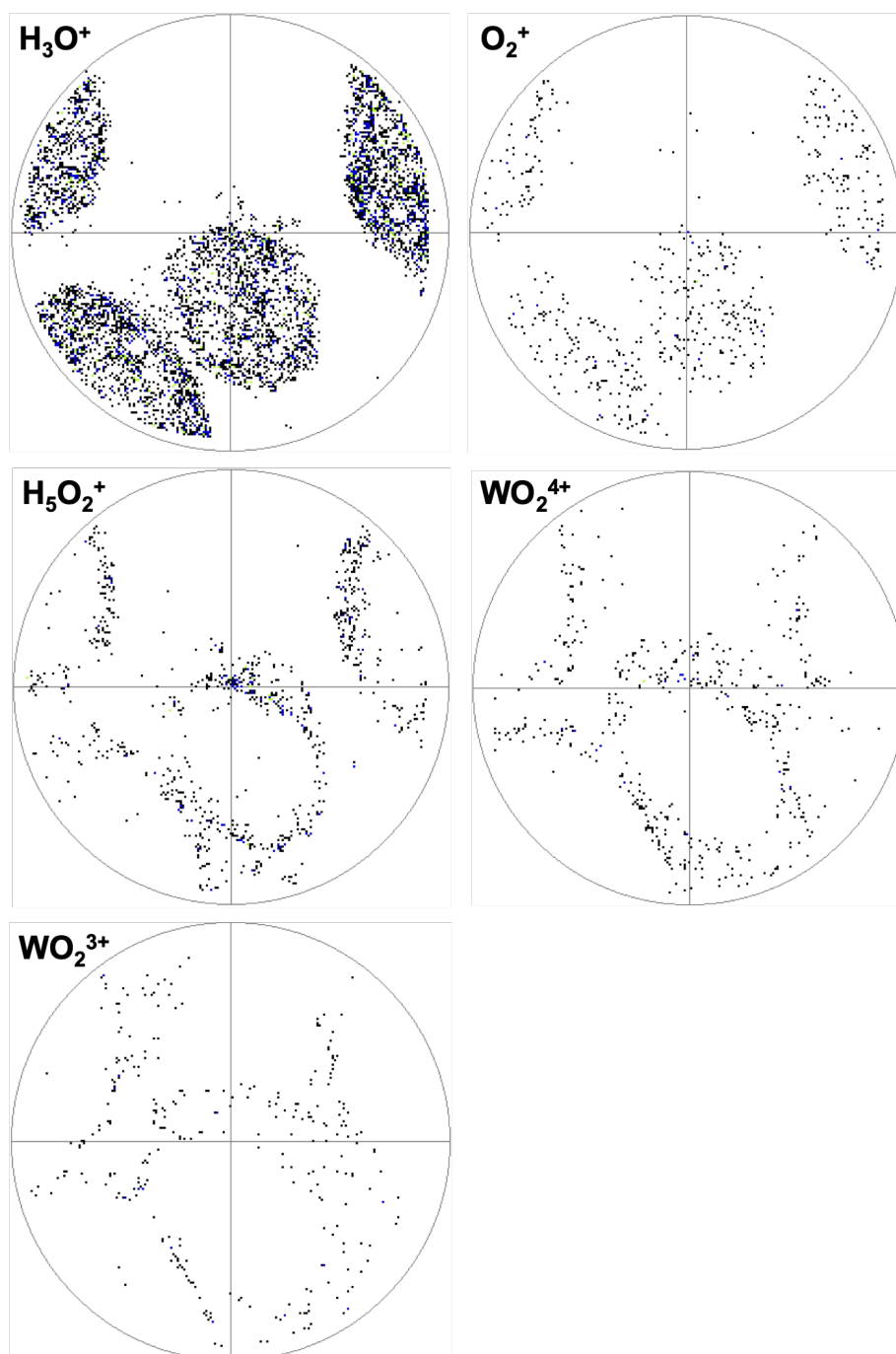


Figure 6.4 The 2D maps of H₂O⁺, H₃O⁺, O₂H₅⁺, WO₂⁴⁺ and WO₂³⁺ ions during the reaction between O₂ (10^{−5} Pa) and residual H on W surface at the temperature of 158 K. Black dot: 1 ion; blue dot: 2 ions; green dot: 2–5 ions; yellow dot: 5–10 ions; red dot: 20–50 ions.

6.2 Reaction on Platinum/Palladium Alloy

When it comes to PtPd specimen, the author failed to obtain a FIM image. In that, the crystal of PtPd alloy is not as perfect as a pure metal, and the field evaporation field of Pt (45 V nm^{-1}) and Pd (37 V nm^{-1}) is different. Argon and Neon gases were introduced into the main chamber as imaging gases, but no clear concentric rings were shown on the detector.

6.2.1 Temperature Effect

O_2 gas (10^{-5} Pa) was introduced to the main chamber to study the reaction of O_2 with residual H on the PtPd alloy surface. The chemical composition and distribution were recorded by AP at the temperature ranging from 60 K to room temperature. Four typical mass spectra, with m/n range from 10 to 100 were shown in Figure 6.5. At 60 K, the signal of O_2^+ was solely detected on the PtPd alloy surface (Figure 6.5a). When the temperature increased to 106 K, the H_2O^+ started to appear in the mass spectrum, suggesting the formation of products of hydrogen oxidation reaction. Besides, the PdO_2^{3+} and O_2^+ ions also showed at the temperature of 106 K, and the intensity of PdO_2^{3+} is larger than that of O_2^+ ions, which inferred a chemical bond between Pd and O_2 . In addition, the Pd metal was more easily oxidized than Pt at a cryogenic temperature. Upon further increasing the temperature to 130 K, the H_3O^+ and PdO^{4+} ions emerged as shown in Figure 6.5c. The appearance of PdO^{4+} indicated the dissociated O on Pd surface, and the dissociated O tightly bonded to Pd surface resulting into the evaporation of Pd metal.

When the temperature came to 140 K, the intensity of H_3O^+ , H_2O^+ and O_2H_5^+ ions increased, suggesting that the speed of the hydrogen oxidation reaction was accelerated by the increasing temperature (Figure 6.5d).

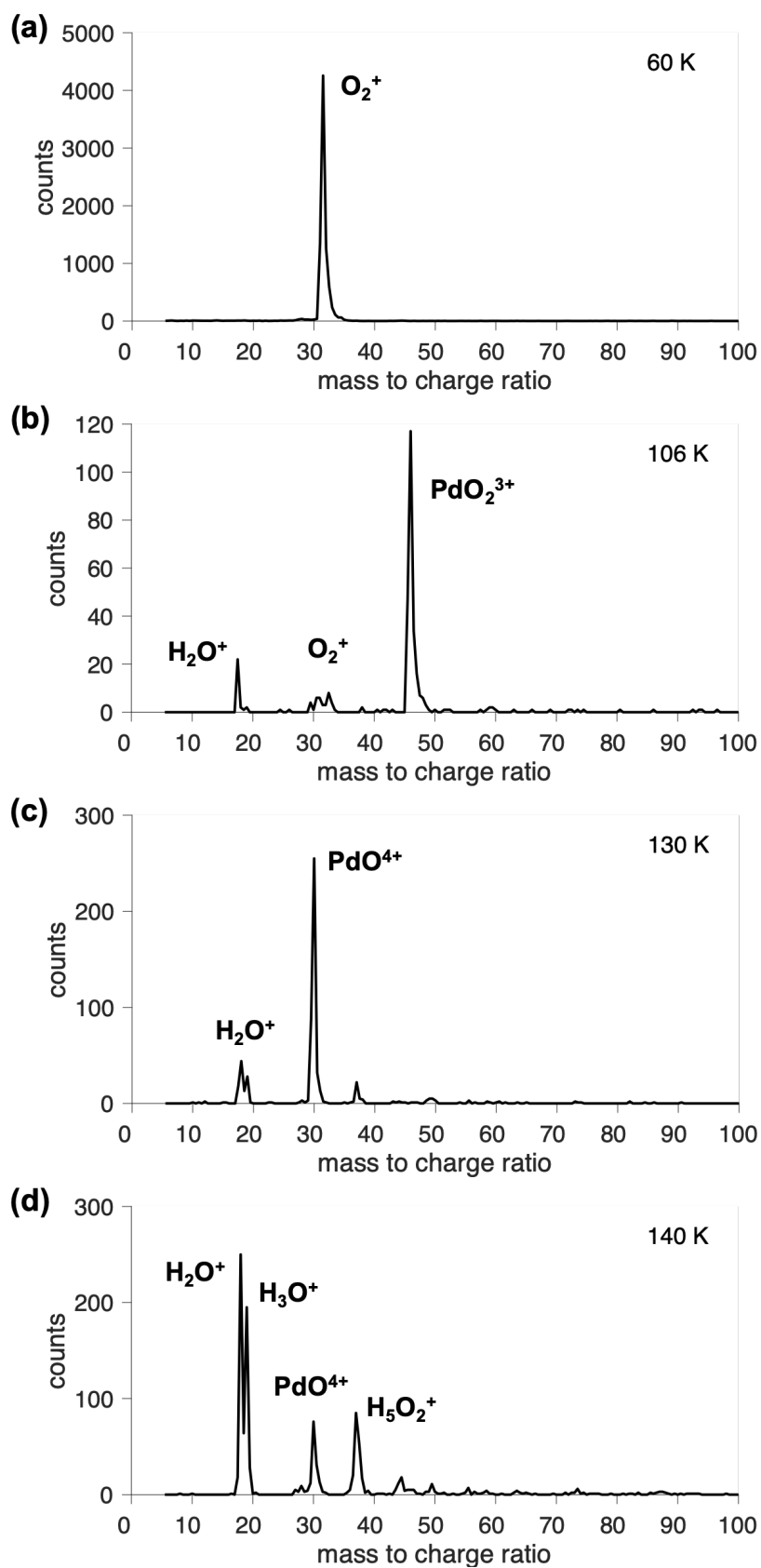


Figure 6.5 Mass Spectra of the interaction of O_2 (10^{-5} Pa) and H species on the PtPd alloy surface in different temperatures: (a) 60 K, (b) 106 K, (c) 130 K and (d) 140 K in voltage pulse mode.

6.2.2 2D Mapping

As for the 2D mapping of the chemical compositions on PtPd surface, all the ions in a typical mass spectrum of Figure 6.5d were chosen to be studied. As shown in Figure 6.6, the H_3O^+ , $\text{H}_3\text{O}^+ \text{PdO}^{4+}$ and H_5O_2^+ ions almost shared a same distribution, indicating the reaction was more easily to take place at the oxidized place.

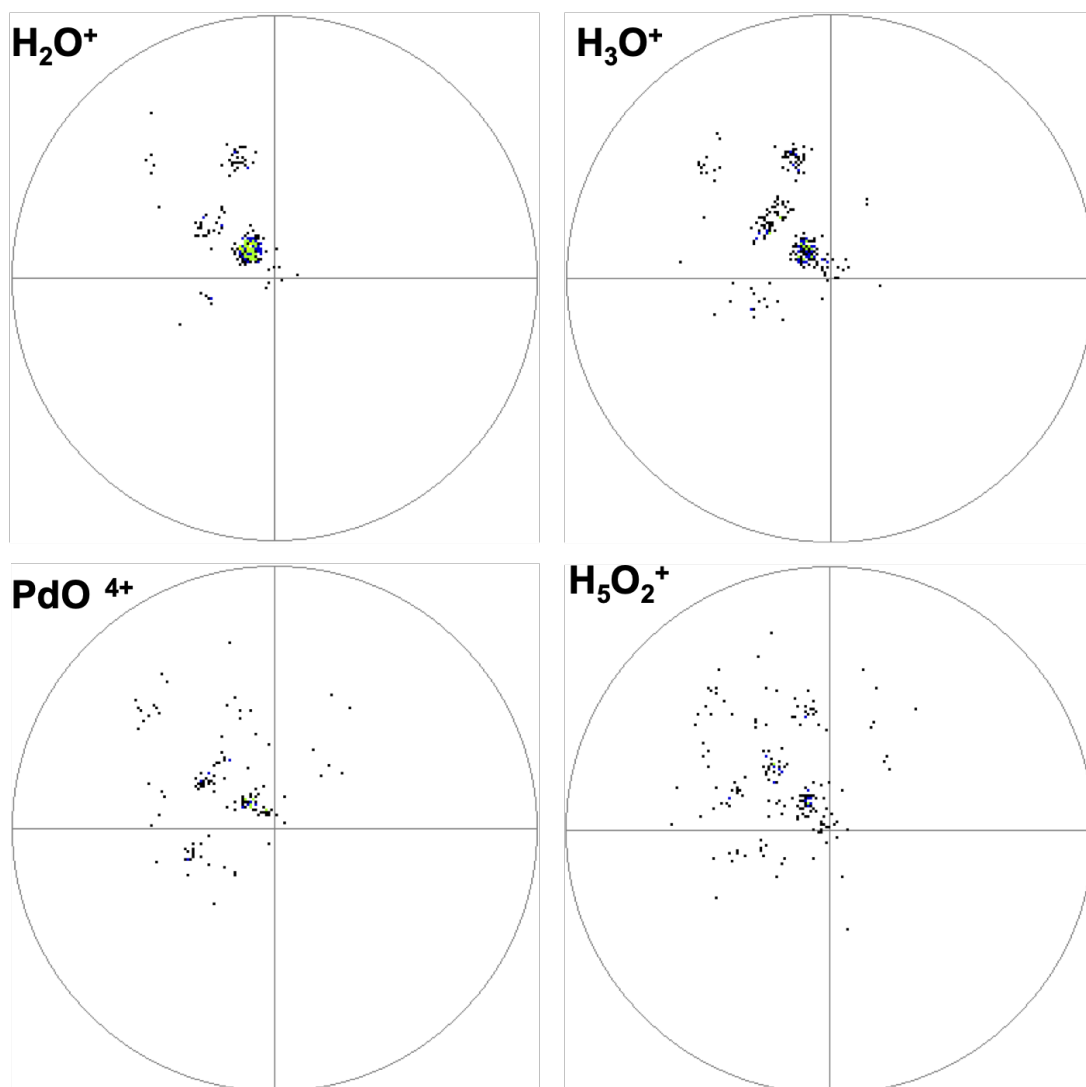


Figure 6.6 The 2D maps of H_2O^+ , H_3O^+ , O_2H_5^+ , PdO^{4+} ions during the reaction between O_2 (10^{-5} Pa) and residual H on PtPd alloy surface at the temperature of 140 K. Black dot: 1 ion; blue dot: 2 ions; green dot: 2–5 ions.

6.3 Conclusion

In conclusion, the author investigated the O₂ and residual H reaction on the W metal and PtPd alloy surface by FIM and AP. Upon exposing the nanoscale W metal and PtPd alloy surface to the O₂ atmosphere (10⁻⁵ Pa), the lowest temperatures to trigger hydrogen oxidation reaction on PtPd and W surface were 106 K and 135 K, respectively. As shown in Figure 6.7, comparing to 125 K of Pt metal, the PtPd was proved to be more active for hydrogen oxidation reaction and W was less active.

The oxidation of PtPd and W surface was also be observed, the oxidized metal can promote the hydrogen oxidation reaction [1,2].

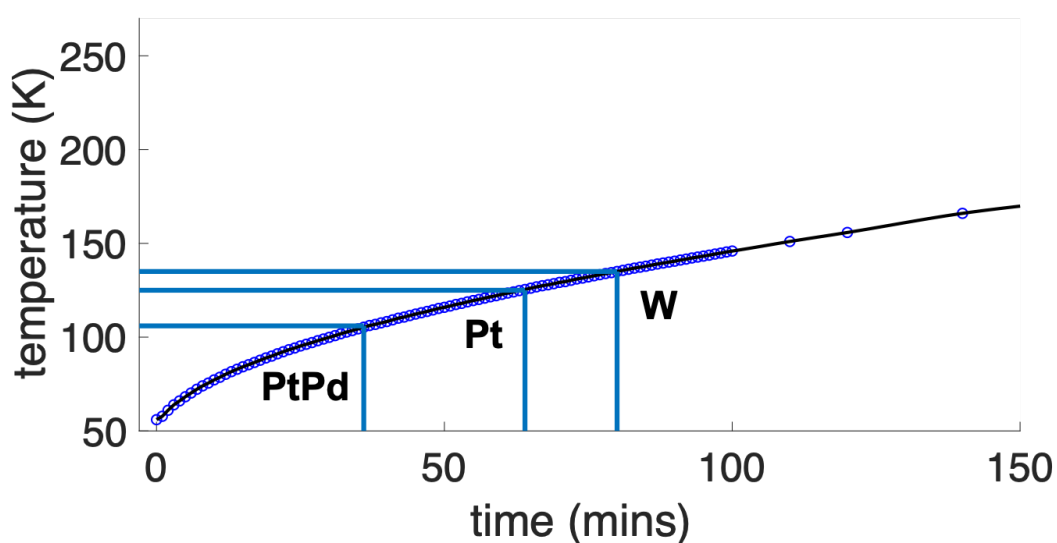


Figure 6.7 The temperatures of hydrogen oxidation reaction taking place on PtPd (106 K), Pt (125 K) and W (135 K) surface.

6.4 Reference

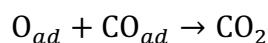
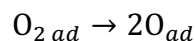
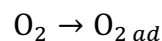
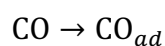
1. T. V. Bocarmé, T. D. Chau and N. Kruse, Imaging and probing catalytic surface reactions on the nanoscale: Field Ion Microscopy and atom-probe studies of $\text{O}_2\text{-H}_2/\text{Rh}$ and $\text{NO-H}_2/\text{Pt}$. *Top. Catal.* **39**, 111–120(2006).
2. V. K. Medvedev, Y. Suchorski, C. Voss, T. V. Bocarmé, T. Bär and N. Kruse, Oxygen-induced reconstruction and surface oxidation of rhodium. *Langmuir* **14**, 6151–6157(1998).

CHAPTER 7 CARBON MONOXIDE OXIDATION REACTION ON Pt SURFACE

In this chapter, the CO oxidation reaction on Pt surface at the temperatures from 60 K to 300 K was explored by AP. Compared to the hydrogen oxidation reaction (in chapter 5 and 6), in which only O₂ gas was introduced into chamber to react with residual hydrogen, two kinds of gases, carbon monoxide (CO) and O₂, were introduced into the main chamber together. Consequently, the experimental parameters became complicated.

Some previous studies of CO oxidation on Pt surface by FIM have been clarified in **section 1.2.2** of chapter 1. Some key points can be summarised:

1. When CO and O₂ gases coexist, they competitively adsorb on Pt surface. In general, CO preferentially adsorbs on Pt sites.
2. The oxidized Pt surface has the reactivity to trigger CO oxidation reaction.
3. With a proper pressure ratio of CO to O₂, two gases would adsorb on Pt by turns. And the intensity of CO₂ would show a periodic wave, which is CO-oxidation oscillating.
4. All the previous studies about CO oxidation reaction by FIM is implemented above room temperature.
5. In general, the CO oxidation reaction obeys Langmuir-Hinshelwood rule as:



The CO and O₂ adsorb on Pt surface and the dissociated O can oxidize CO into CO₂ [1–5].

Therefore, to study CO oxidation reaction on Pt, a proper pressure condition, CO adsorption behaviours, CO oxidation temperature, and CO oxidation active sites are essential problems to be solved. In this chapter, the author put the emphasis on the first two problems, and the rest problems will be studied by other AP group members in our Lab.

7.1 CO Adsorption on Pt Surface

CO gas (10^{-5} Pa) was introduced to the main chamber with Pt sample cool down to 60 K. the pressure of CO was hold for one hour, for a sufficient contact of CO with Pt surface. During this time, only one peak, with m/n of 28, can be detected. Then stop the supply of CO, and increase the temperature of Pt by turning off the cryogenerator. The pressure of main chamber decreased to background level (10^{-8} Pa).

As the Pt temperature raised, various peaks appeared in the mass spectra. As shown in figure 7.1, CO-related and H₂O-related chemical species were detected. The appearance of H₂O-related attributed to some residual water in the main chamber. According to their small intensity, the existence of water has a negligible influence on CO adsorption.

The intensity of CO-related peaks was larger than that of H₂O-related species. At 60 K, a great quantity of CO gas could still bind to Pt surface even under 10^{-8} Pa. As temperature increased, a weak physical bond developed into to a strong chemical bond, which can be proved by $\text{Pt}(\text{CO})_2^{3+}$ ions in the mass spectrum. In addition, CO gas accumulated on Pt surface according to the existence of the $(\text{CO})_2$ and $(\text{CO})_3$ species. Besides, CO cannot dissociate on Pt surface because no PtO or PtC ions appeared in the mass spectrum, which is different from the interaction between O₂ and Pt surface.

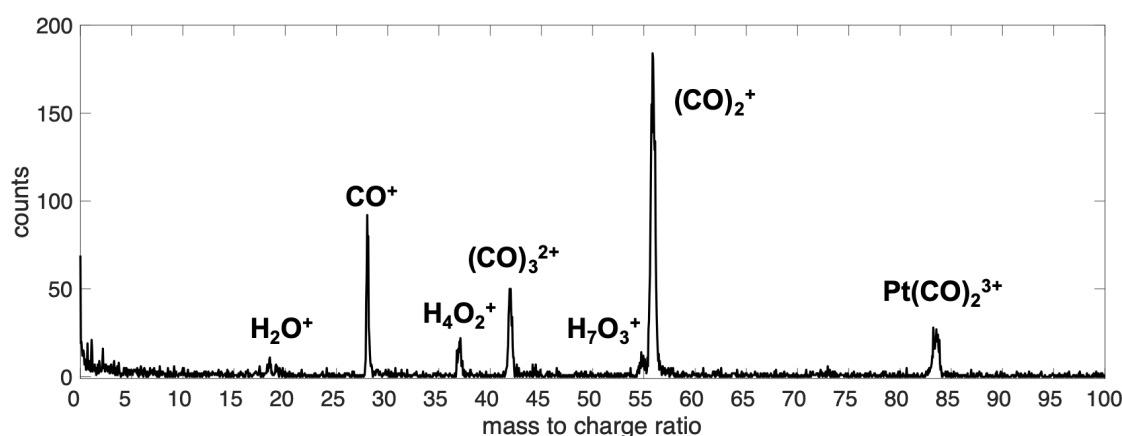


Figure 7.1 Mass Spectrum of CO adsorption on the Pt surface.

Chemical species distribution on Pt surface were displayed in figure 7.2. The distribution patterns of CO-related ions are similar, and the intensity of CO was extremely large on some spots as shown in red colour.

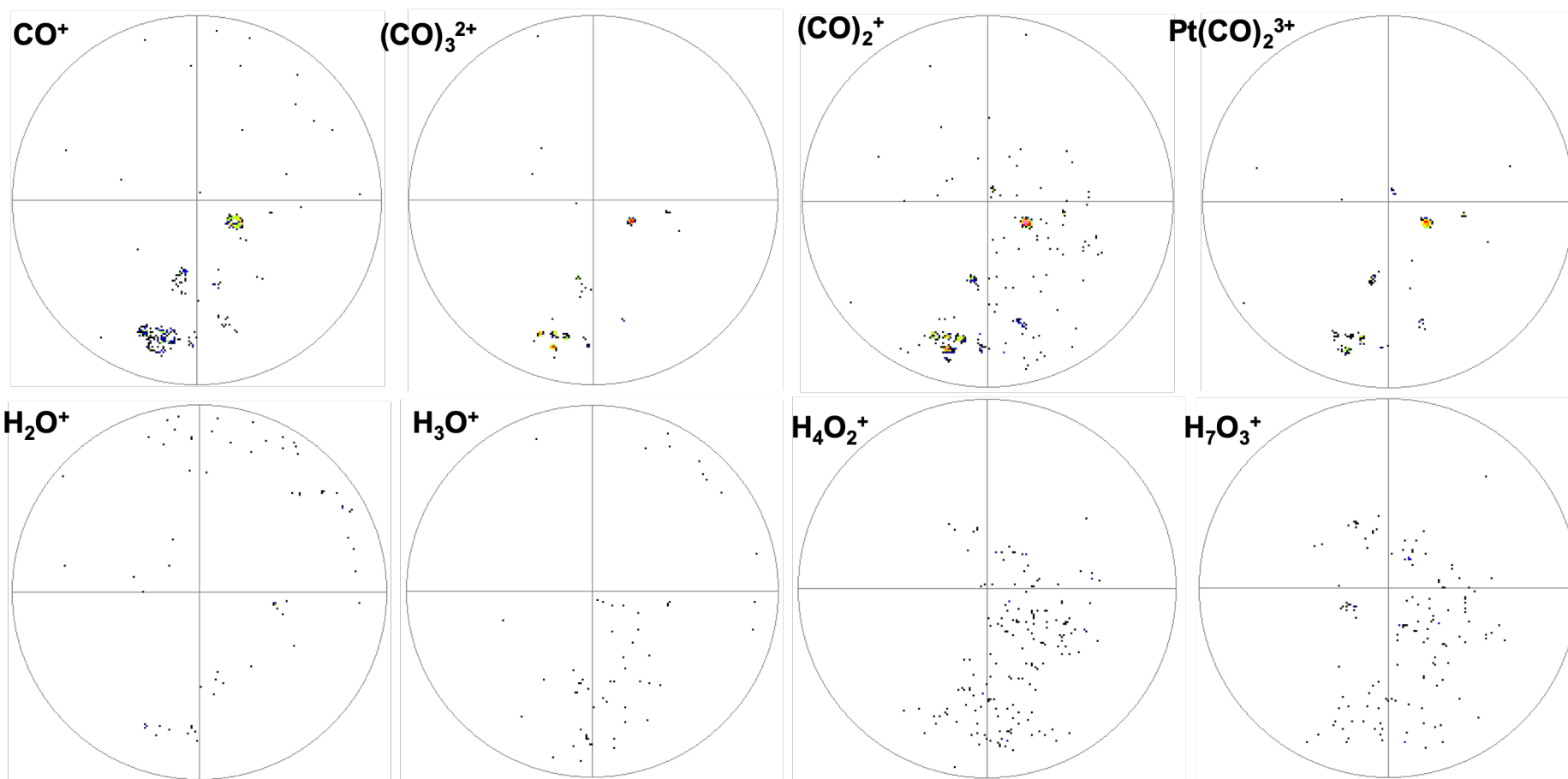


Figure 7.2 The 2D maps of CO^+ , $(\text{CO})_3^{2+}$, $(\text{CO})_2^+$, $\text{Pt}(\text{CO})_2^{3+}$, H_2O^+ , H_3O^+ , $\text{H}_4\text{O}_2^{5+}$, $\text{H}_7\text{O}_3^{5+}$ ions on Pt surface. Black dot: 1 ion; blue dot: 2 ions; green dot: 2–5 ions; yellow dot: 5–10 ions; red dot: 20–50 ions.

7.2 Pressure Ratio of O₂ to CO

As we know, the O₂ adsorbed or oxidized Pt surface can trigger CO oxidation. And CO preferentially adsorbs on Pt sites compared to O₂. Therefore, to achieve CO oxidation, an optimal pressure ratio of CO to O₂ is a critical parameter.

When the pressure of CO and O₂ both kept around 1×10^{-5} Pa, only the CO⁺ peak, with m/n of 28, appeared in the mass spectrum (figure 7.3a). Then gradually decrease the pressure of CO, the peak, with m/n of 32 starting to show in as the pressure of O₂ was 10 times larger than that of CO (figure 7.3b). At this point, the O₂ had the chance to adsorb on Pt surface. Therefore, an optimal pressure ratio of CO to O₂ is about 10, which is consistent with the result of V.V. Gorodetskii [2].

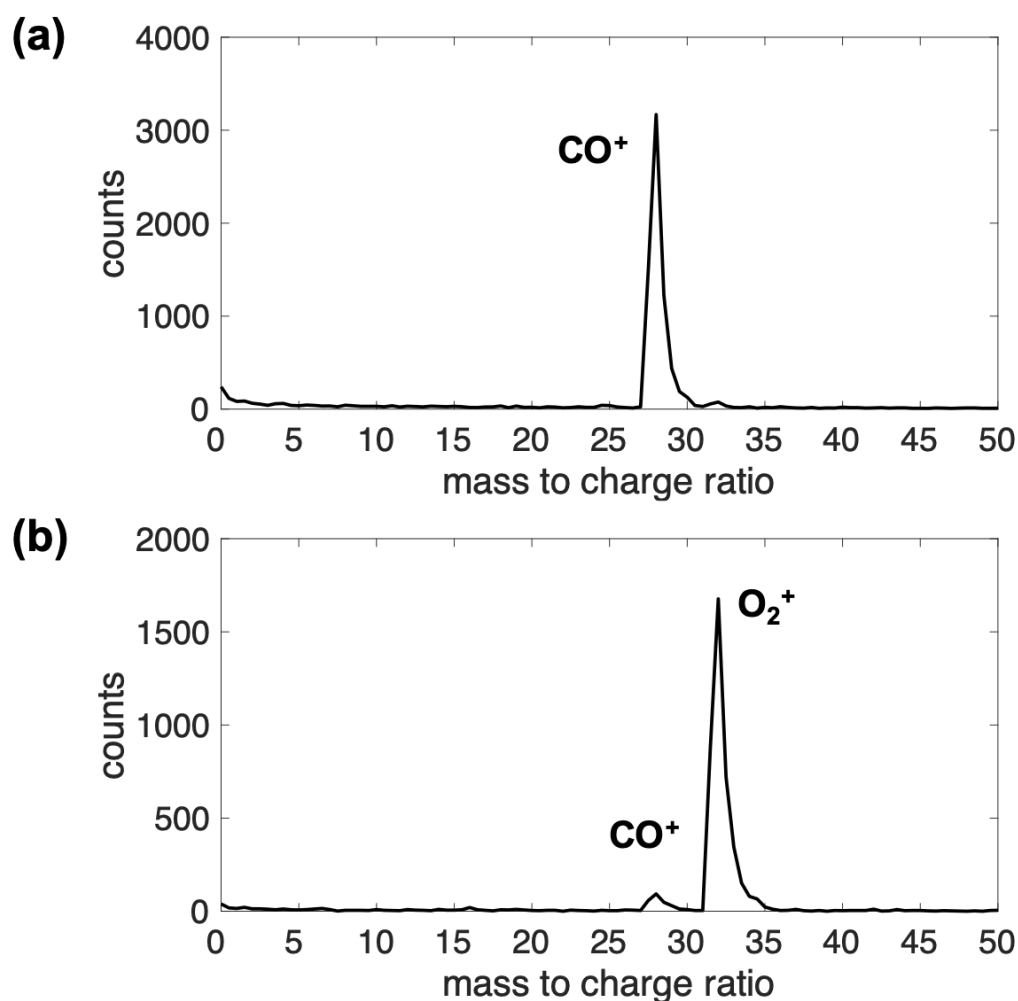


Figure 7.3 Mass Spectra of O₂ and CO on Pt surface. (a) pressure of O₂: 1×10^{-5} Pa and pressure of CO: 1×10^{-5} Pa; (b) pressure of O₂: 1×10^{-5} Pa and pressure of CO: 1×10^{-6} Pa.

7.3 Conclusion

At 60 K, a great quantity of CO gas could adsorb on Pt surface. As temperature increased, a weak physical bond developed into to a strong chemical bond, as $\text{Pt}(\text{CO})_2^{3+}$ ions appeared. CO cannot dissociate on Pt surface at the temperature from 60 K to 300 K. A proper pressure ratio of O_2 to CO gases was about 10, in which the O_2 had the chance to adsorb on Pt surface.

7.4 Reference

1. V.V. Gorodetskii and B. E. Nieuwenhuys, W. M. H. Sachtler and G. K. Boreskov, Adsorption of oxygen and its reactions with carbon monoxide and hydrogen on rhodium surfaces: comparison with platinum and iridium. *Surf. Sci.* **7**, 355–371 (1981).
2. V.V. Gorodetskii, V.I. Elokhin, J.W. Bakker, B.E. Nieuwenhuys, Field electron and field ion microscopy studies of chemical wave propagation in oscillatory reactions on platinum group metals. *Catal. Today* **105**, 183–205 (2005).
3. V. Gorodetskii, W. Drachsel and J.H. Block, Imaging the oscillating CO-oxidation on Pt-surfaces with field ion microscopy. *Catal. Lett.* **19**, 223–231 (1993).
4. V.V. Gorodetskii, W. Drachsel, Kinetic oscillations and surface waves in catalytic $\text{CO}+\text{O}_2$ reaction on Pt surface field electron microscope, field ion microscope and high resolution electron energy loss studies. *Appl. Catal. A-Gen.* **188**, 267–275(1999).
5. V.V. Gorodetskii, A.V. Matveev, E.A. Podgornov, and F. Zaera, Study of the low-temperature reaction between CO and O_2 over Pd and Pt surfaces. *Top. Catal.* **32**, 17–28 (2005).

CHAPTER 8 CONCLUSION AND PERSPECTIVE

APM is the only material analysis technique providing 2D and 3D mapping of chemical composition and structure at the atomic scale, which offers a compelling and unique insights into the way material behaves. The emphasis of this research focuses on *in-situ* observation of surface reaction at an atomic level by APM, which can be regarded as a new function and application of APM. Specifically, the FIM image can identify the surface morphology before reaction conducted on sample surface. Then introduce reactant gases into the chamber and make the reaction take place on the specimen surface by changing the specimen temperature. The variation of the chemical composition distribution on specimen surface can be recorded by AP.

To achieve this goal, a proper and simple reaction, hydrogen oxidation reaction catalyzed by Pt, was chosen as a tentative model on the first try in AP analysis. The reaction surface is subjected to a high electric field and the pressure of reactant gas should be kept in vacuum condition, which is different from the real reaction conditions. Therefore, the influence of the EF variation over specimen surface on active site identification was explored. Besides, the effects of the laser/voltage pulse, the surface corrosion caused by the reaction etc. were investigated.

To evaluate the EF effects on active sites identification, the author developed an approach to experimentally calculate the EF distribution on a nano-sized sample surface. The sample apex was located by comparing the ion intensity of the FIM image. Next, contour maps of normalized H^+ ion intensity with various EF_{max} were used to calculate the relative EF with respect to the emitting angle (figure 8.1 a and c). This fast and non-destructive method could determine the appropriate EF for accurate AP analysis. In addition, after sufficient field evaporation, the specimen emitter evolves to be an EF-constant surface except the outer boundary, in which the emitter develops into an equilibrium end shape (figure 8.1 b and d). As a result, the ion intensity of the 2D mapping of such flat surface can exactly reflect the real distribution of the chemical composition on the emitter.

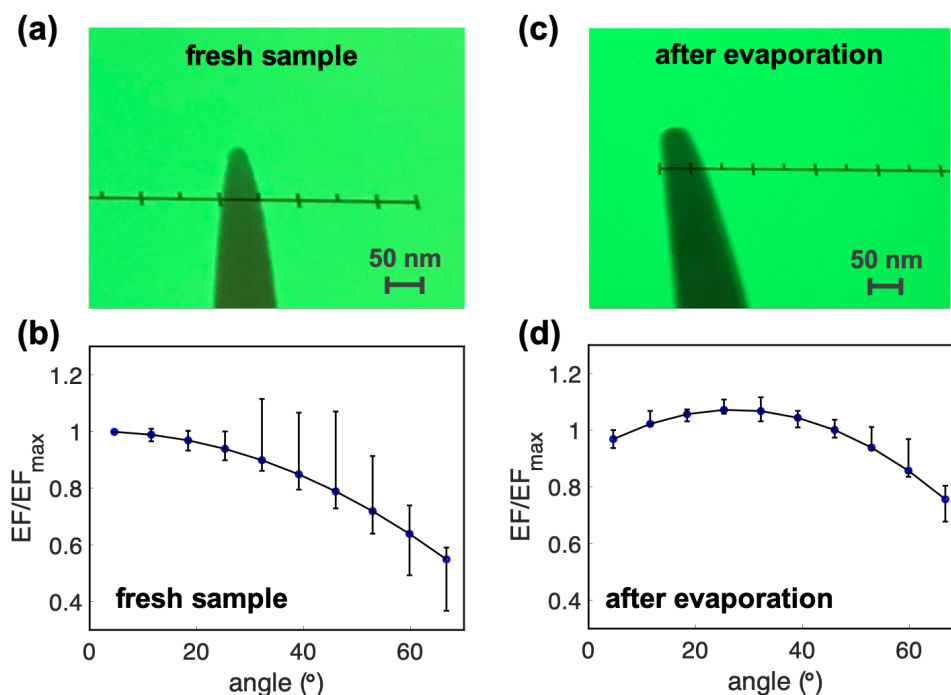


Figure 8.1 TEM images of the sample surface for a fresh sample (a) and an evaporated sample (c). The change in the relative EF with respect to emitting angle, θ of a fresh sample (b) and an evaporated sample (d).

The residual hydrogen in ultra-high vacuum on Pt surface was systematically investigated by AP analyses in chapter 4. Three hydrogen species, H^+ , H_2^+ , and H_3^+ ions, can be detected on Pt surface with a background pressure of 2×10^{-8} Pa. H^+ ions are more likely to be detected at high electric field. On the contrary, the H_2^+ and H_3^+ ions appeared at relatively low electric field. In isotope labelling experiments using D_2 under two kinds of pressure conditions (2×10^{-6} Pa and 2×10^{-8} Pa), the variation of D^+/D_2^+ and H^+/H_2^+ showed a similar pattern with respect to electric field, which revealed that the residual hydrogen is from H_2 gas in the chamber. Calculation of field-induced binding energy of H_2 gas with surface suggested a considerable improvement of the H_2 gas concentration on the sample surface upon applying high electric field. The accumulated H_2 gas on Pt sample surface can be regarded as the reactant gas in future research.

The O_2 and residual H reaction on the Pt surface was investigated by FIM and AP in chapter 5. Upon exposing the nanoscale Pt metal surface to the O_2 atmosphere (10^{-5} Pa), the residual H_2 can be oxidized at temperatures above 125 K. The products were H_2O and H_3O . Moreover, the author found that the planes surrounding the $\{111\}$ planes were more active owing to their particular rough atomic corrugation (figure 8.2).

The absence of static voltage and the thermal power of laser pulse decreased the local concentration of residual H_2 gas on Pt surface, which decreased the rate of the hydrogen oxidation reaction.

AP specimen surface was corroded by the hydrogen oxidation reaction. Pt was oxidized as the temperature increased. Various Pt-O complex ions could be detected, which in reverse promoted the hydrogen oxidation process.

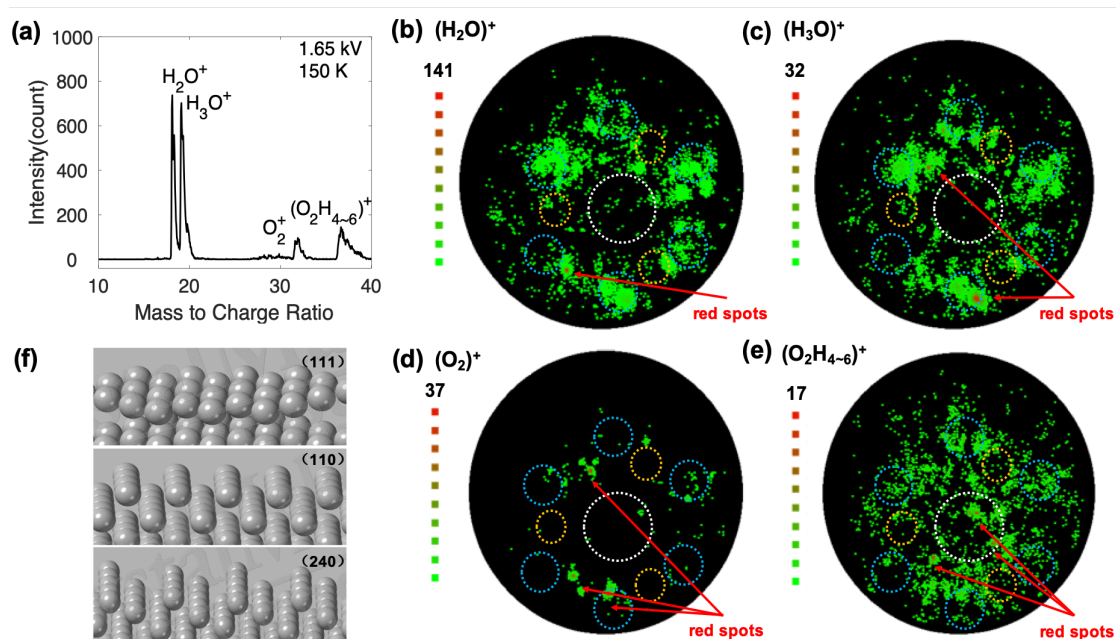


Figure 8.2 (a) Mass spectrum of the reaction between O_2 (10^{-5} Pa) and H_2 on the Pt surface at 150 K. 2D distribution images of (b) H_2O^+ , (c) H_3O^+ , (d) O_2^+ and (e) $O_2H_{4-6}^+$. (f) Surface corrugation of the Pt (111) surface. The white dash ring, blue dash rings and orange dash rings represent the $\{111\}$, $\{240\}$ and $\{113\}$ planes, respectively. (f) Surface corrugation of the Pt (111), (110) and (240) planes.

In chapter 6, the author investigated the O₂ and residual H reaction on the W metal and PtPd alloy surface. Upon exposing the nanoscale W metal and PtPd alloy surface to the O₂ atmosphere (10⁻⁵ Pa), it was found that the lowest temperatures to trigger hydrogen oxidation reaction on PtPd and W surface was 106 K and 135 K, respectively. As shown in figure 8.3, comparing to 125 K of Pt metal, the PtPd was proved to be more active for hydrogen oxidation reaction and W was less active. The oxidation of PtPd and W surface was also observed, which can promote the hydrogen oxidation reaction.

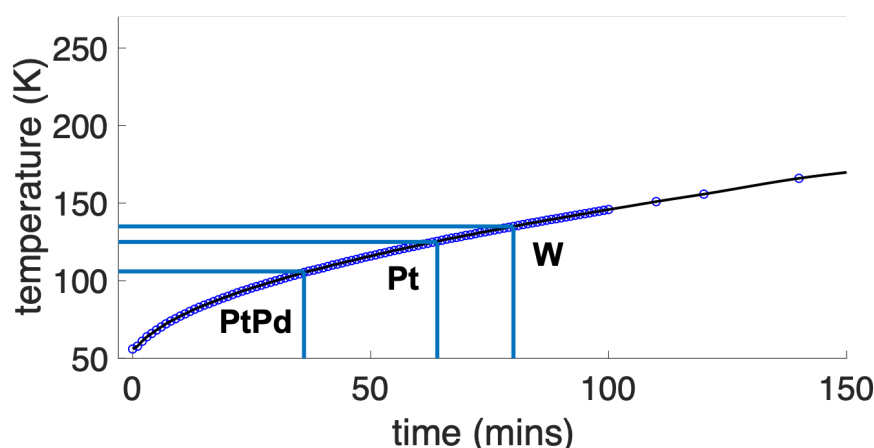


Figure 8.3 The temperatures of hydrogen oxidation reaction taking place on PtPd (106 K), Pt (125 K) and W (135 K) surface.

In chapter 7, some tentative works were conducted to explore CO oxidation on Pt surface by AP. At 60 K, a great quantity of CO gas was adsorbed on Pt surface. As temperature increased, the weak physical bond developed into the strong chemical bond, evidenced by the observation of Pt(CO)₂³⁺ ions. CO will not dissociate on Pt surface at the temperature from 60 K to 300 K. A proper pressure ratio of O₂ to CO gases was about 10, in which the O₂ had the chance to adsorb on Pt surface.

In conclusion, a new surface analysis method combined with FIM and AP has been successfully developed to *in-situ* observe catalytic surface reactions for the first time. The atomic-level surface structure obtained by FIM and chemical composition-related information obtained by AP allow us to study on-going catalytic reactions with atomic lateral resolution.

This surface analysis method may pave an avenue for exploring the heterogenous reaction with a nanometric lateral resolution. The experiment data lead to a new insight

for surface reaction mechanism and theory, which partially narrow the gap between surface analysis approaches and catalysis/reaction.

In spite of this initial achievement, APM ought to challenge more complicated heterogeneous reaction for a vast application prospect. Additionally, some inevitable problems cannot be ignored. The reaction can only be investigated in vacuum condition, which is a niche area for all surface analysis techniques. And high temperature will decrease the mass and spatial resolution. Other characterization methods can be invented for cross-references to investigate a reaction with comprehensive perspectives.

APPENDICES

Appendix A

Image Hump Model Prediction

Element	Λ	I_1	I_2	I_3	Φ	F_1	F_2	F_3
Li	1.650	5.392	76.368	122.451	2.50	14	520	1000
Be	3.330	9.322	18.211	153.893	3.90	53	46	770
B	5.920	8.300	25.150	37.900	4.60	64	79	103
C	7.400	11.260	24.380	47.890	4.34	142	103	155
Na	1.130	5.139	47.286	71.640	2.30	11	210	360
Mg	1.530	7.646	15.035	80.143	3.70	21	25	220
Al	3.340	5.986	18.828	28.447	4.10	19	35	50
Si	4.670	8.150	16.340	33.490	4.80	45	33	60
K	0.941	4.340	31.630	45.720	2.20	7	87	150
Ca	1.825	6.113	11.871	50.910	2.70	19	18	100
Ti	4.855	6.820	13.580	27.490	4.00	41	26	43
V	5.300	6.740	14.650	29.310	4.10	44	30	49
Cr	4.100	6.766	16.500	30.960	4.60	27	29	51
Mn	2.980	7.435	15.640	33.670	3.80	30	30	60
Fe	4.290	7.900	16.160	30.650	4.40	42	33	54
Co	4.387	7.860	17.060	33.500	4.40	43	37	63
Ni	4.435	7.635	18.168	35.170	5.00	35	36	65
Cu	3.500	7.726	20.292	36.830	4.60	30	43	77
Zn	1.350	9.394	17.964	39.720	3.80	33	39	84
Ga	2.780	5.999	20.510	30.710	4.10	15	39	56
Ge	3.980	7.880	15.930	34.220	4.80	35	29	58
As	3.000	9.810	18.633	28.351	4.70	46	42	54
Rb	0.858	4.177	27.280	40.000	2.10	6	69	110
Y	4.400	6.380	12.240	20.500	3.10	40	24	–
Zr	6.316	6.840	13.130	22.990	4.20	56	28	35

Nb	7.470	6.880	14.320	25.040	4.00	74	37	45
Mo	6.810	7.100	16.150	27.160	4.20	65	41	51
Ru	6.615	7.370	16.760	28.470	4.50	62	41	54
Rh	5.752	7.460	18.080	31.060	4.80	49	41	59
Pd	3.936	8.340	19.430	32.920	5.00	37	41	63
Ag	2.960	7.576	21.490	34.830	4.60	24	45	72
Cd	1.160	8.993	16.908	37.480	4.10	25	31	70
In	2.600	5.786	18.869	28.030	4.10	12	31	46
Sn	3.120	7.344	14.632	30.502	4.40	26	23	46
Sb	2.700	8.641	16.530	25.300	4.60	32	30	40
Cs	0.827	3.894	25.100	35.000	2.10	5	55	85
Ba	1.860	5.212	10.004	–	2.50	15	13	–
La	4.491	5.577	11.060	19.175	3.30	32	18	24
Hf	6.350	7.000	14.900	23.300	3.50	67	39	43
Ta	8.089	7.890	16.000	22.000	4.20	96	48	44
W	8.660	7.980	18.000	24.000	4.50	102	57	52
Re	8.100	7.880	17.000	26.000	5.10	82	45	49
Os	7	8.700	17.000	25.000	4.60	86	48	50
Ir	6.930	9.100	17.000	27.000	5.30	80	44	50
Pt	5.852	9.000	18.560	28.000	5.30	63	45	53
Au	3.780	9.225	20.500	30.000	4.30	53	54	66
Tl	1.870	6.108	20.428	29.830	3.70	13	38	57
Pb	2.040	7.416	15.032	31.937	4.10	20	23	52
Bi	2.150	7.289	16.690	25.560	4.30	18	27	39

Note:

Λ is the sublimation energy.

I_1 , I_2 , and I_3 are first, second, and third ionization potentials.

Φ is work function.

F_1 , F_2 , and F_3 are calculated evaporation fields for 1^+ , 2^+ , and 3^+ charged ions.

The bold is the expected states.

Appendix B

The interplanar spacings d between planes (hkl) with unit cell lengths a , b , c and angles α , β , γ can be calculated from these lattice parameters.

$$\text{Cubic: } \frac{1}{d_{hkl}^2} = \frac{h^2 + k^2 + l^2}{a^2}$$

$$\text{Tetragonal: } \frac{1}{d_{hkl}^2} = \frac{h^2 + k^2}{a^2} + \frac{l^2}{c^2}$$

$$\text{Hexagonal: } \frac{1}{d_{hkl}^2} = \frac{4}{3} \left(\frac{h^2 + hk + k^2}{a^2} \right) + \frac{l^2}{c^2}$$

Rhombohedral:

$$\frac{1}{d_{hkl}^2} = \frac{(h^2 + k^2 + l^2) \sin^2 \theta + 2(hk + kl + hl)(\cos^2 \theta - \cos \theta)}{a^2(1 - 3 \cos^2 \theta + 2 \cos^3 \theta)}$$

$$\text{Orthorhombic: } \frac{1}{d_{hkl}^2} = \frac{h^2}{a^2} + \frac{k^2}{b^2} + \frac{l^2}{c^2}$$

Appendix C

The angles between planes (in degree) of different crystal structure (fcc, bcc, dc, and hcp) of common pure elemental phases.

fcc	(111)	(002)	(022)	(113)	(133)	(024)	(224)
(002)	54.74						
(022)	35.26	45.00					
(113)	29.50	25.24	31.48				
(133)	22.00	46.51	13.26	25.94			
(024)	39.23	26.57	18.43	19.29	22.57		
(224)	19.47	35.26	30.00	10.02	20.51	24.09	
(135)	28.56	32.21	17.02	14.46	14.20	10.67	14.96

bcc	(011)	(002)	(112)	(013)	(222)	(123)	(114)
(002)	45.00						
(112)	30.00	35.26					
(013)	26.57	18.43	25.35				
(222)	35.26	54.74	19.47	43.09			
(123)	19.11	36.70	10.89	21.62	22.21		
(114)	33.56	19.47	15.79	14.31	35.26	19.11	
(024)	18.43	26.57	24.09	8.13	39.23	17.02	18.43

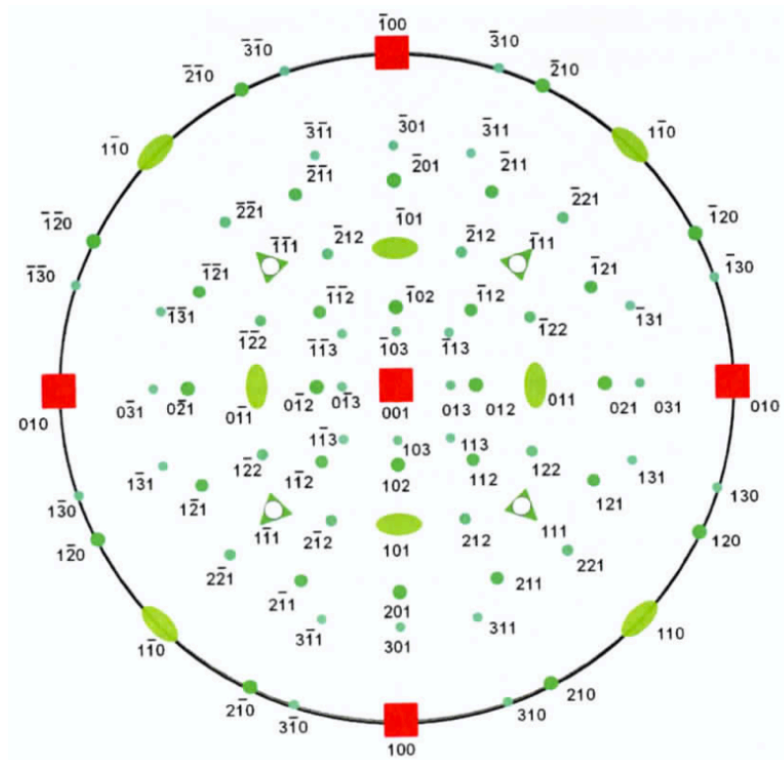
dc	(111)	(220)	(311)	(400)	(331)	(422)	(511)
(220)	35.26						
(311)	29.50	31.48					
(400)	54.74	45.00	25.24				
(331)	22.00	13.26	25.94	46.51			
(422)	19.47	30.00	10.02	35.26	20.51		
(511)	38.94	35.26	9.45	15.79	32.98	19.47	
(531)	28.56	17.02	14.46	32.31	14.20	14.96	19.37

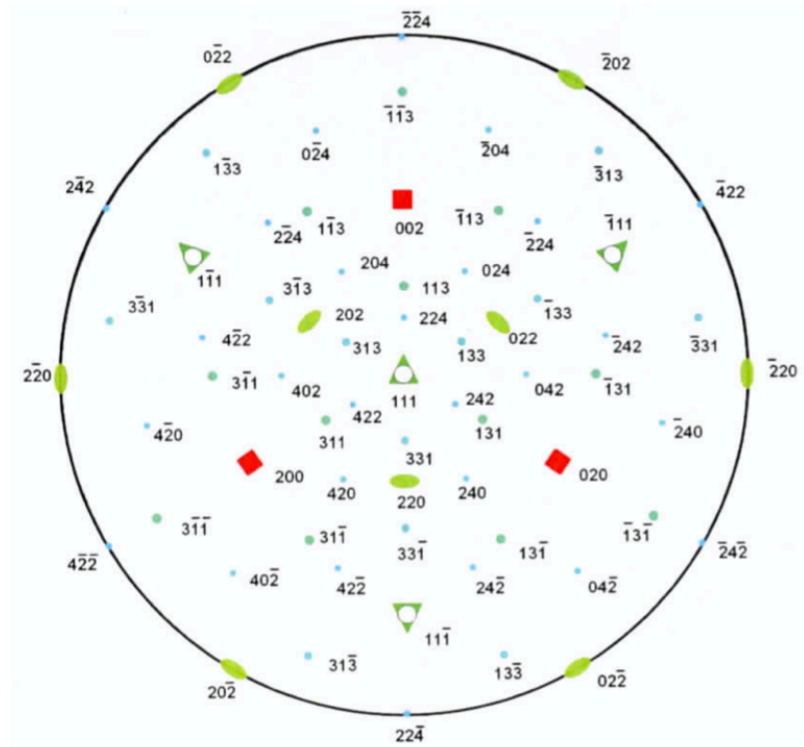
hcp	(100)	(002)	(101)	(102)	(110)	(103)	(112)
(002)	90.00						
(101)	27.94	62.06					
(102)	46.69	43.31	18.75				
(110)	30.00	90.00	40.08	53.55			
(103)	57.85	32.15	29.91	11.16	62.56		
(112)	42.39	58.52	26.21	27.55	31.48	33.37	
(201)	14.85	75.15	13.09	31.84	33.17	43.00	32.03

Note: fcc, bcc, dc, hcp refer to face centred cubic, body centred cubic, diamond cubic crystal respectively.

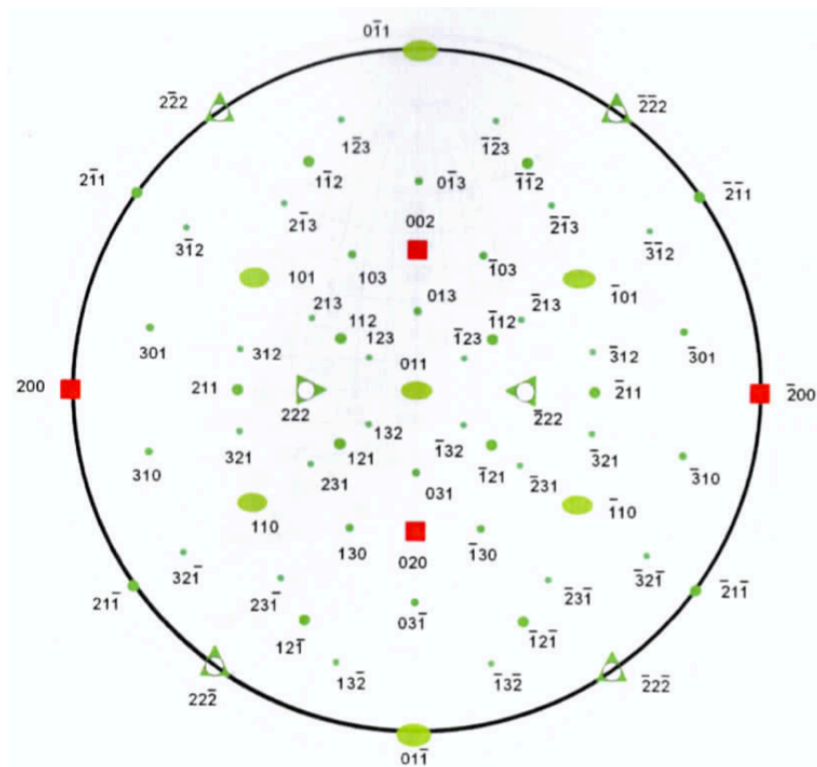
Appendix D

stereographic projections

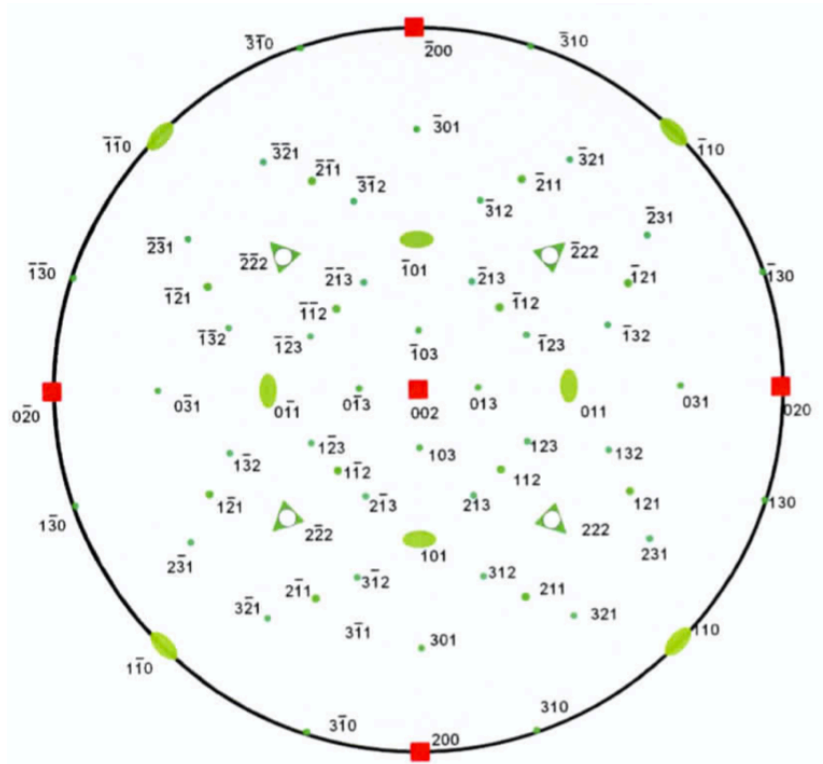




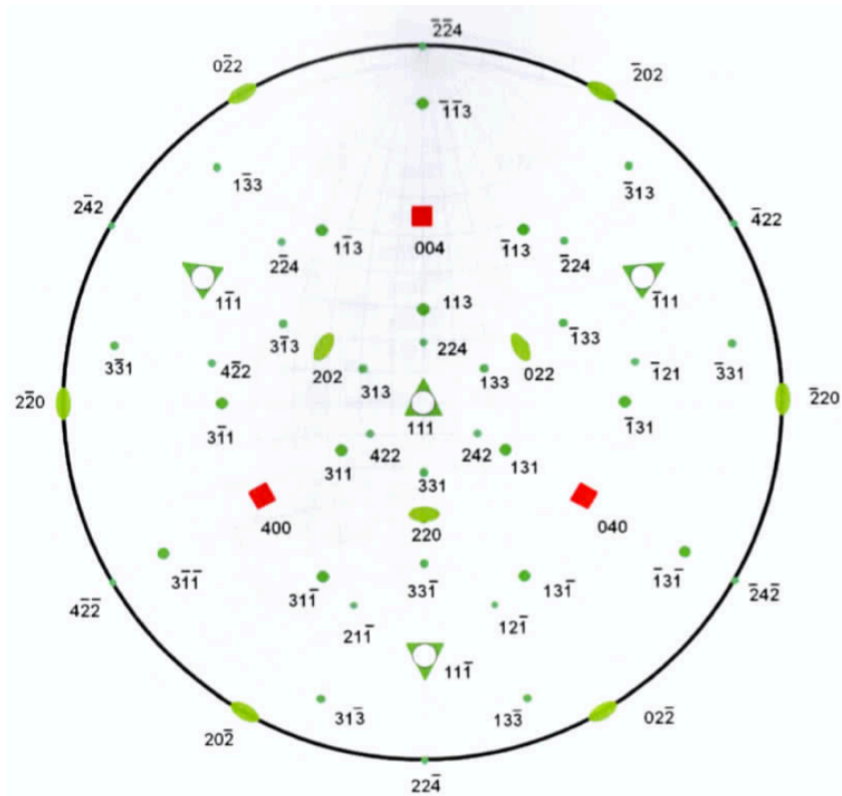
Stereographic projection of the cubic lattice on the (111)-oriented plane indexed for allowable planes in the fcc lattice.



Stereographic projection of the cubic lattice on the (011)-oriented plane indexed for allowable planes in the bcc lattice.



Stereographic projection of the cubic lattice on the (002)-oriented plane indexed for allowable planes in the bcc lattice.



Stereographic projection of the cubic lattice on the (111)-oriented plane indexed for allowable planes in the dc lattice.

Appendix E

Electropolishing Chemicals and Conditions

Material	Electrolyte	Condition
Aluminium (Al)	1–10 % perchloric acid in	5–10 V AC at –10 °C
Al based alloys	1 st : 25 % perchloric acid in glacial acetic acid; 2 nd : 2 % perchloric acid in 2-butoxyethanol	1 st : 10–25 V DC 2 nd : 10–25 V DC
Al–copper(Cu)	80 % HNO ₃ in water	3 V DC at 0 °C
Al–Lithium(Li) Al–zinc (Zn)– magnesium (Mg)	30 % HNO ₃ in methanol	5–7 V DC at –30 °C
Al–Mg–scandium (Sc)	1 st : 30 % HNO ₃ in methanol; 2 nd : 2 % perchloric acid in butoxyethanol	
Baron (B)	KOH or NaOH	10 V–20 V AC
Carbon/graphite (C)	1.25 N NaOH in water	4.5 VDC
Cobalt (Co) based alloy	1 st : 25 % chromic acid in water; 2 nd : 10 % HCl in water	1 st : 6 V AC 2 nd : 3.2 V AC
Cu	1 st : 70 % orthophosphoric acid in water 2 nd : 100 orthophosphoric acid	1 st : 1–5 V AC 2 nd : 8–15 V DC
Cu–iron (Fe)	10 % H ₃ PO ₄ in water	4–10 V DC at 0 °C
Germanium (Ge)	30–50 % HF in HNO ₃	AC
Gold (Au)	20 wt % KCN in water	4–5 V DV
Iridium (Ir)	30 % chromic acid in water	2–10 V AC
Fe based alloys	1 st : 10–25 % perchloric acid (70 %) in glacial acetic acid 2 nd : 2 % perchloric in 2-butoxyethanol	1 st : 10–25 V DC 2 nd : 10–25 V DC
Mg alloys	1 st : 25 % perchloric acid (70 %) in glacial acetic acid 2 nd : 2 % perchloric in 2-butoxyethanol	1 st : 10–25 V DC 2 nd : 10–25 V DC
Molybdenum (Mo)	5 M NaOH in water or 12 % H ₂ SO ₄ in water	6 V AC
Mo–silicon (Si)	12 % H ₂ SO ₄ in CH ₃ OH	7 V DC
MgO/Cu	10 vol% Na ₂ Cr ₂ O ₇ in glacial acetic acid	2–20 V DC

Niobium (Nb)	10 % HF in HNO ₃	1–3 V DC
Nb ₃ Sn	10 % HF in HNO ₃	Chemical
Platinum (Pt)	80 % NaNO ₃ , 20 % NaCl	3–5 V DC molten
Rhenium (Re)	50 % H ₃ PO ₄ in H ₂ O ₂	3–9 VDC
Ruthenium (Ru)	25 % KCl or KOH in water	1.5–30 V AC
Si	30 %–50 % HF in HNO ₃	Chemical
Tantalum (Ta)	45 % HF, 22 % H ₂ SO ₄ , 22 % H ₃ PO ₄ in acetic acid	15 V DC
Titanium (Ti)	6 % perchloric acid, 34 % n-butanol in methanol	50–60 V DC at –50 °C
Ti carbide	5 % H ₂ SO ₄ in methanol	–30 °C
Tungsten (W)	5 % in water	1–5 V AC

Note: electropolishing is conducted at room temperature unless otherwise stated. The proportions of all mixture electrolyte are presented in percentages by volume. These electrodes, percentage, and conditions should be used as a guide. Specific conditions may vary according to laboratories conditions and alloy composition.

1st and 2nd refer to the first step and second step, respectively.

Appendix: F

Matlab Code to Fit Electric Field.

```
% raw data
xdata=[0.5 1.5 2.5 3.5 4.5 5.5 6.5 7.5 8.5 9.5];
ydata=[1.000 0.923 0.776 0.533 0.269 0.185 0.101 0.060
0.053 0.030];
error=[0.000 0.215 0.278 0.265 0.236 0.166 0.096 0.054
0.046 0.025];

ydata_u=ydata+error;
ydata_l=ydata-error;

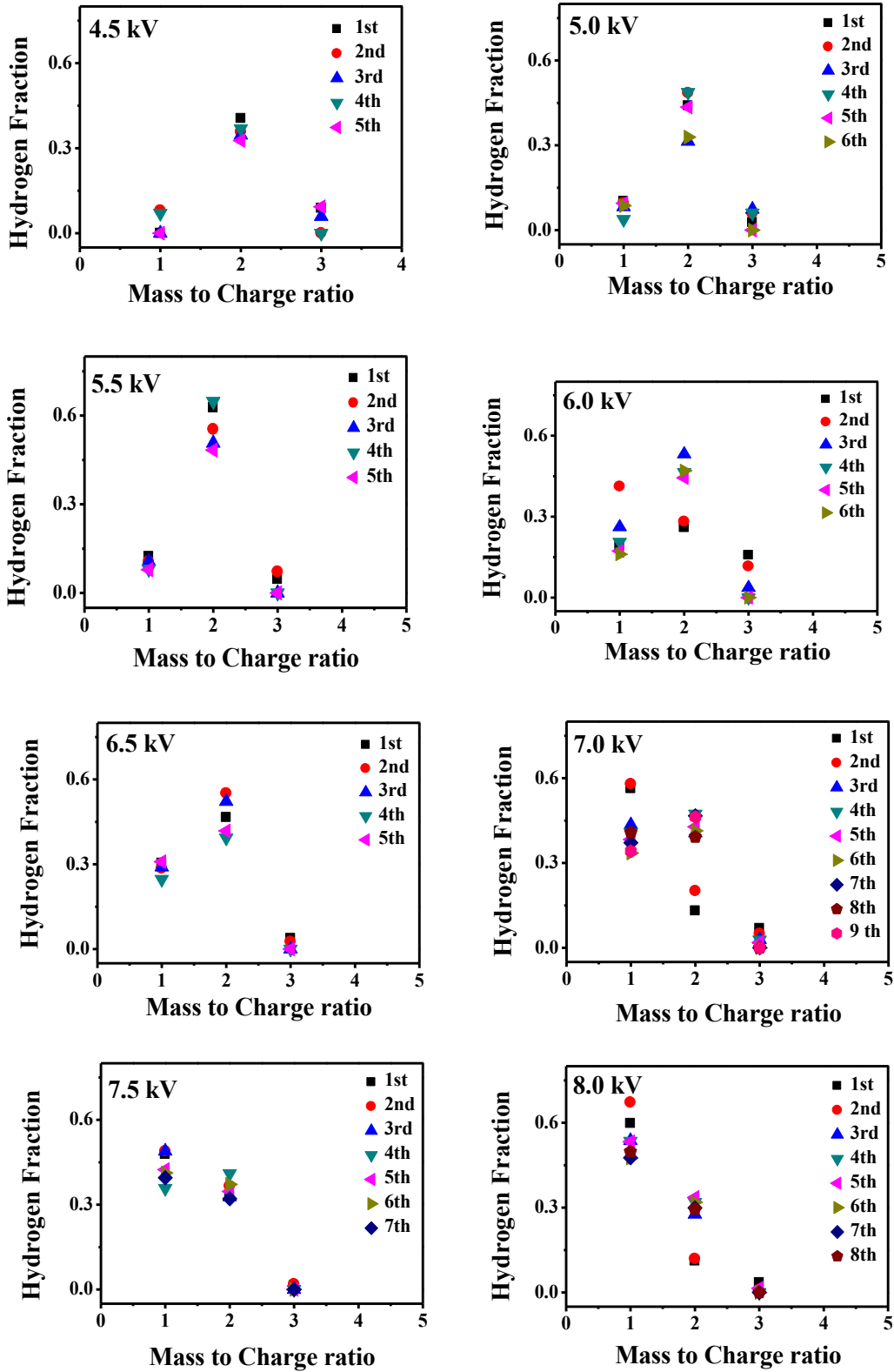
% fitting
lb=[0,0];
ub=[inf,0.01];
fun=@(x,xdata)exp(x(1).*((1-x(2).*xdata.^2)-1))
x0 = [1,1];
x = lsqcurvefit(fun,x0,xdata,ydata,lb,ub)
y=1-x(2).*xdata.^2;

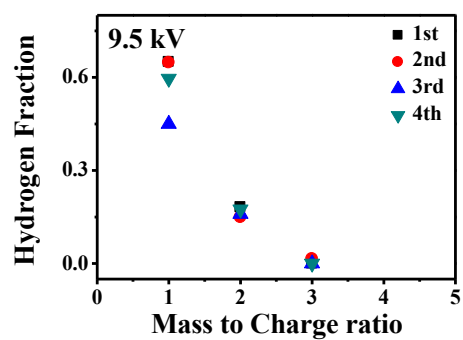
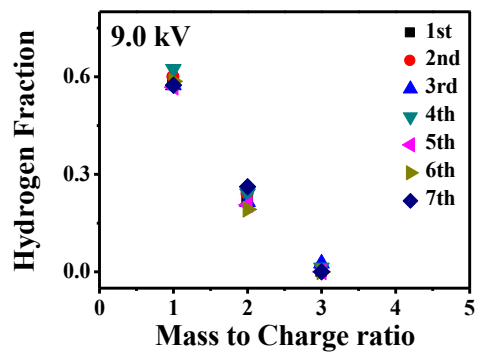
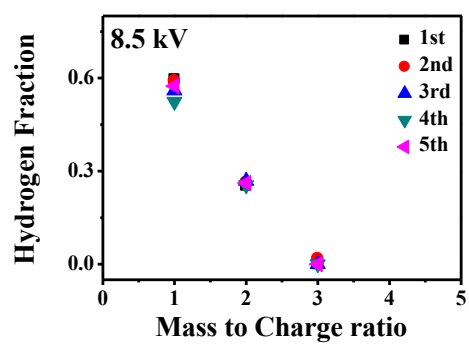
%errorbar calculation
error_uu=((log(ydata_u))./x(1)+1);
error_ll=((log(ydata_l))./x(1)+1);
error_u=error_uu-y;
error_l=y-error_ll;

hold on
%convert the ring number to
xdata_angle=xdata.*6.9+1.166;
% draw curve and errorbar
scatter(xdata_angle,y,'bo','lineWidth',3)
errorbar(xdata_angle,y,error_u,error_l,'k','LineWidth',2)
xlabel('angle (\circ)')
ylabel('EF/EF_{max}')
hold off
```

Appendix: G

Mass Spectrum of H^+ , H_2^+ and H_3^+ obtained from Pt surface at 60 K by laser pulse (2.5 nJ/pulse).





Appendix: H

Fortran Code to Make Pt fcc Crystal

```
program crystalstructure
  implicit none
  integer n, c, i, j, k, p, nc, q, s, g, h, maxcoord
  real :: preb(8000000) = -1.0
  integer :: coord(8000000) = -1
  real newpreb(8000000)
  integer newcoord(8000000)
  real :: b(8000000) = 0.0
  real newb(8000000)
  real nx, ny, nz, d, r, cx, cy, cz, maxpreb, minpreb, dia, wtn,
atomdst
  real tmpx, tmpy, tmpz
  real x(100000000), y(100000000), z(100000000)
  real realx(8000000), realy(8000000), realz(8000000)
  real newx(8000000), newy(8000000), newz(8000000)
  character crystr*3
  character elem*2
  character filename*30
  ! === 結晶構造(立方体)x,y,zの作製 ===
77 write(*,*) 'select Pt or W'
  read(*,*) elem
  if (elem == 'W') then
    d = 3.165
    wtn = 2.5
    crystr = 'bcc'
    atomdst = sqrt(3.0)/2.0
  else if (elem == 'Pt') then
    d = 3.9231
    wtn = 1.5
    crystr = 'fcc'
    atomdst = sqrt(2.0)/2.0
  else
    go to 77
  end if
  write(*,*) 'input diameter of sphere [nm]'
  read(*,*) dia
  write(*,*) 'enter output file name (*.cif)'
  read(*,*) filename
```

```

nc = 10*dia/d
r = nc/2.0
cx = r
cy = r
cz = r
p = 0
q = 0
s = 0
! === bcc単位格子を三次元に平行移動(1格子あたり2原子)===
if (crystr == 'bcc') then
  do i = 1, nc
    do j = 1, nc
      do k = 1, nc
        tmpx = (0.0+1.0*(i-1))
        tmpy = (0.0+1.0*(j-1))
        tmpz = (0.0+1.0*(k-1))
        if ((tmpx-cx)**2 + (tmpy-cy)**2 + (tmpz-cz)**2 <
r**2) then
          s = s+1
          if ((tmpx-cx)**2 + (tmpy-cy)**2 + (tmpz-
cz)**2 > (r-3.0)**2) then
            q = q+1
            x(q) = tmpx
            y(q) = tmpy
            z(q) = tmpz
          end if
        end if
        tmpx = (0.5+1.0*(i-1))
        tmpy = (0.5+1.0*(j-1))
        tmpz = (0.5+1.0*(k-1))
        if ((tmpx-cx)**2 + (tmpy-cy)**2 + (tmpz-cz)**2 <
r**2) then
          s = s+1
          if ((tmpx-cx)**2 + (tmpy-cy)**2 + (tmpz-
cz)**2 > (r-3.0)**2) then
            q = q+1
            x(q) = tmpx
            y(q) = tmpy
            z(q) = tmpz
          end if
        end if
      end do
    end do
  end do
end do

```

```

        end do
    end do
    ! === fcc単位格子を三次元に平行移動(1格子あたり4原子)===
    else if (cryststr == 'fcc') then
        do i = 1, nc
            do j = 1, nc
                do k = 1, nc
                    tmpx = (0.0+1.0*(i-1))
                    tmpy = (0.0+1.0*(j-1))
                    tmpz = (0.0+1.0*(k-1))
                    if ((tmpx-cx)**2 + (tmpy-cy)**2 + (tmpz-cz)**2 <
r**2) then
                        s = s+1
                        if ((tmpx-cx)**2 + (tmpy-cy)**2 + (tmpz-
cz)**2 > (r-3.0)**2) then
                            q = q+1
                            x(q) = tmpx
                            y(q) = tmpy
                            z(q) = tmpz
                        end if
                    end if
                    tmpx = (0.5+1.0*(i-1))
                    tmpy = (0.5+1.0*(j-1))
                    tmpz = (0.0+1.0*(k-1))
                    if ((tmpx-cx)**2 + (tmpy-cy)**2 + (tmpz-cz)**2 <
r**2) then
                        s = s+1
                        if ((tmpx-cx)**2 + (tmpy-cy)**2 + (tmpz-
cz)**2 > (r-3.0)**2) then
                            q = q+1
                            x(q) = tmpx
                            y(q) = tmpy
                            z(q) = tmpz
                        end if
                    end if
                    tmpx = (0.5+1.0*(i-1))
                    tmpy = (0.0+1.0*(j-1))
                    tmpz = (0.5+1.0*(k-1))
                    if ((tmpx-cx)**2 + (tmpy-cy)**2 + (tmpz-cz)**2 <
r**2) then
                        s = s+1
                        if ((tmpx-cx)**2 + (tmpy-cy)**2 + (tmpz-

```

```

cz)**2 > (r-3.0)**2) then
    q = q+1
    x(q) = tmpx
    y(q) = tmpy
    z(q) = tmpz
end if
end if
tmpx = (0.0+1.0*(i-1))
tmpy = (0.5+1.0*(j-1))
tmpz = (0.5+1.0*(k-1))
if ((tmpx-cx)**2 + (tmpy-cy)**2 + (tmpz-cz)**2 <
r**2) then
    s = s+1
    if ((tmpx-cx)**2 + (tmpy-cy)**2 + (tmpz-
cz)**2 > (r-3.0)**2) then
        q = q+1
        x(q) = tmpx
        y(q) = tmpy
        z(q) = tmpz
    end if
end if
end do
end do
end do
end if

print *, 'completed'

print *, 'Number of all spherical (stuffed) atoms=', s
! === 球を構成する原子の拡張配位数b(i)を計算(中心原子からwtnまで) ===
! === 2×dより内側の原子は最大配位数とする(内側が空洞なので) ===
! === 自身をカウントするためb(i)の初期値は-1 ===
print *, 'calculating coordination numbers...'

do i = 1, q
    do k = 1, q
        if (x(k) <= x(i)+(wtn+0.01) .and. x(k) >= x(i)-(wtn+0.01))
then
            if (y(k) <= y(i)+(wtn+0.01) .and. y(k) >= y(i)-
(wtn+0.01)) then
                if (z(k) <= z(i)+(wtn+0.01) .and. z(k) >= z(i)-
(wtn+0.01)) then

```



```

        if ((x(i)-x(k))**2+(y(i)-y(k))**2+(z(i)-z(k))**2
<= wtn**2+0.01) then
            preb(i) = preb(i)+1.0
            if ((x(i)-x(k))**2+(y(i)-y(k))**2+(z(i)-
z(k))**2 <= atomdst**2+0.01) then
                coord(i) = coord(i)+1
            end if
        end if
    end if
end if
end if
end if
end do
    if (mod(i, 1000) == 0) then
        print *, 'calculated', i, 'atoms in ', q
    end if
end do

print *, 'completed'

maxpreb = maxval(preb)
maxcoord = maxval(coord)

do i = 1, q
    if (preb(i) <= preb(i+1)) then
        minpreb = preb(i)
    end if
end do

do i = 1, q
    if ((x(i)-cx)**2 + (y(i)-cy)**2 + (z(i)-cz)**2 < (r-2.0)**2)
then
        preb(i) = maxpreb
        coord(i) = maxcoord
    end if
end do

do i =1, q
    b(i) = exp(minpreb-preb(i))
    if (b(i) > 1.0) then
        b(i) = 1.0
    end if
end do

```

```

h = 0
do i = 1, q
    if (coord(i) /= maxcoord) then
        h = h+1
    end if
end do

! === 表示を軽くするため内側の原子をさらにくり抜き ===
g = 0
do i = 1, q
    if ((x(i)-cx)**2 + (y(i)-cy)**2 + (z(i)-cz)**2 > (r-
2.0*atomdst)**2) then
        g = g+1
        newx(g) = x(i)
        newy(g) = y(i)
        newz(g) = z(i)
        newpreb(g) = preb(i)
        newb(g) = b(i)
        newcoord(g) = coord(i)
    end if
end do

! === 座標を実座標(A単位)に置き換え ===
do i = 1, g
    realx(i) = newx(i)*d
    realy(i) = newy(i)*d
    realz(i) = newz(i)*d
end do

open (18, file=trim(filename)//'.cif', status='replace')

! === CIFファイル書き出し(ヘッダー) ===
write (18,*) '# generated by fortran'
write (18,*) '# '//cryst, 'r =', r*d, ' angstroms'
write (18,*) '#number of stuffed atoms =', s, ' atoms'
write (18,*) '#number of surface atoms =', h, ' atoms'
write (18,*) 'data_ '//trim(filename)
write (18,*) '_entry.id '//trim(filename)
write (18,*) '#'
write (18,*) 'loop_'
write (18,*) '_atom_site.group_PDB'
write (18,*) '_atom_site.id'

```

```

write (18,*) '_atom_site.type_symbol'
write (18,*) '_atom_site.label_atom_id'
write (18,*) '_atom_site.label_alt_id'
write (18,*) '_atom_site.label_comp_id'
write (18,*) '_atom_site.label_asym_id'
write (18,*) '_atom_site.label_entity_id'
write (18,*) '_atom_site.label_seq_id'
write (18,*) '_atom_site.pdbx_PDB_ins_code'
write (18,*) '_atom_site.Cartn_x'
write (18,*) '_atom_site.Cartn_y'
write (18,*) '_atom_site.Cartn_z'
write (18,*) '_atom_site.occupancy'
write (18,*) '_atom_site.B_iso_or_equiv'
write (18,*) '_atom_site.pdbx_formal_charge'
write (18,*) '_atom_site.auth_asym_id'
write (18,*) '_atom_site.pdbx_PDB_model_num'
! === 各原子情報書き出し ===
do i = 1, g
    write (18, 99) 'HETATM ', i, ' CU CU . CU B 2 700 ? ',
realx(i), realy(i), realz(i), newcoord(i), newb(i), newpreb(i), ' A
1'
99    format(a, i8, a, f10.3, f10.3, f10.3, i3, f8.2, f8.2, a)
end do
close (18)

end program crystalstructure

```

PUBLICATIONS

1. “Quantitative Analysis of Residual Hydrogen on Platinum Surface by Atom Probe”

Sunwei Chen, R. Murakami, K. Araki, M. Owari
e-Journal of Surface Science and Nanotechnology. **18**, 127–132 (2020).

2. “A method to study the electric field distribution on sample surfaces in atom probe analysis.

Sunwei Chen, T. Suzuki, B. Tomiyasu, M. Owari
Surface and Interface Analysis. **52**, 463–469.

3. “The interaction of O₂ and residual H on Pt surface studied by field ion microscopy and in-situ surface atom probe.”

Sunwei Chen, T. Suzuki, B. Tomiyasu, M. Owari
Journal of Surface Analysis. **26**, 1–8 (2019).

Conferences

1. “Quantitative Analysis of Residual Hydrogen on Platinum Surface by Atom Probe”

Sunwei Chen, R. Murakami, K. Araki, M. Owari
Symposium on Practical Surface Analysis 19 (International), Sapporo Japan, November 3–8, Poster Presentation.

2. “Distribution on Sample Surfaces in Atom Probe Analysis. Surface and Interface Analysis”

Sunwei Chen, T. Suzuki, B. Tomiyasu, M. Owari
12th International Symposium on Atomic Level Characterizations for New Materials and Devices 19, Kyoto Japan, October 20–25, Poster presentation.

3. “The interaction of O₂ and residual H on Pt surface studied by field ion microscopy and in-situ surface atom probe.”

Sunwei Chen, T. Suzuki, B. Tomiyasu, M. Owari
Symposium on Practical Surface Analysis 18, Numazu Japan, October 15–16, Poster Presentation.

ACKNOWLEDGEMENT

First and foremost I would like to express sincere and deepest sense of gratitude to my supervisor Prof. Masanori Owari (The University of Tokyo) for continuous guidance, enthusiastic discussion, caring, patience and hearty encouragement over the last three years. I still cannot forget Prof. Owari accept me as a member of Owari Lab, and supported and encouraged me to pass the entrance examination of doctoral course.

I am extremely grateful to Dr. Bunbunoshin Tomiyasu (The University of Tokyo), an assistance professor in Owari Lab, for his edifying instruction, enthusiastic discussion, ample patience and immense supports on my research. Despite he left our Lab since Sep. 2019, every time I encountered difficulties in result analysis and machine repairment, he supported me without reservation.

I am thankful to Dr. Yun Kim and Takuya Egawa, in despite of their busy graduation schedule, they still taught me a lot of basic knowledge and experimental skill about AP. They made me quickly get used to the new research environment.

I am also thankful to Takumi Suzuki, a graduated master student in our lab. I was impressed by his talent, concentration, enthusiasm and diligence in scientific research. I also want to express my sincere appreciation to Dr. Morita (Kogakuin University) for his valuable advice on AP software production and Dr. Mayama (Toshiba nanoanalysis) for valuable discussion, to the engineer of Roentdek Handels GmbH, Achim Czasch, for his assistance and patience to help us to repair DLD, to Prof. Iwata for his efforts to fix our voltage pulse system, for Ryo Murakami, Kohei Matsumura, Takeki Azuma, Masuo Tagaki, for his kind assistance on this research and teaching me Japanese.

I am grateful to Dr. Sohee Kang, another senior foreign student in our lab for her assistance on academic and private affairs during these three years, to Koya Araki for his assistance on job hunting.

Finally, I would like express my profound appreciation to my parents, Mr. Xiaolong Chen and Ms. Sujun Sun for their warm encouragement and financial support, to my hudsbund, Dr. Yiyang Zhan, who always encourages me to overcome the difficulties and gave valuable advice on paper writting.

Sunwei Chen

June 2020